ISSN 0915-6348

NATIONAL INSTITUTE FOR FUSION SCIENCE

Structure Formation and Function of Gaseous, Biological and Strongly Coupled Plasmas

(Ed.) M. Tanaka

(Received - Sep. 16, 1999)

NIFS-PROC-43 Sep. 1999

RESEARCH REPORT
NIFS-PROC Series

NAGOYA, JAPAN

Structure Formation and Function of Gaseous, Biological and Strongly Coupled Plasmas

Motohiko Tanaka, Editor

National Institute for Fusion Science, Toki 509-5292, Japan

The word "plasma" can refer either to a biological fluid in living cells or to a high-temperature ionized gas in space and fusion studies (*Webster New World College Dictionary, 3rd. edition*). The objective of the series of lectures in this proceedings is to find the cross-disciplinary relationships of these two kinds of plasmas, which are usually never discussed in a single workshop. However, it has been found that strongly coupled laboratory plasmas, charged polymers, DNA/RNA threads in living organisms, and hydrogen-bond networks in water are all closely related under Coulombic interactions. Furthermore, from a technical point of view, particle (i.e., kinetic) and fluid descriptions are common to solar-terrestrial, fusion, and biological investigations of plasmas. Both technical aspects and applications in these wide areas of plasmas are presented in this proceedings.

Keywords: hot (gas) plasma, strongly coupled plasma, biological plasma, molecular machinery, charged polymers, DNA folding, hydrogen-bond network in water, rotating magnetoplasma, magnetic reconnection, solar-terrestrial physics.

Contents

Toward the Creation of an Artificial Cellular System

Kenichi Yoshikawa and Shin-ichirou Nomura
Department of Physics, Graduate School of Science,
Kyoto University, Kyoto 606-8502

With the development of molecular biology and biochemistry, knowledge of the details of biological molecules has been increasing rapidly. On the other hand, the phenomenon of life itself remains a mysterious matter. Individual biological cells of several and several tens of micrometers maintain life by themselves in a self-organized manner. It is obvious that the essence of life cannot be understood as the simple accumulation of the knowledge of individual biological molecules.

We are currently studying life phenomena, based on the view that living organisms exist with self-organized supramoleculer assemblies under nonequilibrium thermodynamically open conditions. Over a number of years, we have focused our efforts on the development of the physical chemistry of the folding transition of giant macromolecules, with special emphasis on giant DNA molecules.

The results of our research are summarized as follows.[1-5]

(1) Individual single duplex-DNA molecules with a size over 10 kbp exhibit large discrete transition, or first-order phase transition, between the elongated coiled state and the collapsed globule state, whereas the physicochemical characteristics in an ensemble average of DNA chains exhibit a continuous nature in the transition. In other words, there exists no phase-transition at the ensemble level of molecular chains.

(2) There is a rich variety of morphology in the collapsed DNAs, e.g. toroid, spherical, spool-like structures. By controlling the thermodynamic parameters as well as the kinetic parameters, various kinds of folded structures can be created with high reproducibility.

(3) With the choice of suitable condensation agents, the all-or-none character in the folding transition of DNA is changed and, as a result, intrachain phase-segregated structures are generated.

(4) The above experimental results have been discussed with the help of theoretical considerations. We have purposed a phase-diagram for single macromolecules as the function with interaction parameter and chain stiffness (see Fig. 1).

As we have already published these results elsewhere,[1-5] in the present article we would like to describe our attempts to develop an artificial cellular system as an extension of the

results in our current research under the project, as an indication for the future direction of the study.

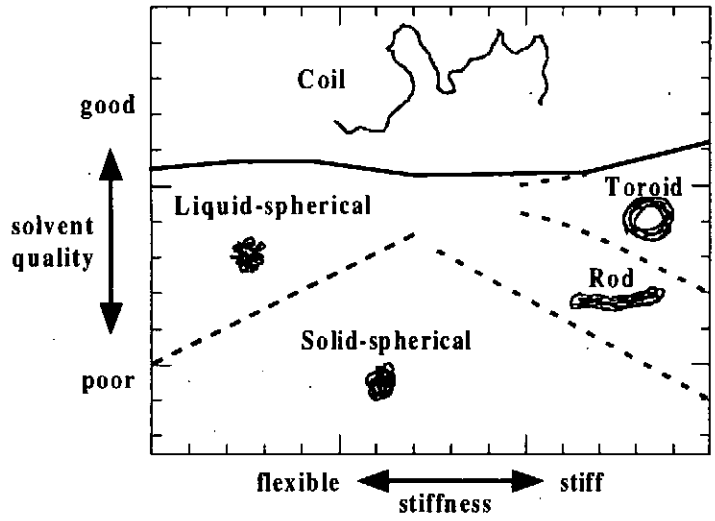

Figure 1. Schematic representation of the phase diagram with the parameters of chain stiffness and solvent quality, showing the morphological change depending on temperature and stiffness.[5]

Preparation of a Cell-sized Liposome

To establish the methodology for obtaining a cell-sized liposome is an important step toward the creation of an artificial cellular system. Although many efforts have been made to develop techniques to prepare a giant liposome from neutral phospholipids, only multi-lamellar liposomes have been obtained under mild conditions such as natural

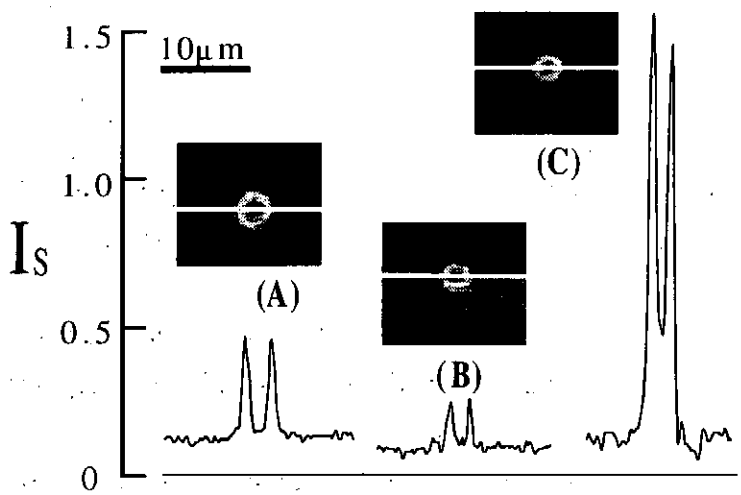

Figure 2. Dark-field microscopic images and the intensity I_s of the scattered light for giant liposomes of DOPC prepared by three different procedures: (A) unilamellar vesicle prepared by ether vaporization method, (B) unilamellar vesicle prepared by natural swelling method with 10mM HEPES buffer (pH=7.0) containing 10mM $MgCl_2$. (C) multilamellar vesicle with natural swelling method with 10mM HEPES buffer (pH=7.0). The intensity I_s is taken along the horizontal line shown in the picture of the liposomes and is nomalized with reference to the scattering from a latex bead with a diameter of 9.975μm, Duke Sci. Corp.

swelling.[6,7] Recently, we have found that giant unilamellar liposome can be prepared from a neutral phospholipid with the procedure of natural swelling in an aqueous solution containing magnesium ion.[8]

Figure 2 exemplifies the dark-field microscopic images on giant liposomes of 1,2-dioleoyl-sn-glycero-3-phosphocholine, DOPC, prepared by the following procedures: (**A**) ether vaporization method, (**B**) natural swelling in the presence of Mg^{2+}, and (**C**) natural swelling in the absence of Mg^{2+}. It is well established that the unilamellar vesicle is produced by the ether vaporization method.[9] It is also known that the multilamellar vesicle is obtained with usual natural swelling.[6,7] Thus, it is clear that the spherical vesicle, obtained by natural swelling in the presence of Mg^{2+} (method B), is classified as a unilamellar liposome. The remaining question is the fact that the scattering intensity $\mathbf{I}_s$ in B is much weaker than that in A. As discussed in our previous report,[7] the liposome obtained by method B is expected to be induced by the osmotic effect owe to the binding of Mg^{2+} to the phosphate group in the natural phospholipid. This suggests that the liposome by method B has high osmotic pressure inside, whereas in the liposome obtained by method A the osmotic pressure inside the vesicle would be almost the same as that of the buffer solution. Thus, there would be large fluctuation within the length of the optical wave length for the liposome by method A. On the other hand, the bilayer membrane would be stretched significantly for the liposome by method B. Such a difference in the fluctuation of the bilayer membrane of the liposomes obtained by methods A and B may result in the large difference in the scattering light intensity between the unilamellar vesicles.

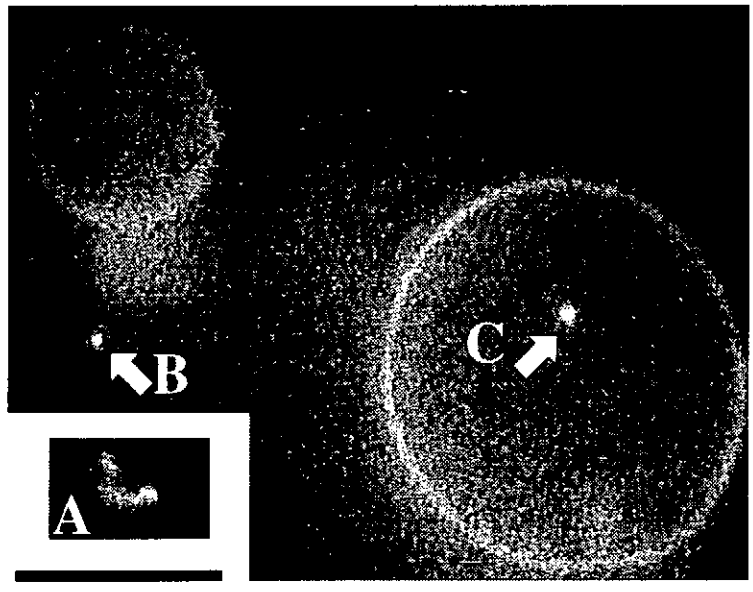

Figure 3. Fluorescence microscopic images of T4 dcDNA molecules: A) in 10mM $MgCl_2$/10 mM HEPES buffer solution (pH=7.1); and B, C) in the buffer solution with closed phospholipid liposomes outside and inside the liposomes, respectively. The bar represents 10μm.

Developing the Model of an Artificial Cellular System

By combining the results of our recent studies on DNA and on giant liposomes, we have tried to establish the methodology for preparing giant vesicles entrapping giant DNA. Fig. 3 shows the actual examples of the DOPC vesicles entrapping T4 DNA molecules.[10] Here again, the presence of Mg^{2+} is essential for preparing the giant liposomes.

We have adapted the procedure of natural swelling of DOPC film in the magnesium solution containing T4 DNAs. It has been found that an artificial cellular system constructed in this way has an efficiency of about 1/30 of the whole number of the liposomes. It is noted that the giant DNAs undergo intrachain and translational Brownian motion inside the vesicles.

References

1. Yoshikawa, K.; Takahashi, M.; Vasilevskaya, V. V.; Khokhlov, A. R., *Phys. Rev. Lett.*, **1996**, *76*, 3029.
2. Starodoubtsev, S. G.; Yoshikawa, K., *J. Phys. Chem.*, **1996**, *100*, 19702.
3. Yoshikawa, K.; Yoshikawa, Y.; Koyama, Y.; Kanbe, T., *J. Am. Chem. Soc.*, **1997**, *119*, 6473.
4. Noguchi, H.; Yoshikawa, K., *Chem. Phys. Lett.*, **1997**, *278*, 184.
5. Noguchi, H.; Yoshikawa, K., *J. Chem. Phys.*, **1998**, *109*, 5070.
6. Mueller, P.; Chien, T. F.; Rudy, B., *Biophys. J.*,**1983**, *44*, 375.
7. Hub, H. H.; Zimmermann, U.; Ringsdorf, H., *FEBS Lett.*, **1982**, *140*, 254.
8. N. Magome; T. Takemura; K. Yoshikawa, *Chem. Lett.*, **1997**, 205.
9. Deamer, D.; Bangham, A. D., *Biochim. Biophys. Acta*, **1976**, *443*, 629.
10. Kumazawa, N.; Mel'nikova, Yu. S.; Yoshikawa, K., *Macromol. Symp.*, **1996**, *106*, 219.

Spatiotemporal heterogeneity and Rugged Energy Landscape in Liquid Water

M. Sasai
Graduate School of Human Informatics, Nagoya University, Nagoya, 464-8601, Japan

Abstract

Study of water should provide a key to reveal physics of liquids and glasses through its prominent static and dynamic anomalies:Specific heat and compressibility become anomalously large and can be fitted by an algebraically divergent formula, $C_p \approx \kappa_T \approx |T - T_s|^{-1/2}$ with $T_s \approx -46^{\circ}C$ at least for the temperature region $T > -30^{\circ}C$ at 1 atm [1] and viscocity and the diffusion constant show $\eta \approx 1/D \approx |T - T_c|^{-\gamma}$ with $\gamma \approx 1.8$ and $T_s \approx T_c$ [2]. It is still an open question, however, whether there is a common physical basis underlying both static and dynamic anomalies in supercooled water. The molecular dynamics (MD) analyses suggest a scenario to understand these anomalies.

Local Structure Index

There have been accumulating evidences in experimental and simulation data that the transition between high density amorphous (HDA)-ice and low density amorphous (LDA)-ice is responsible for the thermodynamic anomalies of supercooled water [3]. HDA-ice and LDA-ice experimentally observed in the low temperature regime should undergo glass transitions to turn into high density liquid (HDL) and low density liquid (LDL) and the HDA-LDA transition line can be extrapolated to the HDL-LDL transition line. The anomalous fluctuation of supercooled water might be associated with the fluctuation around the HDL-LDL transition. To see whether this hypothesis is indeed valid, a suitable order parameter has to be defined and fluctuation should be examined in terms of the order parameter. In Ref.4 it was shown with the MD simulation that density of molecules in the region bound by two spheres $3.2\text{Å} < r < 3.8\text{Å}$ around each centered molecule can be used as a sign of local strucutral ordering and was quantified by a parameter termed local structure index (LSI). Molecules with large LSI were called structured molecules and ones with small LSI were called destructured molecules. Each molecule alternatively goes through structured and destructured periods and lifetime of the period is hierarchically distributed from several hundred fs to 10ps at 0°C at 1 atm. Structured molecules tend to gather together to form microdomains. By calculating the neutron-weighted radial distribution function around each molecule it was shown that the structured domains are LDA-like and the destructured domains are HDA-like[4]. In Fig.1 the LDA-like regions and the HDA-like regions are separately shown for the same configuration of the MD snapshot.

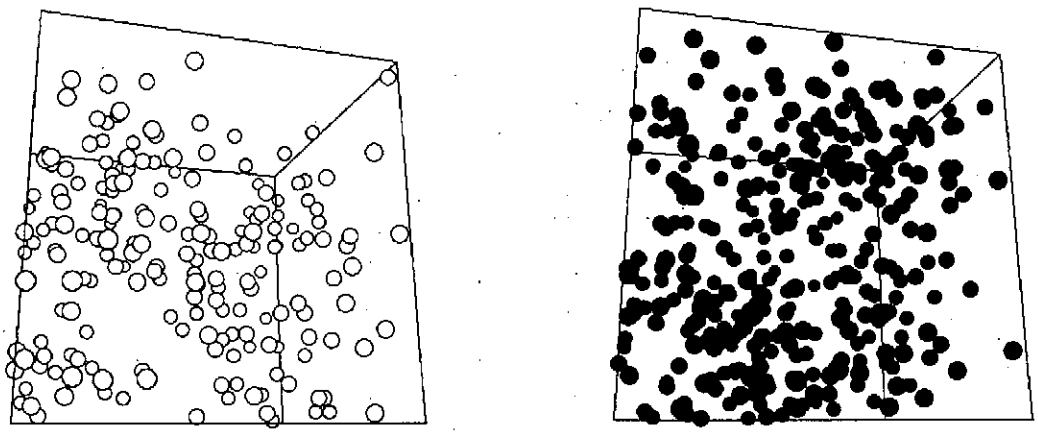

Fig. 1. A snapshot of 512 water molecules simulated with the SPC/E potential at temperature 273K with density ρ= 0.997g/cm^3. Positions of LDA-like molecules (white spheres) and positions of HDA-like molecules (dark spheres) are separately shown in the left and in the right figures, respectively. Liquid water can be regarded as a composite of the LDA-like regions and the HDA-like regions.

Unstable Modes are Localized in the HDA-like Regions

Normal modes are derived by diagonalizing the Hessian of the energy of the instantaneous configuration of the MD trajectory. It should be noticed that at every configuration examined in the MD simulation at $T > T_c$ there always exist the unstable modes with certain fraction, 3.47% of total modes in average at 273K. Energy surface has the negative curvature in the direction of the eigenvector of these modes. Thus, the system is always around the saddle points. There is extremely small chance for the system to visit near the energy minimum. Thus, it is an incorrect notion to describe water dynamics above T_c that the trajectory staying near the minimum suddenly surpasses the energy barrier to jump to the next minimum, but it is more suitable to express water dynamics as successive transitions from saddle to saddle. Unstable modes represent the diffusional motion of molecules associated with the structural rearrangement [5].

In Ref. [6] it was shown that the fraction of unstable modes decreases as lowering temperature and was extrapolated to 0% around T_c. This behavior is consistent with the description based on the mode coupling theory [6, 7]. As approaching T_c, saddle-to-saddle motion becomes more difficult and the dynamics should alter its feature from saddle-to-saddle to minimum-to-minimum motion with the activation-type temperature dependence.

We denote the component of the eigenvector of the unstable mode with the imaginary frequency $i\omega$ at the kth molecule as $e(k,a;i\omega)$, where $a = 1$ - 3 is the translational component and $a = 4$ - 6 is the rotational component of the kth molecule. In Fig.2 the translational components of an unstable eigenmode are exemplified. We can see that the eigenvector of the unstable mode is localized in the HDA-like regions in this example.

Fig.2. Translational components $\left(e(k,1;i\omega), e(k,2;i\omega), e(k,3;i\omega) \right)$ of the eigenvector of an unstable mode with frequency $|i\omega| = 74.116244\,\mathrm{cm}^{-1}$ are shown by lines. Length of lines is proportional to the amplitude of $e(k,a;i\omega)$ and the center of the kth line is located at the center of the kth molecule. Positions of LDA-like molecules are shown with spheres. The same configuration as in Fig.1 is used.

The correlation between the HDA-like regions and unstable modes is calculated by the following quantity;

$$B(n)_{\text{unstable}} = \frac{1}{N_{\text{mode}}} \sum_{\mu=1}^{N_{\text{mode}}} \frac{1}{N_n} \sum_{\left\{ \begin{array}{l} k \in \text{molecules which have} \\ n \text{ strutured neighbors} \end{array} \right\}} \sum_{a=1}^{6} \left(e(k,a;i\omega_\mu) \right)^2 \quad , (1)$$

where n is the number of structured molecules around the centered molecule and sum over k is the sum over the centered molecules which have n structured neighbors. N_n is the number of molecules which have n structured neighbors. Sum over μ is the sum over unstable modes and N_{mode} is the number of unstable modes. In Fig. 3 $B(n)_{\text{unstable}}$ is plotted for various temperatures. There is a clear correlation between n and $B(n)_{\text{unstable}}$: $B(1)_{\text{unstable}} / B(5)_{\text{unstable}}$ = 1.8 at 263K with ρ=0.997g/cm^3 and = 2.65 at 207K with ρ=0.97g/cm^3. The same quantity was calculated for the stable modes (modes with real frequency) and no significant n dependence was found for $B(n)_{\text{stable}}$; $B(1)_{\text{stable}} / B(5)_{\text{stable}}$=0.97 at 243K. Thus, unstable modes have larger amplitude at the molecules which have less structured neighboring molecules. In other words, the unstable modes have larger amplitude in the HDA-like regions.

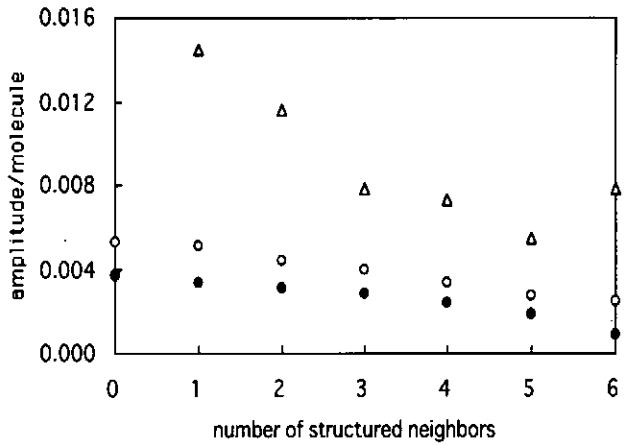

Fig.3. Averaged amplitude of unstable modes $B(n)_{\text{unstable}}$ is plotted against the number of structured neighbor molecules n. 207K (triangle) with ρ=0.97g/cm^3 and 263K (open circle) and 333K (filled circle) with ρ=0.997g/cm^3. Note that the temperature in SPC/E water is shifted from temperature in real water, so that T_c in SPC/E water should be around 190K [8].

From "Saddle-to-Saddle Motion" to "Minimum-to-Minimum Motion"

When dynamics is dominated by the saddle-to-saddle transition through the motion along the direction of unstable modes, diffusional motion of each molecule should be governed by the amplitude of $e(k,a;i\omega)$ of unstable modes. Then, the motion of each molecule is determined by the degree how unstable modes are localized in space. Thus, the motion of molecules is rather entropy-driven than energy-driven. C.A. Angell explained the slow dynamics of supercooled water in terms of the entropy change needed to evoke the collective motion localized in space [9]. The finding in the present paper provides a systematic way to understand the implication of the phenomenological model of Refs.[9] and [10].

As temperature is lowered, motion of the system changes its feature from the "saddle-to-saddle" to "minimum-to-minimum" type. It is plausible to assume that this alternation of characteristics of motion corresponds to the transition of the liquid type from "fragile" to "strong" one. The presen analyses showed that

the transitoion between strong and fragile liquids should be intimately connected to the transition between LDL and HDL. A schematic scenario of this transition is shown in Fig.5. With this mechanism of transition of kinetic features, either the thermodynamically discontinuous transition or the continuous transiton is possible between LDL and HDL. When the density of states decreases abruptly at the temperature around the kinetic transition takes place, then the thermodynamic change can be discontinuous. When the density of states does not change much upon the kinetic transition, then the transition between HDL and LDL should be thermodynamically continuous. Thus, the energy landscape picture should provide a framework to understand the mechanism of anomalies of water.

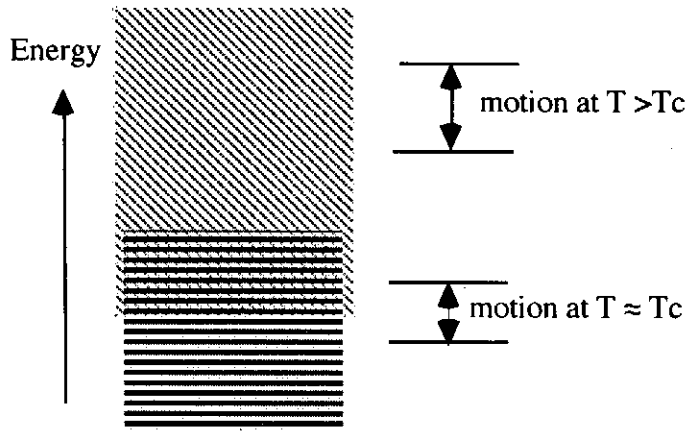

Fig. 5. A schematic diagram of energy spectrum of the configurations of energy extrema. ▨ represents the saddle point configurations and ▬ represents the energy minimum configurations. At T > Tc the system moves from saddle to saddle without approaching the minimum and at around Tc the system begins to be trapped in the energy minimum and liquid changes its nature from "fragile" to "strong".

Acknowledgement

This work is supported by Japan Science and Technology Corporation (Project ACT-JST-98-A5-1), and by Grants-in-Aid from the Ministry of Education, Science, Sports and Culture, Japan (no.11166227 and no.09440147).

Reference

[1] R.J. Speedy, *J. Phys. Chem.* **91**, 3354 (1987).
[2] F.X. Prielmeier et al., *Phys. Rev. Lett.*, **59**, 1128 (1987).
[3] O. Mishima and H.E. Stanley, *Nature*, **396**, 329 (1998).
[4] E. Shiratani and M. Sasai, *J. Chem. Phys.*, **108**, 3264 (1998).
[5] W.-X. Li, T. Keyes, and F. Sciortino, *J. Chem. Phys.*, **108**, 252 (1998).
[6] F. Sciortino and P. Tartaglia, *Phys. Rev. Lett.*, **78**, 2385 (1997).
[7] F. Sciortino et al., *Phys. Rev. Lett.*, **76**, 2730 (1996).
[8] S. Harrington, et al., *J. Chem. Phys.*, **107**, 7443 (1997).
[9] C.A. Angell, *Physica D*, **107**, 122 (1997).
[10] G. Adams and J.H. Gibbs, *J. Chem. Phys.*, **43**, 139 (1965).

Molecular Dynamics Study of Single/Multichain Coulomb Polymers and the Effects of Salt Ions

Motohiko Tanaka[1], A.Yu Grosberg[2,3], and Toyoichi Tanaka[2]

[1] National Institute for Fusion Science, Toki 509-5292, Japan
[2] Massachusetts Institute of Technology, Cambridge, MA 02139, USA
[3] Institute of Biochemical Physics, Russian Academy of Sciences, Moscow 117977, Russia

Abstract

The dynamic behaviors and equilibrium properties of charged polymers of random sequences (polyampholytes) are studied for both the single-chain and multichain cases with the use of molecular dynamics simulations. Single-chain polyampholyte has three temperature regimes under neutral condition, which are characterized by an elongated Gaussian coil and a very dense globule for high and low temperatures, respectively, and by a transition between them at medium temperature. The size of a single-chain polyampholyte shows hysteresis against slow cyclic temperature changes under the Coulomb force and short-range attraction force. The multichain polyampholyte takes a segregated globular phase at low temperature, and the wall-bound one-phase state with separated chains at high temperature. The polyampholyte chains overlap significantly below the critical temperature, at which glass transition takes place. Added salt ions screen the electric field between the monomers and make the polyampholyte soluble when their density is comparable to that of the polyampholyte.

I. Introduction

The polymers that are composed of electrically charged monomers have a wide range of industrial applications. They are also important building blocks of live organisms such as DNA and RNA. Because of the microscopic scales of Angstrom ranges, these polymers constitute *a strongly coupled system*, where the Coulomb energy prevails over the thermal energy, $e^2/\epsilon b k_B T \geq 1$, where e is electron charge, ϵ electrical permitivity, b the average monomer distance, k_B the Boltzmann constant, and T temperature. The charged polymers are classified into two typical groups (or regimes) called *polyelectrolyte* and *polyampholyte*. The former that consists of monomers of only one charge sign takes an elongated conformation at equilibrium due to electrostatic repulsive force, which is usually surrounded by a cloud of neutralizing counter-ions. The structure of the latter,

that includes nearly equal number of positively and negatively charged monomers, can be quite variable upon charge sequences, temperature and existence of salt ions.

With regard to polyampholytes, most of the recent studies are concerned with the quenched ones whose charge state and sequence are predetermined by the synthesis chemistry[1]. The properties of these polymers were extensively studied experimentally[1,2], theoretically[3-5], and also numerically[6-9]. In this paper, we present molecular dynamics (MD) simulations[7,8] of single and multichain polyampholytes, and the effect of added salt on them.

The motion of charged polymers in thermal and viscous medium (such as water and alcohol) is described by

$$m\frac{d\mathbf{v}_i}{dt} = \mathbf{F}_{LR}(\mathbf{r}_i) - \left(\frac{3k_BT}{a^2}\right)(2\mathbf{r}_i - \mathbf{r}_{i+1} - \mathbf{r}_{i-1}) + \mathbf{F}_{th} - \nu m\mathbf{v}_i, \tag{1}$$

$$\frac{d\mathbf{r}_i}{dt} = \mathbf{v}_i. \tag{2}$$

These are the set of Newton-Langevin equations for N monomers. Here, $\mathbf{r}_i$ and $\mathbf{v}_i$ are the position and velocity of the i-th monomer ($i = 1 \sim N$) at time t, respectively, m the monomer mass, a the normalization length close to the bond length, and ν the friction constant.

As shown above, we have four force terms acting on the monomers. First, the long-range Coulomb force $\mathbf{F}_{LR}$ is calculated by direct sums among the monomers,

$$\mathbf{F}_{LR}(\mathbf{r}_i) = \sum_j Z_i Z_j e^2 \frac{\hat{\mathbf{r}}_{ij}}{\epsilon|\mathbf{r}_i - \mathbf{r}_j|^2}, \tag{3}$$

where $Z_i e$ is charge state, and $\hat{\mathbf{r}}_{ij}$ a unit vector along $(\mathbf{r}_i - \mathbf{r}_j)$. The second force arises from connection of adjacent monomers. The average bond length, which can be arbitrary in Eq.(1), is held nearly constant due to entropic nature of elasticity adopted in the equation. On top of them, random thermal kicks $\mathbf{F}_{th}$ and momentum absorption are executed by surrounding medium to equilibrate polyampholytes in solution. In order to handle monomer collisions, exclusion volume with radius a_{col} is introduced, instead of the Lennard-Jones potential force. For such cases, the time step of molecular dynamics simulation $\Delta t = 0.02\omega_p^{-1}$ is adequate, where $\omega_p \cong (2\pi e^2/ma^2)^{1/2}$ is the plasma frequency (typically, for the CH_2 monomer in pure water, $1\omega_p^{-1} \sim 0.1$ ps).

The most important controlling parameter in Eq.(1) is the electrostatic coupling constant Γ (or temperature T), which is defined by

$$\Gamma = e^2/\epsilon a k_B T. \tag{4}$$

Other implicit parameters are the exclusion radius of monomers, the number of chains and monomers, and charge sequence of the chains. The polyampholyte used in this

study consists of randomly co-polymerized one or several chains, each of which includes both positive and negative monomers. More specifically, the sum of all the charges, $Q = \sum_{i=1}^{N} q_i$, is first determined, but the sequence of charges are made quite at random on any of the chains by shuffling procedure. Thus, individual chain has typically the net charges of $\pm eN^{1/2}$. As will be shown in Sec.II and III, the typical equilibration time is $200 \sim 300\omega_p^{-1}$, which corresponds to $20 - 30$ picoseconds. Simulation runs are performed for nearly twice this period.

II. Single-Chain Polyampholytes

The effect of unbalanced charges on the structure of polyampholytes[7] is depicted in Fig.1, where equilibrium conformations in the bird's-eye view plots and time histories of the gyration radius,

$$R_g = \left(\frac{1}{N} \sum_{j=1}^{N} (\mathbf{r}_j - < \mathbf{r} >)^2 \right)^{1/2} , \tag{5}$$

are shown on the left and right columns, respectively, for medium temperature $T/T_0 = 1/2$ (see Fig.2). The amount of excess charge $\delta N = N_+ - N_-$ on the chain is (a) below,

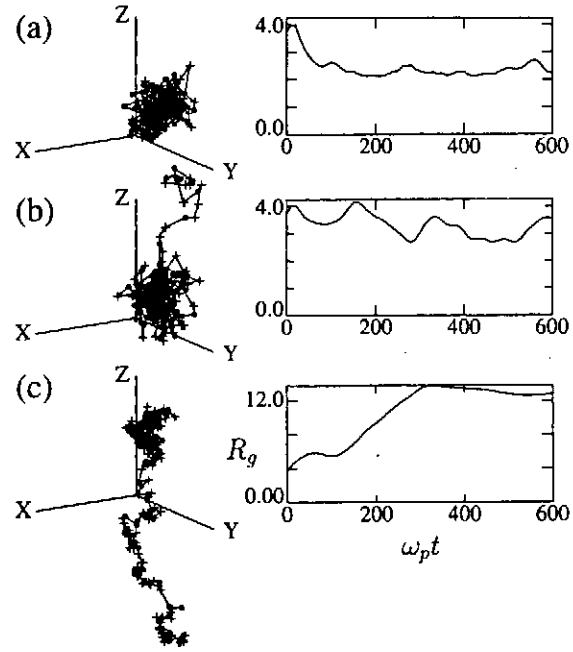

Fig.1. The effects of unbalanced charges are shown by equilibrium conformations (left column) and time histories of gyration radius (right column), for (a) nearly neutral, (b) mirginal, and (c) non-neutral cases. The polyampholytes here consist of randomly co-polymerized 256 monomers of either positive or negative charges, with temperature $T = \frac{1}{2}T_0$ (T_0 is the temperature for which the Coulomb energy equals the thermal energy, and ω_p the plasma Langmuir frequency). The conformation (c) is reduced to 53% that of the real size.

(b) just, and (c) above the critical value $\delta N_0 = N^{1/2}$. When the charge imbalance is smaller than $N^{1/2}$, the polyampholyte chain collapses to form a globule. The relaxation time is roughly $200\omega_p^{-1}$. This relaxation time falls in a few tens of *picosecond* range for the CH_2 monomer in pure water ($\epsilon = 80$). Above the critical charge imbalance, the chain takes a stretched conformation that resembles that of polyelectrolytes.

The temperature dependence of the gyration radius is shown in Fig.2 for balanced (neutral) polyampholytes. The gyration radius increases with temperature. We find the low ($T < T_0$), medium, and high ($T > T_0$) temperature regimes, where the base temperature T_0 is defined by $\Gamma = e^2/\epsilon a T_0 = 1$. These regimes are characterized by a dense globule, a loose globule, and an elongated Gaussian coil, respectively. The elongated coil at high temperature is not stationary, but it repeats contraction and stretching motions.

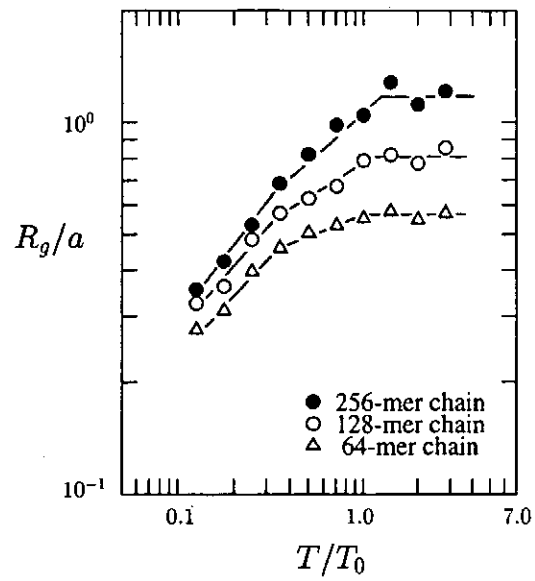

Fig.2. Temperature dependence of gyration radius is shown for neutral single-chain polyampholytes of 64, 128, and 256-mers. Three regimes are identified at high ($T/T_0 \geq 1$), medium, and low ($T/T_0 \leq 0.3$) temperatures. The latter two are the regimes in which the Coulomb force organizes the structure of polyampholytes. The low temperature regime, which is due to intensive folding of the chain, was first obtained by the present molecular dynamics simulation of non-lattice type.

The above high and medium temperature regimes correspond, respectively, to *the high and low temperature regimes* of the Flory theory[4] for the Θ solvent. The dense globule at low temperature, which results from intensive folding of the chain – in good analogy with *protein folding*[10], was first obtained by the MD simulation of non-lattice

type[7]. The velocity distribution of the monomers is almost Gaussian $\exp(-v^2)$, which shows thermal equilibration of the globule.

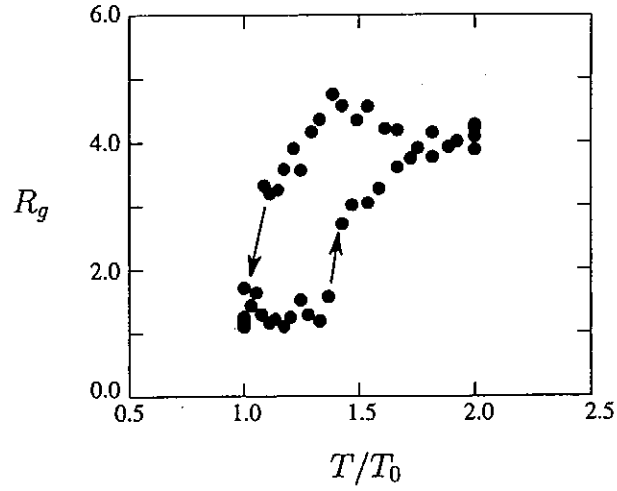

Fig.3. A hysteresis for the gyration radius is observed against slow cyclic changes in temperature under the Coulomb and attractive short-range forces. In the heating phase, the gyration radius takes the lower branch, whereas it goes along the upper branch in the cooling phase (a neutral, single 64-mer polyampholyte is used).

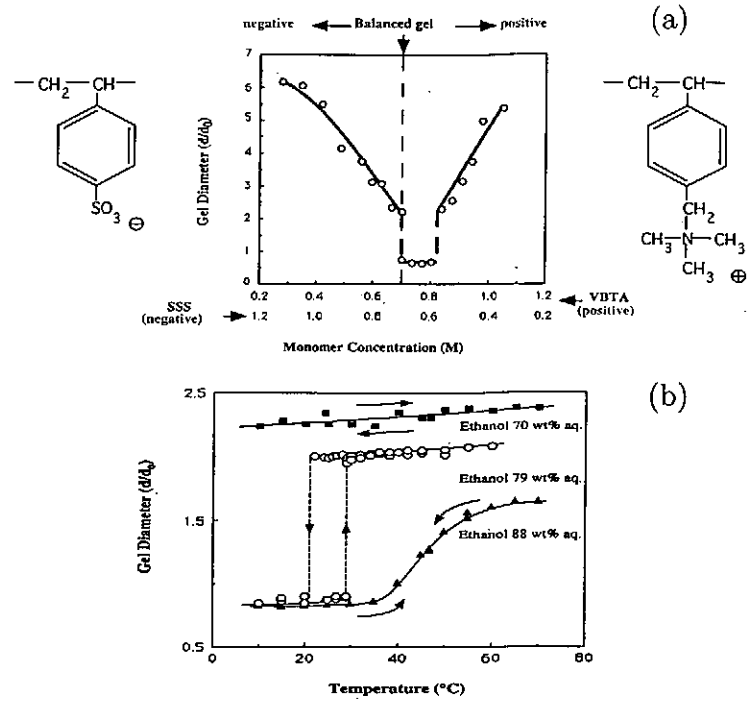

Fig.4. (a) Degree of swelling of SSS-VBTA gels in pure water as a function of monomer composition, and (b) the temperature dependence of the AMPS/MAPTA polyampholyte gels. The 79 wt% ethanol shows the first order transition with hysteresis[11] (after Dr.Y.Takeoka).

The volume of neutral polyampholyte undergoes a hysteresis against slow cyclic changes in temperature when the long-range Coulomb force and short-range attraction force cooperate[7]. If we start from a compact globule at low temperature in Fig.3, the polyampholyte chain keeps a small volume until a critical temperature $T = T_1$ is reached, at which the volume jumps up due to unfolding of the chain. In the cooling phase back from high temperature ($T > T_0$), the volume takes a larger value than for the heating phase until the chain suddenly collapses to a globule at $T = T_2$, with $T_1 > T_2$. This phenomenon reveals existence of double local energy minima around the critical temperature. Despite the hysteresis, the whole process is reversible (the path loop is closed) unless a dissipation term other than viscosity is introduced in Eq.(1).

Volume swelling under the non-neutrality condition and also the hysteresis against temperature changes have recently been observed in charged gels experiments[11]. Gels are network polymers that contain large amount of water inside, which causes drastic swelling of gels. The gels used in the experiments are stylene sulfate SSS which is negatively charged and vinyl benzen trimethylanmonium VBTA which is positively charged. They are mixed and combined with a cross-linker in water. Figure 4(a) shows the gel diameter as a function of SSS-VBTA mixing ratio. These PA gels with small side chains are collapsed under a certain amount of charge imbalance, and they get swollen when the net charge within the gels exceeds the critical value. The gel volume dependence on the charge imbalance closely resembles that of the polyampholytes by the molecular dynamics simulations shown in Fig.3.

Figure 4(b) shows the first-order transition of the diameter of the AMPS:MAPTA= 40:60 gels against temperatures. The experiment for the gel processed in 79wt% ethanol shows the transition with hysteresis. This hysteresis is close to the molecular dynamics study of neutral polyampholyte under the Coulomb force and the short-range attraction force[8].

III. Multi-Chain Polyampholytes

The time histories of the gyration radius of the whole system (chains) $R_{g,sys}$, the average of gyration radii of the chains R_{g1}, and the x-component velocity of one specific monomer are shown in Fig.5 for the multichain polyampholyte at high temperature[8]. Here, the polyampholyte is composed of eight 32-mer chains, each of which has net charge because of random charge sequences. The gyration radius of individual chain does not change appreciably, while the system gyration radius increases more in extent to a wall-bound equilibrium in $\tau_{eq} \sim 200\omega_p^{-1}$. The large increase in the size of polyampholyte is attributed to separation of the chains, which is a new feature of *multichain*

polyampholyte compared to the single-chain one.

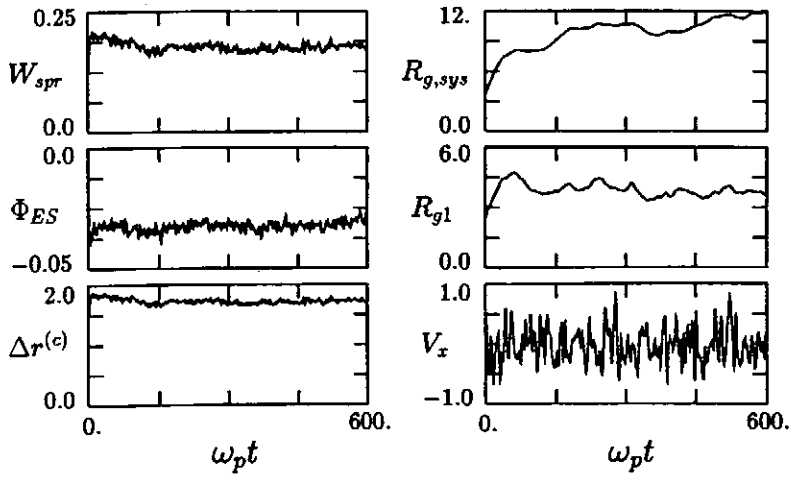

Fig.5. Time histories of the average elastic energy per monomer W_{spr}, the Coulomb energy per monomer Φ_{ES} normalized by the base thermal energy T_0, the average bond length of connected monomers $\Delta r^{(c)}$, the system gyration radius including all the monomers $R_{g,sys}$, the average of gyration radius of chains $R_{g,1}$, and one component of monomer velocity V_{x1} are shown for the multichain polyampholyte consisting of randomly co-polymerized eight chains of 32-mers. The temperature is $T/T_0 \sim 1$.

The typical conformations of multichain polyampholytes are shown for (a) high ($T/T_0 \sim 1$), and (b) low ($T/T_0 = \frac{1}{8}$) temperatures in Fig.6. The one-phase state at high temperature consists of wall-bound separated chains with a large void space among the chains. On the other hand, the segregated phase at low temperature is characterized by a collapsed globule resembling that of a single-chain polyampholyte. At high temperature, the gyration radius R_{g1} of each chain and the velocity of monomers undergo slow oscillations compared to the friction time ν^{-1}. The oscillations of R_{g1} which arises from folding /unfolding motions of the chains occur simultaneously with gather and scatter motions of the chains. On the other hand, at low temperature in (b), the gyration radius R_{g1} does not show oscillations, which implies the glass nature of a collapsed globule[8].

A brief summary is placed here on the effect of specific charge sequences[8]. Thermodynamically, it was shown that a charged polymer with an alternating sequence is very different from the one with random charge sequence[5]. The present MD simulation finds that this is true for multichain polyampholytes with a completely alternating sequence. However, polyampholyte with a longer alternating interval whose block length (of the equal-sign charged monomers) is as small as four already behaves like polyampholyte with random sequence[8]. Therefore, only the charge sequence of the block length one or

two should be regarded as special.

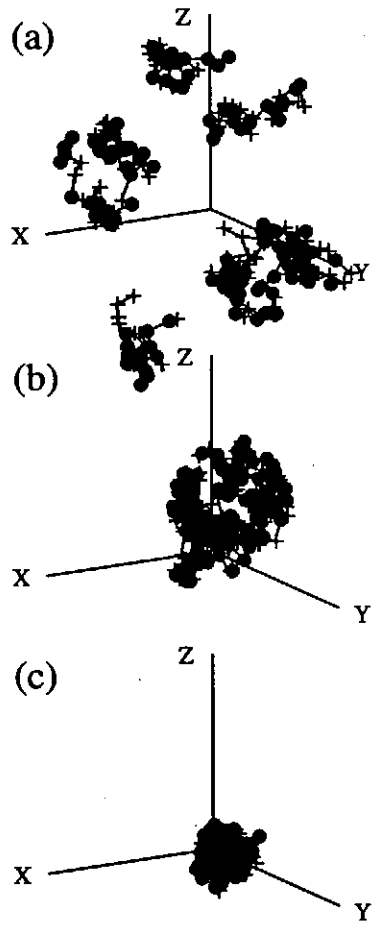

Fig.6. The typical relaxed conformations of multichain polyampholytes are shown for (a) high ($T/T_0 = 1$), (b) medium ($T/T_0 = 1/4$), and (c) low ($T/T_0 = 1/8$) temperatures. We obtain the one-phase state with wall-bound separated chains for (a), and the segregated phase with a compact globule in (c). The phase transition occurs at the temperature slightly below that of (b).

The gyration radius and the filling index $\zeta = N_c^{1/3} R_{g1}/R_{g,sys}$ (N_c: the number of chains) of multichain polyampholytes depend on stiffness, molecular weight and the number of the chains. The critical temperature at which chain overlapping begins is proportional to the molecular weight of the chains, $T_* \sim M_w$. Detailed results are described in Ref.8.

IV. The Effect of Salt

Addition of salt to polyampholyte solution is known to enhance its dissolution in pure water[1], and to control DNA configurations in living cells[12]. A new set of molecu-

lar dynamics simulations are performed for the system consisting of multichain polyampholyte and free salt ions[8]. The salt ions are represented by the same number of positive and negative free counter-ions whose mass and charge are identical with those of the polyampholyte monomers. A typical equilibrium conformation of the polyampholyte is depicted in Fig.7, where scattered small pluses and dots represent salt ions. The surface of the globule in Fig.7(b) now becomes quite fuzzy due to the presence of large number of the salt ions. This is clearly contrasted to the dense globule shown in Fig.7(c) without salt under the same temperature.

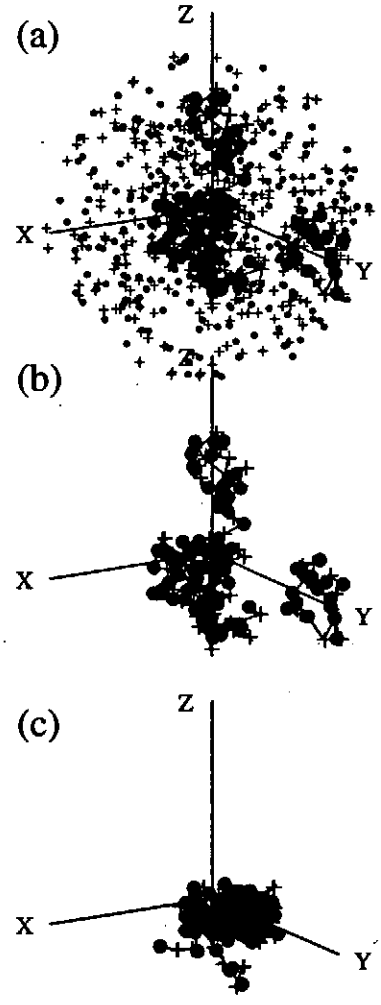

Fig.7. Typical relaxed conformation of randomly co-polymerized polyampholyte (six 32-mers) in salt-added solution for temperature $T/T_0 = 1/8$: (a) polyampholyte and salt ions; (b) only the polyampholyte. The positive and negative salt ions are marked with + and •, respectively. The ralaxed conformation for the salt-free case is shown in (c).

The denseness of the polymer chains (or, the degree of chain overlapping) is well quantified by the *filling index* $\zeta = N_c^{1/3} R_{g1}/R_{g,sys}$, where N_c is a number of chains

composing of the polyampholyte, R_{g1}, $R_{g,sys}$ the gyration radii of each chain and all the chains, respectively. This value equals or exceeds unity, $\zeta \geq 1$, when the chains closely overlap each other; it becomes small for the polymers of separated chains. Thus, we can judge that *the polymer is soluble* if the filling index becomes less than unity, $\zeta < 1$.

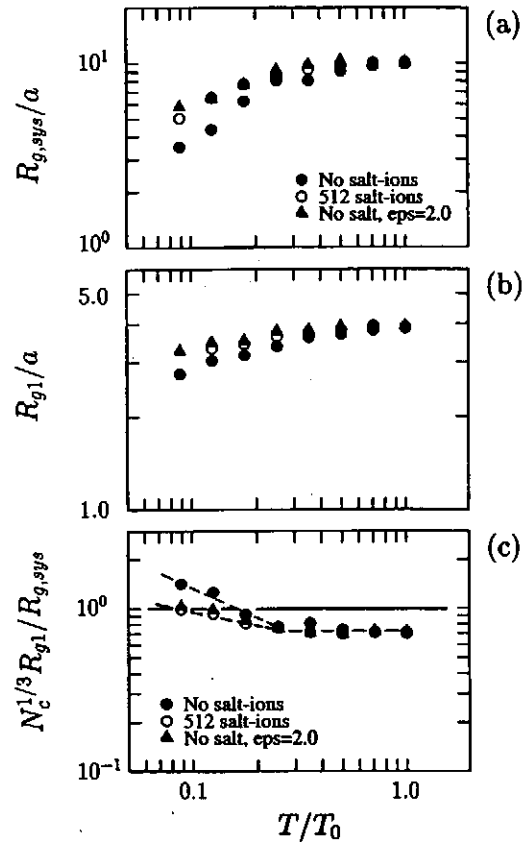

Fig.8. Effect of salt addition for the case with 512 salt ions (256 positive and negative free ions), and for the case of enhanced electrical permitivity $\epsilon = 2\epsilon_0$ without salt ions. The polyampholyte is composed of randomly co-polymerized six 32-mers, and the panels show (a) the system gyration radius $R_{g,sys}$, (b) the average gyration radius of the chains R_{g1}, and (c) the filling index $N_c^{1/3}R_{g1}/R_{g,sys}$.

Figure 8 shows the filling index ζ for the multichain polyampholytes in salt-free solvent (triangles), and in salt-added solution (filled and open circles). Quite evidently, the value of the filling index is reduced in solutions with salt ions. The charge density with 512 salt ions (256 positive and 256 negative ions) is comparable to that of the polyampholyte inside the globule. Half the density of the salt ions is still effective at high temperature, as the polyampholyte takes a larger volume to have less charge density; it is less effective at low temperature. As has been shown clearly in Fig.8, the

added salt ions act to screen the attractive electric field and separate the chains, which causes dissolution and swelling of polyampholytes[5,8].

The effect of salt can be approximately treated by means of enhanced electrical permitivity ϵ in Eqs.(1)-(3). However, at low temperature when a dense globule has been formed, the subtlety of added salt including the relaxation time is properly described only with the use of molecular dynamics simulations[8]. For example, unfolding of the globule due to addition of salt occurs by one order of magnitude more slowly than for the case with enhanced electrical permitivity. This is because the size of the salt ions is non-negligible compared to that of the void space among chained monomers of polyampholytes.

References

1. References in F.Candau and J.F.Joanny, *Encyclopedia of Polymeric Materials, 7,* 5476 (edited by J.C.Salomone, CRC Press, Boca Raton, 1996).
2. J.M.Corpart and F.Candau, *Macromolecules, 26,* 1333 (1993).
3. P.G.Higgs and J.-F.Joanny, *J.Chem.Phys., 94,* 1543 (1990).
4. A.V.Dobrynin and M.Rubinstein, *J.de Phys.II, 5,* 677 (1995).
5. R.Everaers, A.Johner, and J.-F.Joanny, *Macromolecules, 30,* 8478 (1997).
6. Y.Kantor, M.Kardar and H.Li, *Phys.Review, E49,* 1383 (1994).
7. M.Tanaka, A.Yu Grosberg, V.S.Pande, and T.Tanaka, *Phys.Review, E56,* 5798 (1997).
8. M.Tanaka, A.Yu Grosberg, and T.Tanaka, *J.Chem.Phys., 110, 8176 (1999).*
9. T.Soddemann, H.Shiessel and A.Blumen, *Phys.Review E57, 2081 (1998).*
10. *Protein Folding*, edited L.M. Gierasch and J. King (Amer. Assoc. for Advance. Sci., Washington D.C., 1989).
11. Y.Takeoka, A.Berker, T.Enoki, A.Grosberg, M.Kardar, T.Oya, K.Tanaka, G.Wang, X.Yu, and T.Tanaka, *Phys.Rev.Lett., 82,* 4863 (1999).
12. S.Takagi and K.Yoshikawa, *Langmuir 15,* 4143 (1999).

Stepwise Collapse of Polyelectrolyte Chains Entrapped in a Finite Space

Seiji Takagi,[†] Kenichi Yoshikawa[‡]
[†]Graduate School of Human Informatics, Nagoya University, Nagoya 464-0814, Japan
[‡]Department of Physics, Faculty of Science, Kyoto University, Kyoto 606-8502, Japan

Abstract

We performed a theoretical study on the nature of the collapsing, or folding, transition of polyelectrolyte chains entrapped in a narrow closed space, as a model of living cells enclosing giant DNA chains. We adopted a theoretical treatment with a mean-field approximation by taking into account the effect of the translational entropy of small ions. For a system with two, long and short, chains trapped in a narrow space, we found that, with an increase in the concentration of an added trivalent cation, P^+, the short chain collapses first while the long chain remains an elongated coil. With increased P^+, the long chain collapses while the short chain decollapses. Finally, with an excess of P^+, both the short and long chains collapse. For a system with stiff and flexible chains, with increased P^+, the flexible chain collapses while the stiff chain remains an elongated coil. With increased P^+, both the stiff and flexible chains collapses. The state with collapsed stiff chain and elongated flexible chain is metastable state for the whole concentration region of trivalent cation. It may be worth examining such theoretical expectations by actual experiments.

Introduction

In living cells, DNAs on the order of $10^2 - 10^4 \mu$m long are usually packed in a narrow closed space on the order of only $0.1 - 1\mu$m, *i.e.*, the cytoplasmic space in prokaryotes and the nucleus in eukaryotes. The information stored in the sequence of bases along the DNA chain is transformed into proteins based on the code stored in RNA.[1] The entire process of information transduction from DNA to protein molecules is referred to as "gene expression". It is obvious that the tightly packed DNA chains in the intracellular environment must unfold to perform gene transcription from DNA into RNA *i.e.*, dissolution, or unfolding, of the compact DNA chain is necessary for "gene expression".

The purpose of the present article is to report a working hypothesis to interpret the underlying physicochemical mechanism of the selective unfolding, or decollapsing, of multiple different DNAs enclosed within the intracellular space. In many living cells, not only the molecular weight but also the base composition (G/C content) is different between coexisting DNAs. To simplify the discussion,in the present report we will consider a system with two, long and short (stiff and flexible), polyelectrolyte chain with the same stiffness (contour length).

It is well known that the condensation of DNA molecules is highly cooperative.[2] Recently, based on the observation of single DNA chains, it has been found that a single duplex DNA chain undergoes a large discrete transition, or a first-order phase transition, from a spatially elongated unfolded state to a collapsed folded state (coil-globule transition) with the addition of various kinds of condensation agents, including multivalent cations such as polyamine polyamines[3,4] or metal ions,[5] neutral flexible polymers,[6] cationic surfactants[7] and alcohols.[8] Among the various condensation agents, polyamines are chemical species that exist generally both in prokaryotes and eukaryotes. Based on theoretical and experimental studies of the mechanism of DNA collapse induced by polyamines, it has become clear that ion-exchange between a monovalent cation and a multivalent cation plays a crucial role on this transition.[3-5] The physico-chemical mechanism of the collapsing transition induced by a multivalent ion can be summarized as follows. Through exchange with multivalent cations, many monovalent cations are released from within the effective volume of an unfolded DNA chain into the external solution, and this effect causes a large increase in entropy in the system. In other words, ion-exchange between monovalent and multivalent cations induces an osmotic pressure that favors a decrease in the size of elongated coiled DNA. When the effect of the increase in the translational entropy of the counter ions overcomes the destabilization due to the increase in elastic energy, a long DNA chain undergoes a collapsing transition from an elongated coil to a folded compact state. Based on this representation of the collapsing transition as a kind of first-order phase transition in a mesoscopic system, it is naturally expected that the change in the volume of the aqueous environment enclosing the DNAs should have a crucial effect on the collapsing transition.

Especially, if the space enclosing the DNAs is small, the entropy gain due to ion-exchange is small. As a result, the nature of the collapsing transition of DNAs in a μm space, as in a living cellular environment, should be markedly different from that observed on a mm-scale in a test tube. Furthermore, when multiple DNAs exist in such a narrow space, the interaction between the DNAs through the exchange of counter ions and multivalent ions should significantly affect the nature of the collapse transition. The purpose of the present article is to report a theoretical prediction of the nature of the collapsing transition for multiple DNA chains entrapped in a narrow space in relation to the abovementioned problem in biology. In the next section, we give the free energy of a system of polyelectrolytes in a finite volume taking into account the contributions of the translational entropy of monovalent and trivalent ions and also the exchange of counter ions between different polyelectrolyte chains. The result obtained for the transition of polyelectrolytes induced by a trivalent cation can be generalized to that induced by divalent and other multivalent ions.[3]

Theory

We consider a closed system of volume Ω, entrapping two polyelectrolyte chains; the 1 chain and the 2 chain consisting of N_1 and N_2 Kuhn segments of length b_1 and b_2, respectively. In this article, two different chain conditions are studied for this system: (i)long and short chains with the same stiffness; $N_1 b_1 > N_2 b_2$ and $b_1 = b_2$, (ii)stiff and flexible chains with the same contour length; $N_1 b_1 = N_2 b_2$ and $b_1 > b_2$. In DNA, the length b and width d of a Kuhn segment are usually ca. 100 nm and 2 nm, respectively. DNA chains, howeve, exhibit rather marked diversity with regard to their base composition, or G/C content. The G/C-rich part is stiffer than the A/T-rich part, in other words persistence length of G/C-rich part is longer than that of the A/T-rich part.[10] Therefor, in case of (i) there is no difference in the base composition between two cahins, while in case of (ii) the ratio of G/C pair of the 1 chain is less than that of the 2 chain. The "effective charges" in the 1 and 2 chains are Q_1 and Q_2, and the total number of monovalent cations as counter ions are $Q_1 + Q_2$, where the "effective charge" reflects the number of monovalent cations exchangeable with trivalent cations associated with the collapsing transition. Thus, the Q values never directly correspond to the number of free negative phosphate charges, as in the counter ion condensation theory.[11] Thus, the Q values are related to the net change in the translational entropy that accompanies the collapsing transition. Based on a recent experimental study[12] concerning the effect of temperature on the collapsing transition of T4 duplex DNA, 166kbp or $32 \cdot 10^3$ phosphate groups, induced by the addition of a trivalent ion, spermidine, the net entropy change is $32k$ per DNA chain. This result implies that the "effective charge", or the number of exchangeable ions, can be estimated to be on the order of several tens, as adopted in the parametrization of Q in the present article. A detailed analysis of the individual contributions to the change in entropy in the collapsing transition has been presented elsewhere.[12] For simplicity, the direct interaction between the 1 and 2 chains is neglected, *i.e.*, the total effective volume of the chain is smaller than Ω (see Fig. 1(a)). The total free energy of the system is written as,

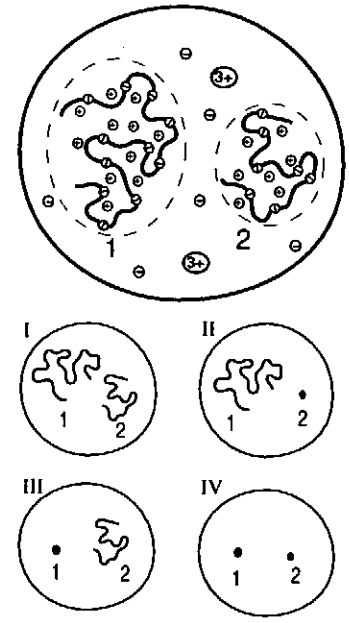

Figure 1 : (a) Model system of a cell containing short and long (stiff and flexible) DNA chains. (b) Four different states for the conformations of the 1 and 2chains.

$$F_{total} = F_1 + F_2 + F_{ext} \tag{1}$$

where F_{ext} is the free energy in the solution outside the effective volume of the chains. F_1 and F_2 are the free energies within the region of the effective volume in the individual polyelectrolyte and consist of four different components: elastic energy F^{ela}, interaction between the segments F^{int}, entropic term due to the translational freedom of small ions F^{trans}, and electrostatic

energy F^{ele}.

$$F_i = F_i^{ela} + F_i^{int} + F_i^{trans} + F_i^{ele} \quad (i = 1, 2) \qquad (2)$$

The 1 and 2 chains have contour lengths of $N_1 b_1$ and $N_2 b_2$, respectively. For rather long polyelectrolytes, such as a DNA molecule of more than several tens of kilobase pairs, the electrostatic term, F_i^{ele}, would become relatively smaller than the other terms, for the following reason.[3] In the elongated state, the distance between the segments in a chain is on the order of 10^2-10^3nm, while the Debye length is on the order of 1nm, and quasi-electroneutrality in the effective volume of the DNA coil will hold. Accordingly, the contribution of this electrostatic term is almost negligible. In the collapsed state, due to charge neutralization with the enhanced binding of the counter ions, the electrostatic repulsion between the bare negative charges along the DNA chain again becomes less important. In other words, the essence of the electrostatic term can be incorporated into the interaction term, F_i^{int}. Thus, we do not consider F_i^{ele} in an explicit manner.

The elastic free energy, F_i^{ela}, is described by the entropy loss due to deformation from the Gaussian coil.[13]

$$F_i^{ela}/kT = \frac{3}{2}(\alpha_i^2 + \alpha_i^{-2}) \qquad (3)$$

where k is the Boltzmann constant, T is temperature, α is the swelling coefficient of the chain, $\alpha_i = (V_i/V_i^0)^{1/3}$, V_i is the effective volume of a chain, and V_i^0 is the volume of a Gaussian chain, $V_i^0 = 4\pi/3(b_i N_i^{1/2})^3$.

The free energy of interaction, F_i^{int}, between segments of the chain is given in the form of a virial expansion for the concentration of segments within the effective volume of the chain, $n_i = N_i/(V_i^0 \alpha_i^3)$.

$$F_i^{int}/kT = N_i(Bn_i + Cn_i^2) \qquad (4)$$

where B and C are the second and third virial coefficients.[9] To focus on the effect of the change in translational entropy that accompanies ion-exchange and on the interaction between chains through mono- and multivalent cations, we simply set these values constant: $B/b^3 = -0.15$ and $C/b^6 = 0.01$ for the case (i), as in previous studies.[13] For the case (ii), the relation, $B_1/B_2 = (b_1/b_2)^2$ and $C_1/C_2 = (b_1/b_2)^3$ are used.[9] With the combination of the elastic and interaction terms, F_i^{ela} and F_i^{int}, one can dipict the double minimum in the free energy for a giant DNA.[3-8,12,13] In other words, the Coulombic term can be effectively renormalized with this simple theoretical model, including the effect of charge neutralization in the collapced DNA.[8,12]

The free energy, F_i^{trans}, represents the translational entropy[6] of small ions moving inside the effective volume of the chain, while the third term, F_{ext} in eq. 1, represents the translational entropy of small ions in the free space of the solution outside the space occupied by the chains.

$$F_i^{trans}/kT = q_i \ln\left(\frac{q_i}{V_i}\right) + p_i^+ \ln\left(\frac{p_i^+}{V_i}\right) + p_i^- \ln\left(\frac{p_i^-}{V_i}\right) \qquad (5)$$

$$F_{ext}/kT = q_{ext} \ln\left(\frac{q_{ext}}{V_{ext}}\right) + p_{ext}^+ \ln\left(\frac{p_{ext}^+}{V_{ext}}\right) + p_{ext}^- \ln\left(\frac{p_{ext}^-}{V_{ext}}\right) \qquad (6)$$

where q_i, p_i^+ and p_i^- are respectively the number of counter ions of the monovalent cations, trivalent cations and monovalent counter anions inside the effective volume of one chain, while q_{ext}, p_{ext}^+ and p_{ext}^- are the corresponding ion numbers in the external solution and V_{ext} is the volume of free solution, *i.e.*, $V_{ext} = \Omega - V_1 - V_2$. Based on the principle of the conservation of the particles, the following relationships are obtained $q_1 + q_2 + q_{ext} = Q_1 + Q_2$, $p_1^+ + p_2^+ + p_{ext}^+ = P^+$, $p_1^- + p_2^- + p_{ext} = P^-$, where P^+ and P^- are the total number of trivalent cations and their counter ions, *i.e.*, $P^- = 3P^+$. For the region near the polyelectrolyte, the electroneutrality condition yields

$$3p_i^+ + q_i = Q_i + p_i^-. \qquad (7)$$

The equilibrium number of each ion is defined by minimizing the total free energy of the system with respect to q_1, q_2, p_1^+, p_2^+. In this context, near the critical concentration of trivalent cations, the free energy profile for one polyelectrolyte has double minima for $\alpha < 1$ and $\alpha > 1$, corresponding to the collapsed compact globule and spatially elongated unfolded coil states, respectively. The total free energy of the system is calculated for the four possible states in the system; (1 chain, 2 chain) = (coil, coil) as state I, (globule, coil) as state II, (coil, globule) as state III and (globule, globule) as state IV; cf., Fig. 1(b).

Results and Discussion

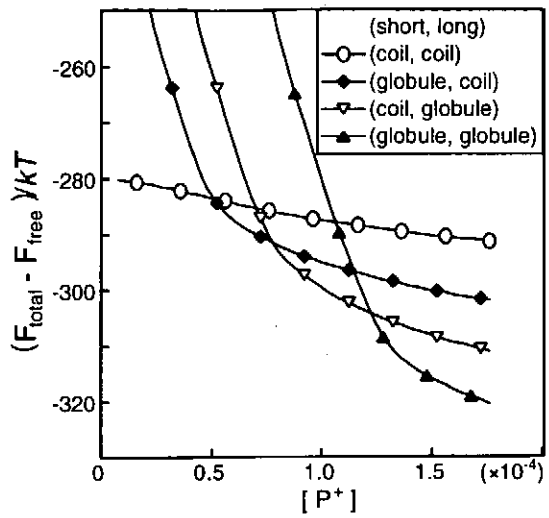

Figure 2 : Change in the free energy for the four different states with the concentration of the trivalent cation $[P^+]$. F_{total} and F_{free} are the free energy in the system as depicted as in (a) and that in the solution of the trivalent cation in the absence of polyelectrolyte chains, respectively. The number of Kuhn segments in the 1 and 2 chains are 150 and 100, respectively.

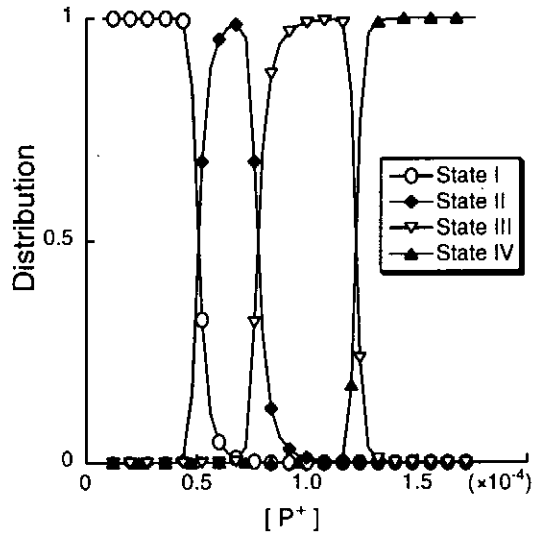

Figure 3 : Probability distributions of the four different states with a change in the concentration of a trivalent ion, as deduced from the result given in Fig. 2.

i. Long and short chains. Figure 2 shows the result of the numerical calculation for the total free energy of the system , where $N_1 = 150$, $N_2 = 100$, $Q_1 = 30$, $Q_2 = 20$ and $\Omega = 10(V_1^0 + V_2^0)$. The longitudinal axis gives the difference in free energy between F_{total} (see eq. 1) and F_{free}; F_{free} is the free energy for the system with free volume Ω where the concentration of the trivalent cation is $[P^+]$, and that of the monovalent counter anion is $[P^-]$ ($[P^-] = 3[P^+]$), in the absence of any polyelectrolyte chain. When the concentration of the trivalent ion $[P^+]$ is low, both the long and short chains take the elongated coil conformation. When the concentration of the trivalent ion $[P^+]$ is large enough, both chains take the collapsed compacted conformation as the state at

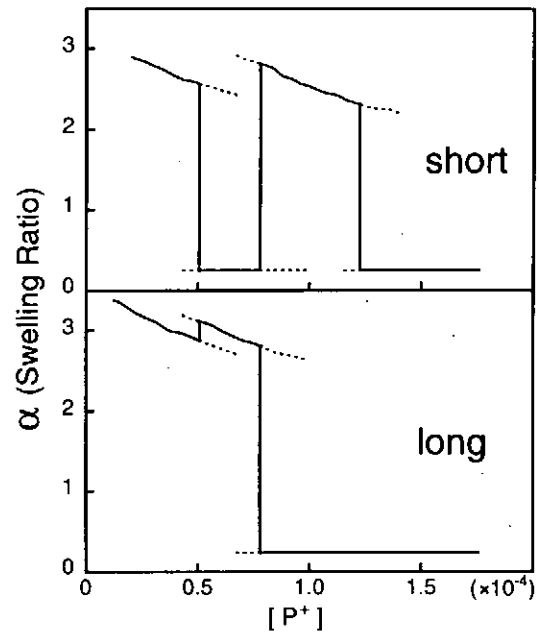

Figure 4 : Change in the swelling ratio α in the short and long chains with the concentration of the trivalent cation. The solid line indicates the state with the free energy minimum.

the free energy minimum. At the intermediate concentration for $[P^+]$, one chain takes a coil conformation and the other takes a collapsed conformation. Interestingly, the short chain collapses and the long chain remains a coil when $[P^+]$ is 0.5–0.8 ($\times 10^{-4}$). On the other hand, when $[P^+]$ is 0.8–1.2 ($\times 10^{-4}$), the state with a coiled short chain and a collapsed long chain becomes most favorable with respect to the free energy.

Based on the result for the free energy given in Fig. 2, Fig. 3 shows the probability distributions for the four different states with a change in the concentration of the trivalent cation. The symbols in Fig. 3 are the same as those in Fig. 2. The the long and short chains again show an interesting conformational behavior. Due to the effect of thermal fluctuation, different states coexist in the transition regions. However, all of the four different states are almost "pure" at different P^+ concentrations.

Figure 4 shows the change in the swelling ratio α of the long and short chains with respect to the corresponding Gaussian conformation. The solid line indicates the swelling ratio for the state with the free energy minimum, and the broken line indicates that for the metastable state.

The curious transition in this system is caused by the difference in the gain in translational entropy necessary for the collapse transition between the shorter and longer chains, and also by the interaction between chains through the solution.

ii. Stiff and flexible chains. Figure 5 shows the result of the numerical calculation for the total free en-

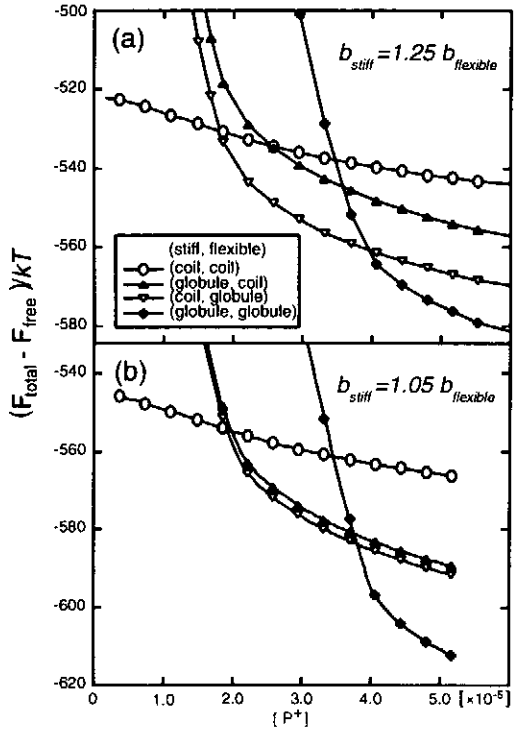

Figure 5 : Change in the free energy for the four different states with the concentration of the trivalent cation $[P^+]$. (a)$N_1 = 160$, $N_2 = 200$, $b_1 = 1.25b_2$,(b)$N_1 = 200$, $N_2 = 210$, $b_1 = 1.05b_2$, $b_2 = 100nm$.

ergy of the system : (a)$N_1 = 160$, $N_2 = 200$, $b_1 = 1.25b_2$ and (b)$N_1 = 200$, $N_2 = 210$, $b_1 = 1.05b_2$, therefor the 1 chain is stiff and the 2 chain is flexible. Both axes in Fig.5 are the same as those in Fig.2. When the concentration of the trivalent ion $[P^+]$ is low, both the stiff and flexible chains take the elongated coil conformation. When the concentration of the trivalent ion $[P^+]$ is large enough, both chains take the collapsed compacted conformation as the state at the free energy minimum. At the intermediate concentration for $[P^+]$, the flexible chain takes collapsed state and the stiff chain takes elongated coil state, while the state with collapsed stiff chain and elongated flexible chain is metastable over the whole concentration for $[P^+]$.

Figure 6 shows the probability distributions for the four different states with a change in the concentration of the trivalent cation. For the condition (a), in which difference in the stiffness of the chain is large, probability of the state (stiff, flexible)=(globule, coil) is almost zero at any concentration of $[P^+]$, and the other three different states are almost "pure" at different $[P^+]$ concentrations. For the condition (b), Kuhn length of stiffer cahin is only 1.05 times longer than that of flexible chain, the difference in the free energy between the states (stiff, flexible) = (coil, globule) and (globule, coil) becomes several times kT, and hence these two states

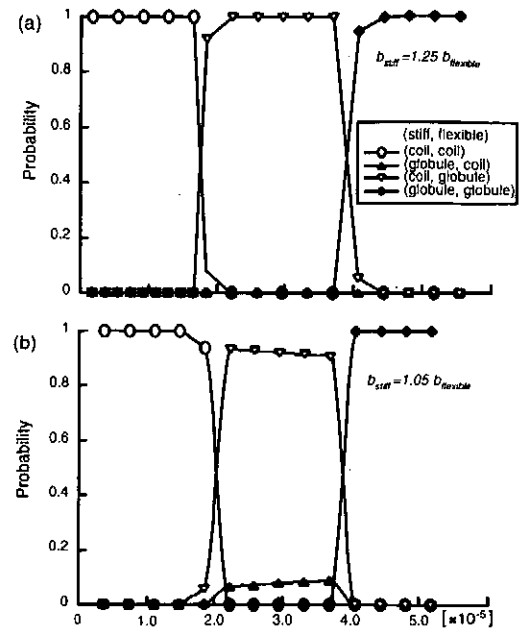

Figure 6 : Probability distributions of the four different states with a change in the concentration of a trivalent ion, as deduced from the result given in Fig. 5.

are indefinite states, when $[P^+]$ is 0.2–0.4 ($\times 10^{-4}$). The difference in Kuhn length is small, only 5 percent, while the difference in the probability of the state (coil, globule) is about 9 times larger than that of the state (globule, coil). This result shows that the difference in the stiffness of DNA molecule, or G/C content, affects largely the collapse transition, in other words the stiffer chain, or G/C-rich chian, tend to unfold with decrease of $[P^+]$.

This result indicates that it is possible to select the chain to unfoled or collapse among plural polyelectrolyte chains with different length and stiffness by the control of concentration of trivalent cation. In actual living cells, as mentioned before, DNA chains exhibit rather marked diversity with regard to their base composition. Besides, there is the band pattern on the chromosome dyed by the dye specific for A/T-pair.[1] Accordingly, it is possibly considered that the length and the stiffness of a chain, or portion, is concerned with the selective unfold of DNA molecule.

Although the present theoretical study is only preliminary, the hypothesis proposed in this article may contribute to understanding the experimental observations on the dynamical change of long DNA chains in living cells. The stepwise folding/unfolding of long DNAs is expected to be closely associated with the mechanism of the self-regulation of gene expression in living systems. This theoretical prediction of exotic behavior in a con-

fined space is not a unique characteristic of DNAs, but rather should be a general feature of polyelectrolytes.

References

(1) Alberts, B., Bray, D., Lewis, J., Martin, R., Roberts, K., Watson, J. D. *Molecular Biology of The Cell*, 3rd ed.; Garland Publishers: New York,1994.

(2) Bloomfield, V. A. *Curr. Opinion Struct. Biol.* **1996**, 6, 334.

(3) Takahashi, M., Yoshikawa, K., Vasilevskaya, V. V., Khokhlov, A. R. *J. Phys. Chem. B* **1997**,101, 9396.

(4) Yoshikawa, Y., Yoshikawa, K. *FEBS Lett.* **1995**,361, 277.

(5) Yamasaki, Y., Yoshikawa, K. *J. Am. Chem. Soc.* **1997**, 119, 10573.

(6) Vasilevskaya, V. V., Khokhlov, A. R., Matsuzawa, Y., Yoshikawa, K. *J. Chem. Phys.* **1995**, 102, 6595.

(7) Mel'nikov, S. M., Sergeyev, V. G., Yoshikawa, K. *J. Am. Chem. Soc.* **1994**, 117, 2401.

(8) Ueda, M., Yoshikawa, K. *Phys. Rev. Lett.* **1996**, 77, 2133.

(9) Grosberg, A. Yu., Khokhlov, A. R. *Statistical Physics of Macromolecules*; American Institute of Physics: New York, 1994.

(10) Hogan, M., LeGrange, J., Austin, B. *Nature*, **1983**, 304, 752.

(11) Manning, G., S., *Q. Rev. Biophys.* **1978**, 2, 179.

(12) Murayama, H., Yoshikawa, K., submitted for publication

(13) Yoshikawa, K., Kidoaki, S., Takahashi, M., Vasilevskaya, V. V., Khokhlov, A. R. *Ber. Bunsenges. Phys. Chem.* **1996**, 100, 876.

Thermodynamics of Folding Phase-Transition of Single T4DNA Molecules in Poly(Ethylene Glycol) Solution

H. Mayama[a,b] and K. Yoshikawa[b]

[a] Institute for Fundamental Chemistry, 34-4, Nishikihiraki-cho, Takano, Sakyo-ku, Kyoto 606-8103, Japan

[b] Department of Physics, Graduate School of Science, Kyoto University, Kyoto 606-8502, Japan

Abstract

Recently, it has been established that single DNA molecule exhibits discrete transition between the elongated coil state and the compact folded state, and that there considerable width on the concentration of condensing agents such as poly(ethylene glycol) and polycations. In this work, we studied the effect of temperature on the bimodal distribution of conformation for the ensemble of T4DNA chains (166kbps) at a fixed concentration of poly(ethylene glycol) using single-chain observation with fluorescence microscopy. From the van't Hoff-type relationship, the entropy change in the transition is $\Delta S = +11.3k/molecule$, and the change in the heat content is $\Delta H = +4.77 \times 10^{-20} J/molecule$ at $T_c = 306K$, where k is the Boltzmann's constant. The positive value of ΔS with the unfolding transition is discussed in relation to the increase in the translational entropy of counterions.

Introduction

It is well known that giant DNAs generally exist in a highly compact state in living cells. For example, in *E-coli* a DNA molecule with a contour length of $1.4mm$ is packed into a narrow cytoplasmic space on the order of μm. In viruses, giant poly-nucleotides are also compacted into a capsid; *e.g.*, T4 phage DNA with a length of $57\mu m$ is packed into a space of less than $1\mu m$. Almost all genetic activities, such as transcription, duplication, repairing, etc., are believed to be closely related to the conformation of the DNA molecule. In order to investigate the compaction or packing of giant DNAs in living cells under very complex conditions in the presence of thousands of different chemical species, *in vitro* experiments on DNA condensation are useful for understanding the mechanism of DNA compaction. It has been found that a neutral hydrophobic polymer such as poly(ethylene glycol) (PEG) induces the condensation of DNA [1]. Such a phenomenon is called polymer salt-induced condensation, or Ψ condensation [2, 3]. Since actual cellular fluid is usually crowded with hydrophilic macromolecules, or proteins [4], the *in vitro* condensation of DNA by PEG is expected especially to serve as a good model for the compaction of DNA in cellular systems. However, despite intensive work on Ψ condensation, most experimental studies on condensation have been performed without clear distinction between the folding of single molecular chains and the aggregation of multiple chains [5, 6, 7, 8]. Thus, the term "condensation" has often been applied to events involving multiple DNAs in conventional studies of Ψ condensation.

Very recently, it has been found that individual giant DNA molecules exhibit an all-or-none-type transition between the elongated coil state and compact folded state using single-chain observation with fluorescence microscopy [9, 10, 11]. It has also become clear that the transition in the ensemble of DNA chains seems continuous, indicating that there is a rather wide region for the coexistence of unfolded and folded chains with respect to the change in the concentration of the condensation agent, such as poly(ethylene glycol) or polyvalent cations. The purpose of the present study is to examine the effect of temperature on the switching of the higher order structure of giant DNAs. By adding a temperature-controlling unit to the system for single-chain observation by fluorescence microscopy, we have measured the change in the size distribution (long-axis length) of DNA as a function of temperature. Based on these experimental data, we discuss the thermodynamics in the folding phase- transition on individual DNA molecules.

Experimental

Bacteriophage T4 dc DNA (166 kbps) was purchased from SIGMA. The fluorescent dye 4′ 6-diamidino-2-phenylindole (DAPI) and the antioxidant 2-mercapto-ethanol (2-ME) were obtained from Wako Pure Chemical. Poly(ethylene glycol) (PEG, average MW. 4600) was obtained from Aldrich. The sample solutions were prepared as follows. First, PEG was dissolved in distilled water ($\sim 55°C$). Next, the PEG solution was adjusted so as to contain the following chemicals; PEG, $100(mg/ml)$; 2-ME, $2\ \%(v/v)$; DAPI, 0.6 (μM) ; and DNA in nucleotides, 0.6 μM, where these concentrations were fixed throughout the experiments. The prepared samples were allowed to stand at ambient temperature $23 \pm 2°C$ for 30 min before the observation.

Fluorescence images of DNA were obtained with a Carl Zeiss Axiovert135TV microscope equipped with a 100 × oil-immersed objective lens. They were recorded on videotape with a high-sensitivity

Hamamatsu SIT TV camera and analyzed with an Argus 50 image processor (Hamamatsu Photonics). The temperature of the samples was controlled by a water-circulating system. The accuracy of the temperature was $\pm 0.5°C$. To characterize the size of DNA, we measured the long-axis length L, which was defined as the longest distance in the outline of the DNA image. In the analysis, we only counted the moving DNAs in the bulk solution and omitted the DNAs adsorbed on the glass surface. Due to the high sensitivity of the SIT camera and the resolution limit associated with the wavelength of the observation light, there is a blurring effect of about 0.3 μm [12, 13].

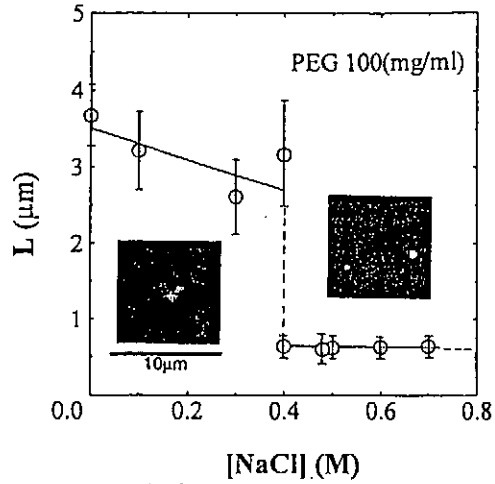

Fig.1: Long-axis length L of individual T4DNA chains vs. the sodium chloride concentration $[NaCl]$. The ensemble average was obtained at least 50 molecules at each concentration. L changes in a discontinuous manner at $[NaCl] = 0.4M$. Typical fluorescence images of the elongated coil and folded compact states are shown.

Results and Discussion

To examine the effect of the temperature on the all-or-none-type transition of individual DNA chains, we tried to find a suitable experimental condition for the folding transition of DNA. Figure 1 shows the dependence of the long-axis length L of individual DNA chains on the sodium chloride concentration $[NaCl]$ at a fixed concentration of poly(ethylene glycol) $(100mg/ml)$ at $23°C$, together with the statistical errors. It is shown that the addition of $NaCl$ promotes the folding transition of DNA chains [12]. This observed effect of salt corresponds well to the results in previous studies on DNA condensation [7, 14], although the previous studies do not seem to have distinguished the folding transition of single DNA molecules from the aggregation, or condensation, of multiple DNA molecules. At least 50 chains were measured at each $NaCl$ concentration. Figure 1 indicates that the value of L changes in a discontinuous manner at $[NaCl] = 0.4M$ and that the unfolding and folding states coexist there. Thus, at around this sodium chloride concentration the folding transition proceeds in an all-or-none manner at the level of individual DNAs.

Based on our results regarding the effect of salt as shown in Fig. 1, we chose a concentration of $[NaCl] = 0.4M$ for the sample solution to examine the effect of temperature. Figure 2 shows the distribution of the long-axis length at different temperatures, and clearly presents a bimodal profile. The portion corresponding to the unfolded coil state tends to increase with an increase in temperature. By evaluating the relative populations of the folded and unfolded states, we can estimate the free energy difference ΔG between the elongated and folded states: $\Delta G/kT = -lnP_f/P_u$, where P_f and P_u are the probabilities of the folded compact and unfolded coil states, respectively. Figure 3 shows that $ln(P_f/P_u)$ changes linearly with $1/T$. From this figure, the temperature at $P_f = P_u$ is $306K$; i.e., the critical temperature in the first-

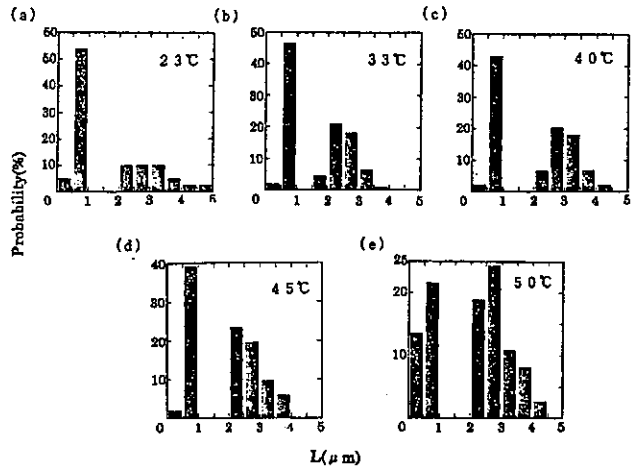

Fig.2: Distribution of the long-axis length L of T4DNA molecules at different temperatures. The temperature is $23°C$ (a), $33°C$ (b), $40°C$ (c), $45°C$ (d) and $50°C$ (e). The left and right peaks in each graph correspond to the folded and unfolded coil states, respectively. With an increase in temperature, the probability of the unfolded coil state increases while that of the folded state decreases.

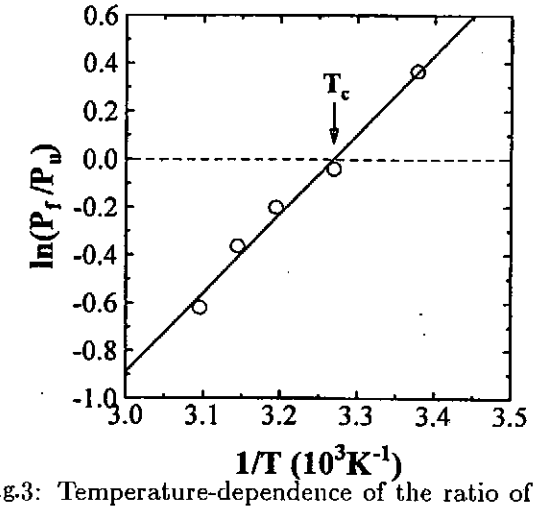

Fig.3: Temperature-dependence of the ratio of the probability of the folded and unfolded states as shown by a $ln(P_f/P_u)$ vs. L plot. From the slope of this linear relationship and the temperature at $P_f = P_u$, the thermodynamic parameters ΔS and ΔH can be estimated to be $+11.3k$ and $+4.77 \times 10^{-20} J/molecule (28.7kJ/mol)$ at $306K$.

order phase transition is $T_c = 306K$. From the slope, ΔS is calculated to be $+11.3k$ per DNA molecule. The heat content of the transition at T_c is $\Delta H = +4.77 \times 10^{-20} J/molecule$ (28.7kJ/mol).

Here, we will discuss briefly the mechanism of the transition. Ψ condensation has been interpreted in the following theoretical framework [2, 3]: Contact between DNA and PEG is considered to be thermodynamically unfavorable, due to the large difference in persistent length between them. Thus, the effective volume of a PEG molecule serves to decrease the free space in unfolded DNAs, but not that of other coiled PEG molecules. As a result, the solvent quality for DNA becomes poorer upon the addition of PEG, and there is effective attraction between the components of a DNA chain. At some critical concentration of PEG, DNAs undergo a collapsing transition or coil-globule transition. Unfortunately, previous studies have considered, at least implicitly, that the coil-globule transition is steep but continuous, or a kind of second-order phase transition [15, 16]. Furthermore, most previous theoretical studies have been devoted to models that do not consider counterions.

Recently, we described a theoretical model to interpret the intrinsic property of the folding transition of single DNA molecules, including the effects of counterions and coexisting low-molecular-weight salt ions [12]. Within this theoretical model, we analyzed the free energy of a DNA chain distributed in PEG solution under the folding framework. The free energy of a single DNA chain, F, can be approximated as follows [12, 17, 18],

$$F = F_{mix} + F_{ela} + F_{tra} \qquad (1)$$

where F_{mix}, F_{ela} and F_{tra} are the free energies from the mixing of DNA and linear polymer, the elastic contribution of DNA chain and the translational entropy of small ions in the system (counterions

and salt ions), respectively. Skipping a detailed explanation of these individual contributions to the free energy, it has become clear that the change in translational entropy before and after the folding transition plays a significant role in determining the free energy. The translational entropy of small ions S_{tra} is represented as follows,

$$S_{tra} = [\sum_i N_i ln \frac{V}{N_i}]_{in} + [\sum_i N_i ln \frac{\Omega}{N_i}]_{out} \qquad (2)$$

where N_i is the number of ion (charge i), V the effective volume of DNA and Ω the volume outside DNA. Figure 4 shows a schematic representation of the distribution of small ions around a single DNA chain in the environment containing PEG molecules. It has been confirmed that the change in the effective volume in the folding/unfolding transition is very large; $V_u/V_f \approx 10^4 \sim 10^5$ [13], where V_u and V_f are the effective volumes in the unfolded and folded states, respectively. Thus, one can expect a significant increase in S_{tra} upon transition from the compact to the elongated state. Using a known value of V_u/V_f [13], Eq. (2) gives the increase in entropy in the unfolding transition of a single T4DNA molecule; $\Delta S_{tra} = +10^5 k \sim 10^6 k$. This estimated entropy difference ΔS_{tra} is much larger than the experimental value of $\Delta S \sim +11.3k$, although both values are positive. This difference is attributable to the so-called hydration effect [19, 20]. It has been well established that small ions interact rather strongly with water molecules. Thus, the increase in the translational entropy of small ions upon dissociation is almost compensated for by the decrease in entropy accompanied by their "complexation" with water molecules [19], and the residual small entropy change corresponds to the observed change of entropy in the experiment. Interestingly, temperature effect on the folding/unfolding transition of DNAs by a multivalent cation is opposite to that by PEG. We recently examined the effect of temperature on the folding transition of T4DNA in the presence of a fixed amount of spermidine, a trivalent amine [21]. We found that unfolded DNA molecules tended to be folded into a compact state with an increase in temperature. According to van't Hoff relationship, the decrease in entropy from the folded to the unfolded state has been evaluated as $\Delta S = -32k$ [21]. Such a temperature dependence is attributed to the increase of the total translational entropy due to the ion-exchange accompanied by the folding transition in relation to the ion-exchange between mono- and trivalent cations. Further experiments on the change in the conformation of individual DNAs at different $NaCl$ concentrations and also with different monovalent cations such as Li^+, K^+, and Rb^+ should provide useful information for estimating the contribution of hydration to the change in entropy.

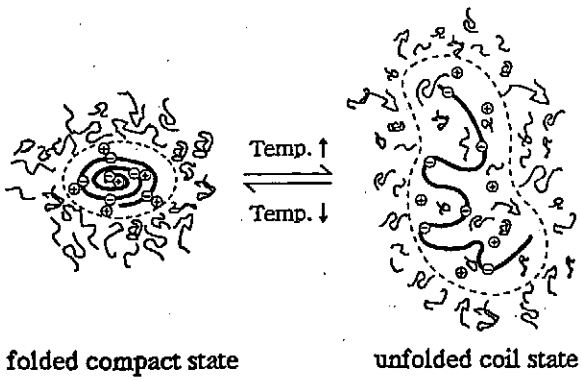

Fig.4: Schematic representation of the distribution of small ions around a DNA chain in the unfolding/folding transition driven by a change in temperature in a PEG solution.

Conclusion

We observed the unfolding transition of single DNA molecules in poly(ethylene glycol) solution. Based on the temperature-dependence of the relative probability of the elongated and compact folded states, T_c, the changes in entropy ΔS and enthalpy ΔH at $306K$ are estimated to be $+11.3(k/molecule)$ and $+4.77 \times 10^{-20}(J/molecule)$, respectively. The sign of the entropy change is opposite that in the unfolding transition of DNA in the presence of multivalent cation. This characteristic effect of temperature in the transition is attributable to the change in the translational entropy of the counterions.

Acknowledgement

This research was done in cooperation with Yoshikawa Laboratory.

References

[1] L. S. Lerman, Proc. Natl. Acad. Sci. USA 68 (1971)1886.

[2] C. B. Post, B. H. Zimm, Biopolymers 18 (1979)1487.

[3] A. Yu. Grosberg, I. Ya. Erukhimovitch, E. I. Shakhnovitch, Biopolymers 21 (1982) 2413.

[4] A. P. Minton, Biophys. J. 68 (1995) 1311.

[5] U. K. Laemmli, Proc. Natl. Acad. Sci. USA 72(1975) 4288.

[6] E. P. Geiduschek, I. Gray, J. Am. Chem. Soc. 78 (1956) 879.

[7] Y. M. Evdokimov, T. L. Pyatigorskaya, O. F. Polyvtsev, N. M. Akimenko, V. A. Kadykov, D. Y. Tsvankin, Y. M. Varshacsky, Nucleic Acids Res. 3 (1976) 2353.

[8] G. Swislow, S. -T. Sun, I. Nishio, T. Tanaka, Phys. Rev. Lett. 44 (1980) 796.

[9] K. Yoshikawa, S. Kidoaki, M. Takahashi, V. V. Vasilevskaya, A. R. Khokhlov, Ber. Bunsenges. Phys. Chem. 100 (1996) 876.

[10] K. Yoshikawa, Y. Matsuzawa, J. Am. Chem. Soc. 118 (1996) 929.

[11] M. Ueda, K. Yoshikawa, Phys. Rev. Lett. 77 (1996) 2133.

[12] V. V. Vasilevskaya, A. R. Khokhlov, Y. Matsuzawa, K. Yoshikawa, J. Chem. Phys. 102 (1995) 6595.

[13] Y. Yamasaki, K. Yoshikawa, J. Am. Chem. Soc. 119 (1997) 10573.

[14] Yu. M. Evdokimov, S. G. Skkuridin, A. T. Dembo, E. V. Shtykoya, V. A. Kadykov, Ya. M. Varshavskii, Mol. Biol.(USSR) 14 (1980) 1378.

[15] I. M. Lifshitz, A. Yu. Grosberg, A. R. Khokhlov, Rev. Mod. Phys. 50(1978) 683.

[16] A. Yu. Grosberg, A. R. Khokhlov, Statistical Physics of Macromolecules, American Institute of Physics, New York, 1994.

[17] V. V. Vasilevskaya, A. R. Khokhlov, Macromolecules 25 (1992) 384.

[18] A. R. Khokhlov, S. G. Starodubtzev, V. V. Vasilevskaya, Adv. Polym. Sci. 109 (1993) 123.

[19] D. C. Rau, V. A. Parsegian, Biophys. J. 61 (1992) 260.

[20] D. C. Rau, V. A. Parsegian, Biophys. J. 61 (1992) 246 .

[21] H. Murayama, K. Yoshikawa, submitted for publication.

Spiral Structures in Magnetized Rotating Plasmas

Masayoshi Y. Tanaka and Mitsuo Kono*
National Institute for Fusion Sciences, Toki, Gifu 509-5292, Japan,
* Faculty of Policy Studies, Chuo University, Hachioji,
Tokyo 192-0393, Japan

Abstract

Evolution of low frequency perturbations in magnetized rotating plasma is formulated, and the eigen-value problem for the perturbed potential is numerically solved to show the existence of spiral solutions. Remarkable characteristic of this solution is that the eigen-value (frequency) becomes zero for particular case. Formation of stationary spiral structure, which was experimentally observed in an ECR plasma, is theoretically confirmed.

Recently, two-arms spirals have been commonly observed in both ECR plasmas [4] and gun-produced plasmas [5], and in particular the spiral structures observed in the ECR plasmas have interesting features: (1) stationary spiral structure is observed in a certain range of the background pressure, (2) the direction of the arm stretching is reversed when the magnetic field is reversed, and (3) the arm winding is identified as an Archimedes spiral.

In an ECR plasma with cylindrical geometry, there is radial electric field of the order of T_e/r_d (T_e: electron temperature, r_d: plasma radius), and the plasma rotates azimuthally with the $\mathbf{E} \times \mathbf{B}$ drift. The ion-neutral collision is small compared with the ion cyclotron frequency ($\nu_i/\Omega_i \sim 0.05$), but not negligible. In this circumstance, the primary motion of the plasma is azimuthal rotation due to the $\mathbf{E} \times \mathbf{B}$ drift. Then we consider evolution of low frequency perturbations in a rotating magnetized plasma.

In this paper, we show that low frequency instability in an azimuthally rotating plasma may develop into spiral structures, which, in particular case, are stationary. Low frequency instabilities such as collisional drift wave instability, centrifugal instability and Kelvin-Helmholz instability are taken into account, and the linear eigen-value problem for the perturbed potential is numerically solved to show the existence of spiral solutions.

Plasmas in a cylindrical vessel are inevitably driven to rotate with the $\mathbf{E}\times\mathbf{B}$ drift due to the ambipolar potential. Then the ions are subjected to centrifugal force and their

rotation frequency is affected by this effective gravitational force, while the electrons are driven by both the $\mathbf{E} \times \mathbf{B}$ drift and the diamagnetic drift. The difference between the azimuthal drift velocities of the ions and electrons induce charge separation which cannot be fully neutralized by the electrons whose axial motions are dragged by the collisions with neutral particles. Thus fluctuations are excited and azimuthal motions are organized in such a way that the core part of the plasmas is rotating almost rigidly, while the outer part lags behind the core part because the azimuthal drift velocities do not increase in proportion to the radius, consequently producing a spiral structure.

Equations for ions and electrons in magnetized plasmas read

$$\frac{\partial n_\alpha}{\partial t} + \nabla(n_\alpha \mathbf{v}_\alpha) = 0, \tag{1}$$

$$\frac{\partial \mathbf{v}_\alpha}{\partial t} + \mathbf{v}_\alpha \cdot \nabla \mathbf{v}_\alpha = \frac{e_\alpha}{m_\alpha}(-\nabla\phi + \frac{1}{c}\mathbf{v}_\alpha \times \mathbf{B}) - \delta_{\alpha,e}\frac{1}{nm_\alpha}\nabla p_\alpha - \nu_\alpha \mathbf{v}_\alpha. \tag{2}$$

where n_α, $\mathbf{v}_\alpha$ and ν_α ($\alpha = e$ or i) are the density, velocity and collision frequency with neutral particles of electrons and ions, respectively, and ϕ is the plasma potential.

In the following, physical quantities are divided into the stationary parts and fluctuating parts:

$$\begin{pmatrix} n \\ \phi \\ \mathbf{v} \end{pmatrix} = \begin{pmatrix} n_0(r,z) \\ \phi_0(r,z) \\ \mathbf{v}_0(r,z) \end{pmatrix} + \sum_\ell \begin{pmatrix} n_\ell(r,z) \\ \phi_\ell(r,z) \\ \mathbf{v}_\ell(r,z) \end{pmatrix} e^{i(\ell\theta - \omega t)} + c.c.$$

For the ion drift, an effective gravitational drift due to the centrifugal force is taken into account in the azimuthal direction, and is neglected in the radial direction since $\nu_i/\Omega_i << 1$. For the electron drift, the diamagnetic drift is dominated over the gravitational drift due to the centrifugal force. The rotation frequencies of the ion and electron azimuthal drift now read

$$\omega_0^i \simeq \omega_E(1 - \frac{\omega_E}{\Omega_i}), \quad \omega_0^e \simeq \omega_E + \omega_*, \tag{3}$$

where ω_E and ω_* are the frequencies associated with the $\mathbf{E}\times\mathbf{B}$ drift and the diamagnetic drift, respectively, defined by

$$\omega_E = \frac{C_s^2}{\Omega_i}\frac{1}{r}\frac{d\phi_0}{dr}, \quad \omega_* = -\frac{v_T^2}{\Omega_e}\frac{1}{r}\frac{d\ln n_0}{dr}, \tag{4}$$

where $C_s^2 = T_e/M$, $v_T^2 = T_e/m$, $\Omega_i = eB/Mc$ and $\Omega_e = eB/mc$ (M: ion mass, m: electron mass). The normalized potential $e\phi_0/T_e$ has been replaced by ϕ_0 in Eq.(4). The second term in the expression for ω_0^i is a contribution from the centrifugal force.

The space potential produced by the ion radial transport is short-circuited by the electron axial transport so that we have $\nabla(n_0^i \mathbf{v}_0^i) = \nabla(n_0^e \mathbf{v}_0^e)$, which determines the profile of the equilibrium density and potential. Since the solution of this equation is sensitively dependent on the boundary conditions at the end of the field lines unless the plasma is so long that parallel diffusion can be neglected altogether, it is unlikely to obtain a self-consistent solution $n_0(r,z)$ and $\phi_0(r,z)$ to the problem of ambipolar diffusion across magnetic field. Instead, in the following we take a phenomenological approach to assume the density and potential profiles compatible with those observed in the experiment.

The fluctuating parts of electron velocities given by Eqs.(1) and (2) are

$$\begin{aligned}
u_\ell^e &= \frac{v_T^2}{\Sigma_e(\omega)}[-\frac{i\ell(\Omega_e - 2\omega_0^e)}{r} + \Gamma_e(\omega)\frac{\partial}{\partial r}](\phi_\ell - \frac{n_\ell^e}{n_0}), \\
v_\ell^e &= \frac{v_T^2}{\Sigma_e(\omega)}[(\Omega_e - \omega_0^e - \frac{dv_0^e}{dr})\frac{\partial}{\partial r} + \frac{i\ell\Gamma_e(\omega)}{r}](\phi_\ell - \frac{n_\ell^e}{n_0}), \\
w_\ell^e &= \frac{v_T^2}{\Gamma_e(\omega)}\frac{\partial}{\partial z}(\phi_\ell - \frac{n_\ell^e}{n_0}),
\end{aligned}$$

where $u_\ell^e, v_\ell^e, w_\ell^e$ are the radial, azimuthal and axial component of $\mathbf{v}_\ell^e$, respectively, and

$$\begin{aligned}
\Gamma_e(\omega) &= \nu_e - i(\omega - \ell\omega_0^e), \\
\Sigma_e(\omega) &= (\Omega_e - 2\omega_0^e)(\Omega_e - \omega_0^e - \frac{dv_0^e}{dr}) + \Gamma_e(\omega)^2.
\end{aligned}$$

On the other hand the fluctuating parts of ion velocities are given by

$$\begin{aligned}
u_\ell^i &= -\frac{C_s^2}{\Sigma_i(\omega)}[\frac{i\ell(\Omega_i + 2\omega_0^i)}{r}\phi_\ell + \Gamma_i(\omega)\frac{\partial\phi_\ell}{\partial r}], \\
v_\ell^i &= \frac{C_s^2}{\Sigma_i(\omega)}[(\Omega_i + \omega_0^i + \frac{dv_0^i}{dr})\frac{\partial\phi_\ell}{\partial r} - \frac{i\ell\Gamma_i(\omega)}{r}\phi_\ell], \\
w_\ell^i &= -\frac{C_s^2}{\Gamma_i(\omega)}\frac{\partial\phi_\ell}{\partial z},
\end{aligned}$$

where the meanings of $u_\ell^i, v_\ell^i, w_\ell^i$ are the same as for the electron, and

$$\begin{aligned}
\Gamma_i(\omega) &= \nu_i - i(\omega - \ell\omega_0^i), \\
\Sigma_i(\omega) &= (\Omega_i + 2\omega_0^i)(\Omega_i + \omega_0^i + \frac{dv_0^i}{dr}) + \Gamma_i(\omega)^2.
\end{aligned}$$

Substituting the above velocities into the electron and ion continuity equations, invoking charge neutrality $n_\ell^e = n_\ell^i = n_\ell$, and assuming the axial dependence of the potential with the normalizations $\xi = r/r_d$ and $\eta = z/r_d$ as

$$\phi_\ell(\xi,\eta) = \phi_\ell(\xi)e^{-(\kappa - ik)\eta}, \tag{5}$$

we have

$$\frac{d^2\phi_\ell}{d\xi^2} + [\frac{1}{\xi} + \frac{d\ln n_0}{d\xi}]\frac{d\phi_\ell}{d\xi} + [\beta(\xi) - \frac{\ell^2}{\xi^2}]\phi_\ell = 0, \tag{6}$$

where the quantity $\beta(\xi)$ is given by

$$\beta(\xi) = \frac{(\kappa - ik)^2\Omega_e\Omega_i}{\Gamma_e(\omega)\Gamma_i(\omega)}(1 - \frac{\ell\omega_*}{\omega - \ell\omega_E}) \tag{7}$$

$$- \frac{i\ell}{\xi}\frac{1}{\Gamma_i(\omega)}\Big[(\omega_0^i + \frac{1}{r_d}\frac{dv_0^i}{d\xi} + \frac{\ell\omega_E^2}{\omega - \ell\omega_E})\frac{d\ln n_0}{d\xi} + \frac{d\omega_0^i}{d\xi} + \frac{1}{r_d}\frac{d^2v_0^i}{d\xi^2}\Big]. \tag{8}$$

In deriving Eq.(6), we have neglected the terms of the order of or less than $O(\Omega_i/\Omega_e)$ and $O(\omega_0^i/\Omega_i)$, and used the following approximation derived from the electron or ion continuity equation,

$$\frac{n_\ell}{n_0} \simeq -\frac{v_T^2}{\Omega_e^2}\frac{\ell\Omega_e}{\omega - \ell(\omega_0^e - \omega_*)}\frac{1}{r}\frac{d\ln n_0}{dr}\phi_\ell = \frac{\ell\omega_*}{\omega - \ell\omega_E}\phi_\ell. \tag{9}$$

Equation (6) describes low frequency fluctuations excited by collisional drift wave instability (the first term of $\beta(\xi)$) [7] and flute mode instability such as the gravitational instability due to centrifugal force acting on ions (the second term of $\beta(\xi)$) [8] and Kelvin-Helmholz instability (the third and fourth terms of $\beta(\xi)$) [9]. The difference between Eq.(6) and the equation derived by Rosenbulth and Simon [6] is that the collisional drag is taken into account and the charge neutrality is assumed in Eq.(6), while in Ref.[6] the collisional drag is not included and the ion diamagnetic drift is taken into account instead of the electron diamagnetic drift. Putting that $\phi_\ell(\xi) = \psi_\ell(\xi)/\sqrt{n_0(\xi)}$, Eq.(6) is transformed to

$$\frac{d^2\psi_\ell}{d\xi^2} + \frac{1}{\xi}\frac{d\psi_\ell}{d\xi} + [A(\xi) - \frac{\ell^2}{\xi^2}]\psi_\ell = 0, \tag{10}$$

where

$$A(\xi) = \beta(\xi) - \frac{1}{4}(\frac{d\ln n_0}{d\xi})^2 - \frac{1}{2}(\frac{d}{d\xi} + \frac{1}{\xi})\frac{d\ln n_0}{d\xi}.$$

The ratio of the contribution from the drift wave to that from the flute mode is estimated to be $(\kappa^2 + k^2)(\Omega_e/\nu_e)(r_d\Omega_i/C_s)$. Therefore the collisional drift wave instability is dominant when $\kappa^2 + k^2 >> (\nu_e/\Omega_e)(C_s/r_d\Omega_i)$ is satisfied. The quantity $(\nu_e/\Omega_e)(C_s/r_d\Omega_i)$ is of the order of 10^{-4} to 10^{-5} for the ECR plasmas and thus we only consider the fluctuations due to the collisional drift wave instability:

$$A(\xi) \simeq \frac{(\kappa - ik)^2\Omega_e\Omega_i}{\Gamma_e(\omega)\Gamma_i(\omega)}\frac{(\omega - \ell\omega_0^e)}{(\omega - \ell\omega_E)}$$

Now the characteristic features of the solutions for Eq.(10) can be examined as follows. The solution is approximated in the case of weak ξ-dependence of the zero-th order quantities by $\psi_\ell(\xi) \simeq J_\ell(\xi\sqrt{A})$, where J_ℓ is the Bessel function of the first

kind. The real part of the argument of the Bessel function should be positive to give a convergent behavior while the imaginary part is responsible for spiral structure, which comes from the imaginary parts of ω, $\Gamma_e(\omega)$ and $\Gamma_i(\omega)$. Multiplying ψ_ℓ^* to Eq.(10) and integrating the resultant equation from the center to the edge of the plasma under the boundary condition $\psi_\ell(0) = \psi_\ell(1) = 0$, we have

$$\int_0^1 \xi\{|\frac{d\psi_\ell}{d\xi}|^2 + \frac{\ell^2}{\xi^2}|\psi_\ell|^2 - A(\xi)|\psi_\ell|^2\}d\xi = 0. \tag{11}$$

From the imaginary part of this equation we have

$$\int \Im[A(\xi)]\xi|\psi_\ell(\xi)|^2 d\xi = 0, \tag{12}$$

which corresponds to the Rayleigh condition. For a collisional drift mode, we have at the marginal instability ($\gamma \sim 0$) with $\kappa >> k$

$$\Im[A(\xi)] = \frac{\nu_e \kappa^2 \Omega_e \Omega_i (\omega_r - \ell\omega_0^e)(\omega_r - \ell\omega_0^i)(\omega_r - \ell\omega_E)}{|\Gamma_e(\omega)|^2|\Gamma_i(\omega)|^2[(\omega_r - \ell\omega_E)^2 + \gamma^2]},$$

from which the Rayleigh condition holds even when $\omega_r = 0$, indicating the formation of stationary spiral structures. The winding direction of spiral arms is reversed when the magnetic fields is changed in sign since the imaginary part of $A(\xi)$ is proportional to odd power of the magnetic field for $\omega_r = 0$. Certainly rotating spirals exist as well.

Here we solve Eq.(6) numerically with the boundary condition $\psi_\ell(0) = \psi_\ell(1) = 0$. Since, according to the experimental observations, the profile of $\mathbf{E} \times \mathbf{B}$ drift frequency ω_E has one zero between $\xi = 0$ and $\xi = 1$, we have used the ω_E profile as shown in Fig.1 in the calculations. Furthermore, the density profile $n_0(r)$ has been assumed to be Gaussian, from which the diamagnetic drift frequency ω_* is depicted in the same figure. We have both the stationary ($\omega_r = 0$) and rotating ($\omega_r \neq 0$) spiral solutions for a given profile of the zero-th order quantities $n_0(r)$ and $\omega_E(r)$. The numerical results for the stationary solution ($\ell = 2$) are shown in Fig.2, where Fig.2(a) is the radial potential profile, and Fig.2(b) the density perturbation contour calculated by Eq.(9). The spiral structure is identified as an Archimedes spiral, which is seen from the eikonal approximation for the solution of Eq.(6); in the case of weak $\xi-$dependence of $\beta(\xi)$, $\phi_\ell(\xi)\exp[i\ell\theta] \sim \exp[i\int \Im[\sqrt{\beta}]d\xi + i\ell\theta] \sim \exp[i\Im[\sqrt{\beta}]\xi + i\ell\theta]$ and the spiral curves are given by $\xi \propto \theta$. The density contour structure is similar to the observed spiral.

The vector field plot of the ion velocity $\{u_\ell^i, v_\ell^i\}$ associated with this spiral structure is depicted in Fig.3. In the figure, each arrow is colored by red for positive radial velocity $u_\ell^i > 0$ and by green for negative radial velocity $u_\ell^i < 0$. The flow pattern exhibits the similar spiral structure, which well explained by the $\mathbf{E} \times \mathbf{B}$ drift due to the perturbed potential ϕ_ℓ. It should be noted that the spiral structure induces both the

outward-going (anticlockwise) flow and the inward-going (clockwise) flow, exhibiting a material circulation between the core and peripheral regions.

The imaginary part of the eigenvalue γ decreases with the azimuthal mode number ℓ, which corresponds to the fact that the observed stationary spirals are always with two arms.

The mass ratio of ion and electron is taken to be 80000 in the above calculations since the experiments were curried out in an argon plasma. The spiral solutions are independent on the mass ratio and also obtained for the hydrogen case ($M/m = 2000$).

Even when we neglect the contributions from the centrifugal and the Kelvin-Helmholz instabilities in Eq.(6), there is no change in the pattern of the spiral. Thus, the spiral structure formation for this choice of parameters is attributable to the collisional drift wave instability.

In the numerical calculations, we have used the special profile for the $n_0(r)$ and $\omega_E(r)$ since we need to compare the numerically obtained spirals with those observed in the experiment [4]. However, it has been confirmed that the spiral solutions of Eq.(6) are insensitive to the profiles of these quantities.

For the different parameters, granulated density structures are obtained, which is regarded as a formation of vortex crystal. Although the vortex crystallization has been reported in pure electron plasmas [2], this type of structures may be general entities excited in magnetized plasmas.

Formation of spiral structures is a rather general characteristic of magnetized rotating plasmas since the energy stored in the plasma inhomogeneity such as density and velocity shear is released to give instabilities, which cause the phase difference between the real and imaginary parts of eigen-functions, driving a spiral structure. The instabilities could be the collisional drift wave instability, centrifugal instability, and Kelvin-Helmholz instability, although the collisional drift wave instability is dominant for ordinary laboratory plasmas. Even in stable cases, collision plays the same role as instabilities in producing phase difference between the real and imaginary parts of the eigen-function. Therefore collision is also essential to the formation of spiral structure. Under the special condition that $\omega_E(\xi)$ becomes zero somewhere between $\xi = 0$ and $\xi = 1$, the characteristic of the stationary spiral structure becomes similar to those observed in the experiment. For a wide variety of density and potential profiles, rotating spiral structures are normally excited.

We have obtained the linear eigen-functions to show the spiral structure formations in magnetized rotating plasmas. The next step is to study the nonlinear stage of evolution and to show why spiral structures are so robust. We are also planning to develop our theory to understand the spiral structures observed in a gun-produced plasma [5]. It is worth noting that our study may contribute for understanding the

mechanism of spiral galaxy formation.

References

[1] M.V. Nezlin and E.N. Snezhkin, *Rossby Vortices, Spiral Structures, Solitons*, (Springer-Verlag, Berlin, 1993).

[2] K.S. Fine, A.C. Case, W.G. Flynn and C.F. Driscoll, Phys. Rev. Lett. **75**, 3277 (1995).

[3] Y. Amagishi, Y. Yoshikawa and J. Ohara, J. Phys. Soc. Jpn **60**, 2496 (1992).

[4] M.Y. Tanaka, T. Sakamoto, H. Imaizumi, K. Taniguchi and Y. Kawai, Proc. 1996 Int. Conf. on Plasma Physics (Nagoya, Japan) Vol.2, 1650 (1997).

[5] T. Ikehata, H. Tanaka, N.Y. Sato and H. Mase, Phys. Rev. Lett. **81**, 1853 (1998).

[6] M.N. Rosenbulth and A. Simon, Phys. Fluids **8** 1300 (1965).

[7] F.F. Chen, Phys. Fluids **10**, 1647 (1967).

[8] A.B. Mikhailovskii, *Theory of Plasma Instabilities, vol.2* Chap.7, (Consultants Bureau, New York, 1974).

[9] C.C. Lin, *The Theory of Hydrodynamic Stability*, (Cambridge University Press, Cambridge, 1966).

Figure 1: The radial profiles of the normalized $\mathbf{E} \times \mathbf{B}$ drift frequency ω_E/Ω_i and the normalized diamagnetic drift frequency ω_*/Ω_i.

Figure 2: The numerical results for a stationary spiral solution ($M/m = 80000$, $\kappa = 0.0675$, $k = 0.0225$, $\gamma/\Omega = 0.024$). (a): the radial profile of the perturbed potential $\phi_\ell(\xi)$, in which the solid line is the real part, and the dotted line the imaginary part. (b): the density perturbation contour $\Re[(n_\ell/n_0)\exp(i\ell\theta)]$.

Figure 3: The vector field plot of ion velocity associated with the spiral structure corresponding to Fig.2 ($u_\ell^i > 0$: black; $u_\ell^i < 0$: gray).

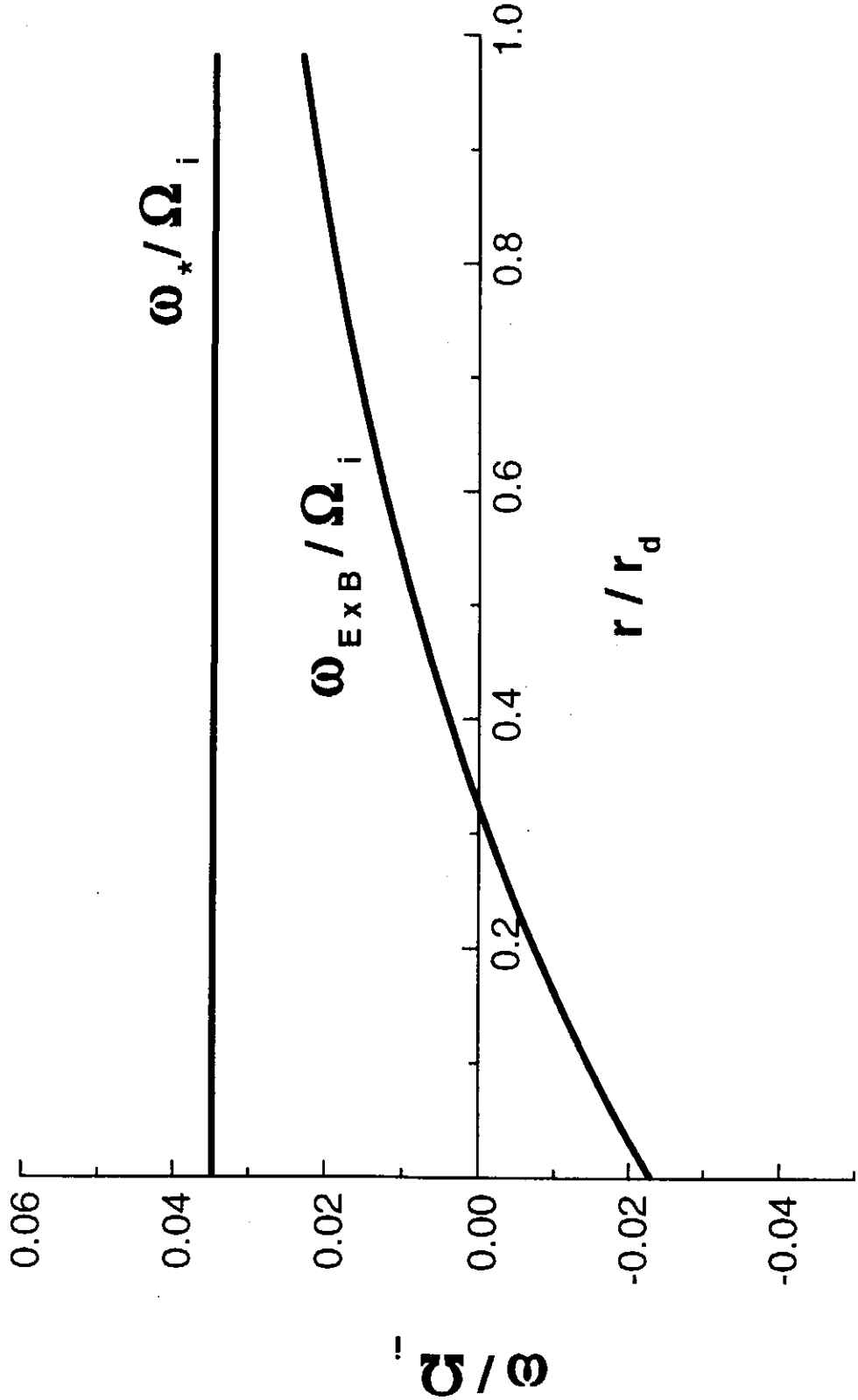

Fig. 1

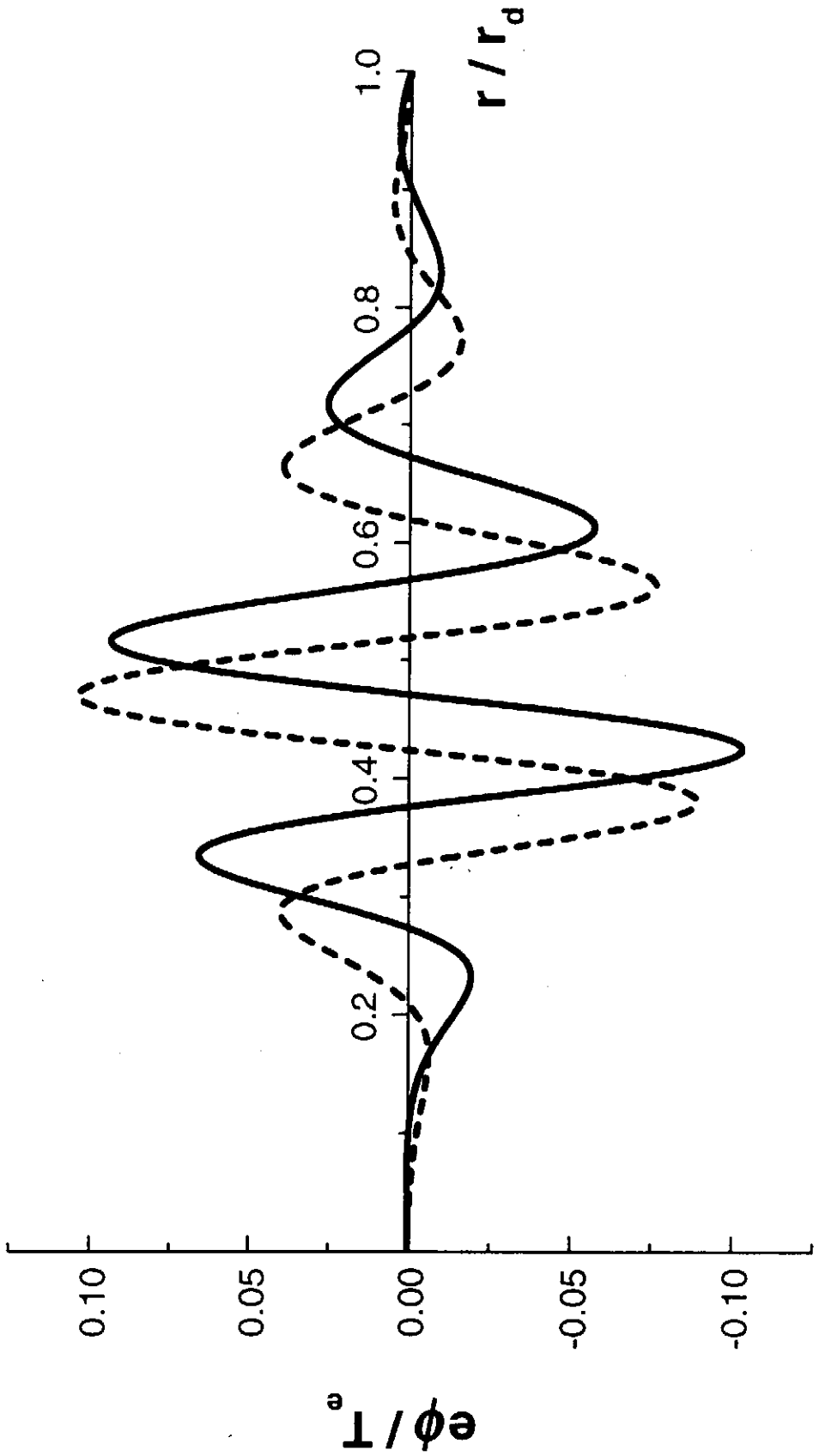

Fig. 2(a)

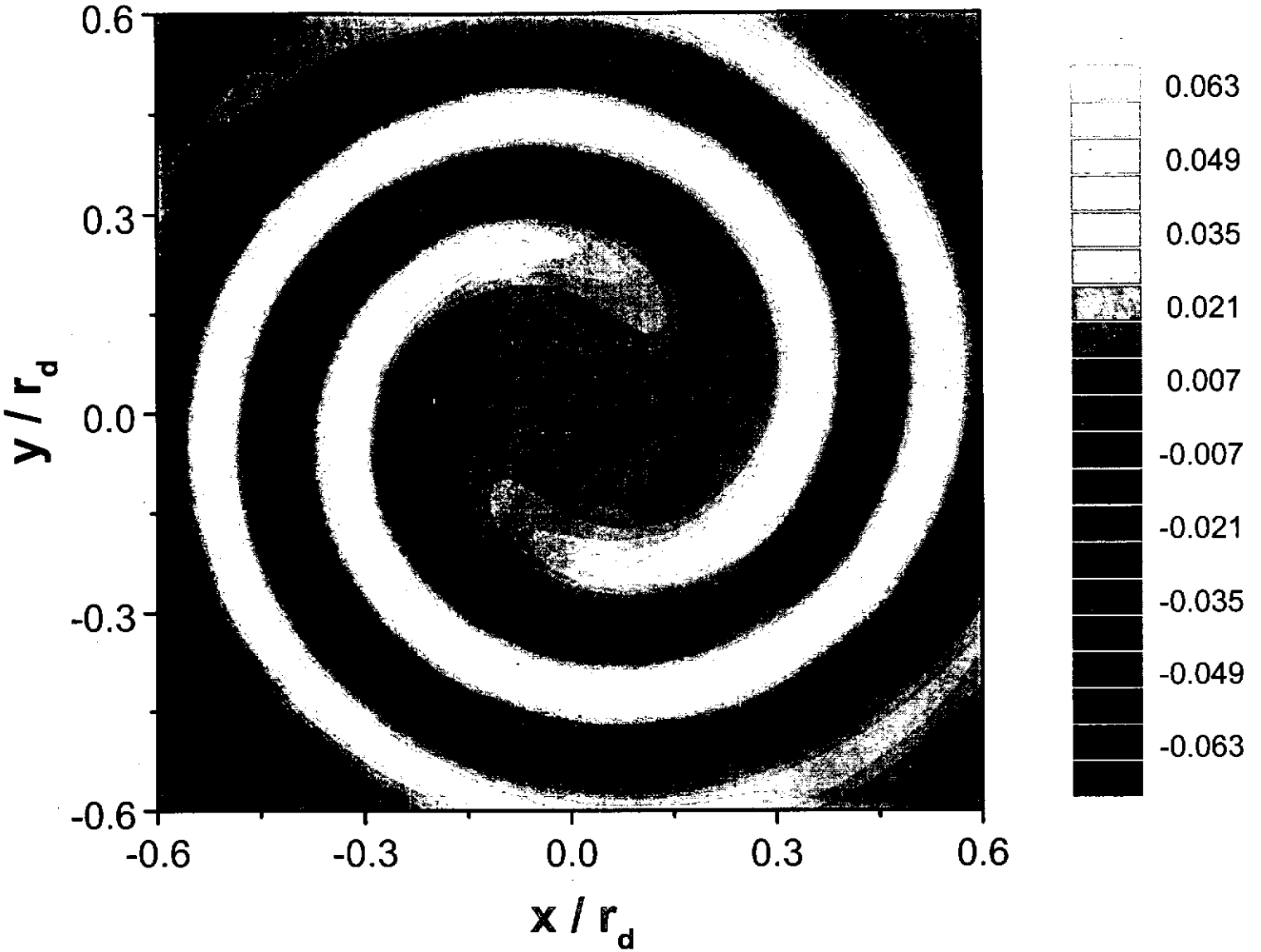
0.6
0.3
0.0
-0.3
-0.6
y / r_d
-0.6
-0.3
0.0
0.3
0.6
x / r_d
0.063
0.049
0.035
0.021
0.007
-0.007
-0.021
-0.035
-0.049
-0.063

Fig. 2(b)

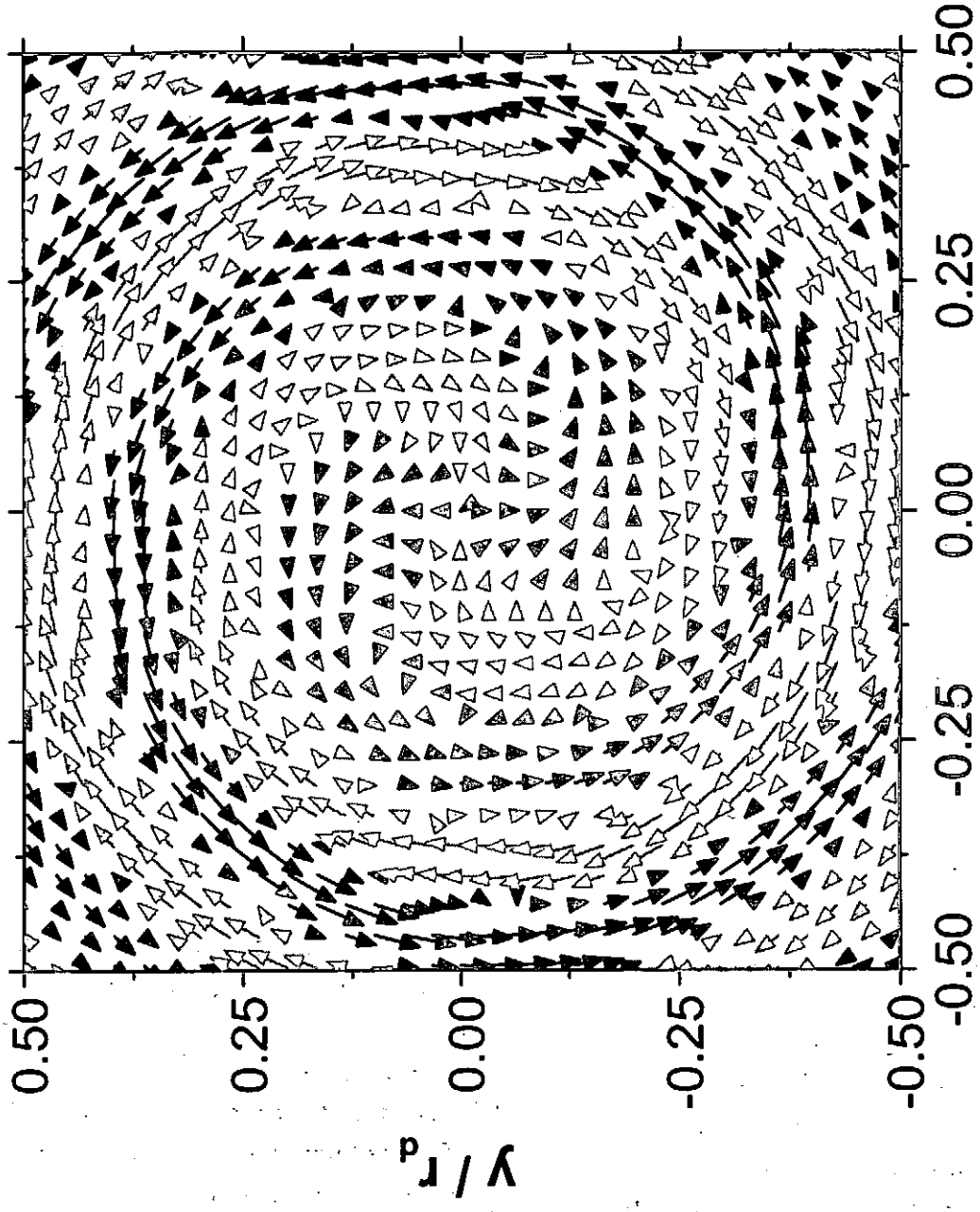

Fig. 3

Two-Dimensional Strongly Coupled Plasma Experiments using Charged Balls System

T. Shoji, K. Shinohe, Y. Sakawa

Department of Energy Engineering and Science, Nagoya University, Nagoya 464-8603, Japan

1. Introduction

When the dimensionless coupling constant of a plasma, $\Gamma=(q^2/4\pi d)/k_BT$, is larger than unity, a long range Coulomb interaction plays a dominant role on the collective phenomena and such a plasma is called a strongly coupled plasma (SCP), where T, q and d are temperature ,charge and inter-particle distance of the plasma, respectively. Several experiments have been conducted to study SCP in the laboratory by increasing charges of small particles in a liquid [1], air [2] and in a low density plasma [3-4]. We demonstrate a simple system of two dimensional (2-D) SCP, where Γ is easily controlled by external parameters.

2. 2-D charged ball system

Experimental setup is shown in Fig.1. Small stainless steal balls (1mm ϕ) are placed on the Si wafer to minimize the friction between the balls and the surface. The balls are charged up by applying DC high voltage V ($\leq$ 50kV) refer to the mesh electrode above. The charged balls are confined by the potential of the metal ring of 90mm in diameter, which is placed on the Si wafer. The charge q can be easily controlled and measure from the critical voltages V_C, where the electric and gravitational forces exerting on the balls balance each other.

The random kinetic energy of the balls is given through random oscillations of the wafer caused by the sound pressure from the speaker placed underneath the wafer.

3. Solidification of 2-D plasma

The statistics of the ball velocities are analyzed from the ball motions taken by a video camera through the mesh. The effective temperature of balls is measured by fitting the velocity distribution of the balls to 2-D Maxwellian one. We include the rotation energy of the balls and the image charge on the wafer induced by the charge on the balls to calculate Γ. The trajectories of the balls in 2 seconds with different Γ values are shown in Fig. 3(b). When Γ=95, the solidification starts to be seen and stable crystallization appears (Fig. 3(a)). The peaking of the radial distribution functions of the balls also indicate the crystalline alignment near Γ=95. The freezing transition of SCP to the triangle Wigner crystal is predicted at Γ~137 by the computer simulation [5], which is near to the experimental result.

4. Diffusion in SCP

The mean square displacement of N balls, $\langle R^2(t)\rangle$, can be written as

$$\left\langle R^2(t)\right\rangle=\left\langle \frac{1}{N}\sum_{i=1}^{N}|r_i(t)-r_i(0)|^2\right\rangle$$

, where $r_i(t)$ and $r_i(0)$ are distances of ith ball from the origin anywhere in the system at time t and 0. It is observed that the balls diffuse proportional to time when Γ is small and $\langle R^2(t)\rangle$ tend to be constant around Γ ~95 (Fig.4). A diffusion coefficient D can be defined in the limit when t goes infinity as

$$\left\langle R^2(t)\right\rangle=4Dt+\alpha \quad (t\rightarrow\infty)$$

, where α is some constant value.

D is plotted versus Γ in Fig. 5 and the abrupt decrease in D is obtained Γ~100 where the crystallization is predicted

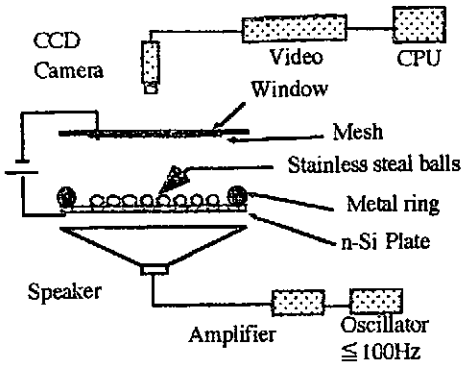

Fig.1: 2-D Charged ball system

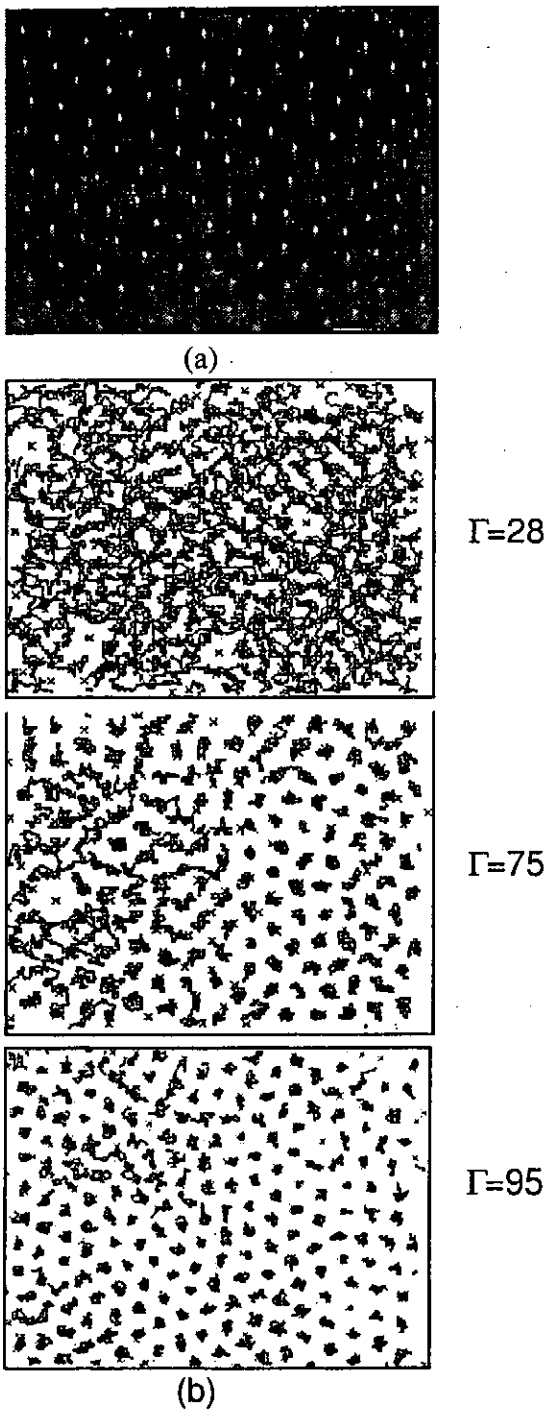

Fig. 2 (a) Crystallized charged metal balls on Si wafer (b)Trajectories of the balls in 2 seconds with different Γ values

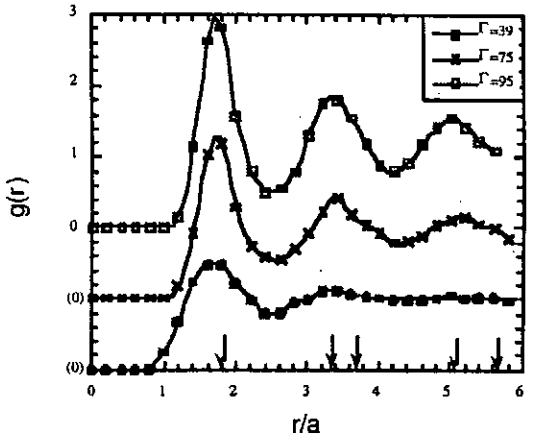

Fig. 3: Radial distribution function for Γ=39, 75, and 95. Arrows indicate the peaks for Wigner cristal.

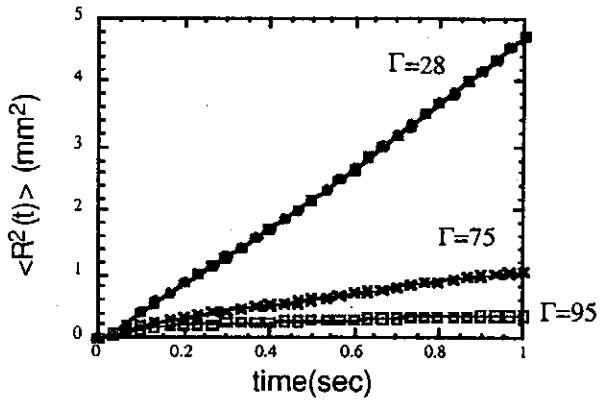

Fig. 4: Time evolution of mean square displacement $<R(t)^2>$ for different Γ.

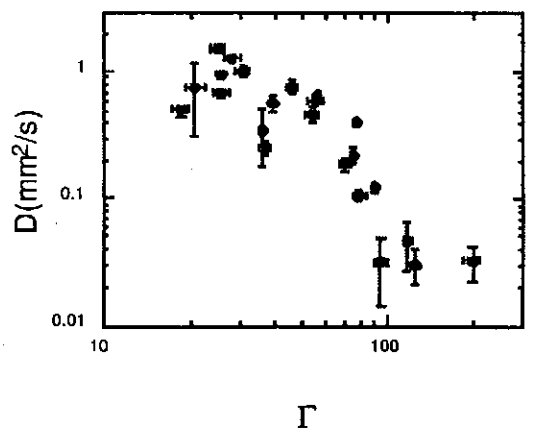

Fig. 5 Diffusion coefficient versus Γ

References

[1] S. Sakaki, J. Chem. Phys. 82(1985)996

[2] R. Wuerker, H. Shelton, and R. Langmuir, J. Appl.Phys. 30(1959)342

[3] J. Chu et al., J Phys. D27(1994)296

[4] Y. Hayashi and K. Tachibana, Jpn. J. Appl. Phys. 33(1994)804

[5] S. Brush, H. Salin and, E. Teller, J. Chem. Phys. 45(1966)2102

An Equilibrium Equation of a Magnetized Plasma Including Electric Fields

Koichi Saeki and Akira Tsushima†

Department of Physics, Faculty of Science, Shizuoka University, Ohya 836, Shizuoka 422,

†*Department of Physics, Faculty of Science, Yokohama National University, Tokiwadai 156, Hodogaya-ku, Yokohama 240*

1. Introduction

The equilibrium of a Tokamak plasma is sustained by a toroidal current and described by the Grad-Shafranov equation [1]. On the other hand, Stix [2] proposed the plasma confinement by a magnetoelectric torus where the poloidal plasma rotation reduces the charge accumulation. Here, in case of neglecting the convective derivative term, we derive an equilibrium equation of a magnetized plasma including electric fields, which gives the description from the Tokamak to the magnetoelectric torus, continuously.

2. An Equilibrium Equation

In order to get an equilibrium equation, we work from MHD equations. The momentum balance equation of a steady state is

$$nm(\boldsymbol{v}\cdot\nabla)\boldsymbol{v} = \boldsymbol{j}\times\boldsymbol{B} - \nabla p - \rho_c\nabla\phi. \tag{1}$$

Here, $\boldsymbol{v}$ is the fluid velocity. n, m and p are the plasma density, the ion mass and the plasma pressure. $\boldsymbol{j}$ and $\boldsymbol{B}$ are the electric current density and the magnetic field. ρ_c and ϕ are the electric charge density and the plasma potential, respectively. Ohm's law in case of zero resistivity is

$$-\nabla\phi + \boldsymbol{v}\times\boldsymbol{B} = \frac{1}{en}(\boldsymbol{j}\times\boldsymbol{B} - \frac{T_e}{T_e+\gamma T_i}\nabla p). \tag{2}$$

Here, T_e and T_i are the electron and ion temperatures. γ is the specific-heat ratio of ions.

We treat an axisymmetric plasma by using the cylindrical coordinates r, θ, z. The poloidal magnetic flux function ψ and the poloidal current flux function I are defined by

$$\boldsymbol{B} = \frac{1}{2\pi r}(\nabla\psi\times\hat{\boldsymbol{\theta}} + \mu_0 I\,\hat{\boldsymbol{\theta}}), \tag{3}$$

$$\boldsymbol{j} = \frac{1}{2\pi r}(\nabla I \times \hat{\boldsymbol{\theta}} - \frac{1}{\mu_0}\mathcal{L}\psi\,\hat{\boldsymbol{\theta}}), \tag{4}$$

respectively. Here, $\mathcal{L}\psi = r\partial/\partial r(\partial\psi/r\partial r) + \partial^2\psi/\partial z^2$. $\hat{\boldsymbol{\theta}}$ is the unit vector in the azimuthal direction. The electric charge density ρ_c is determined by Poisson's equation $\epsilon_0\nabla^2\phi = -\rho_c$. ϵ_0 is the dielectric constant of vacuum.

By taking the scalar product of Eq. (1) and $\nabla\psi/|\nabla\psi|^2$, the generalized Grad-Shafranov equation is derived as

$$\frac{1}{(2\pi r)^2}\left[\frac{\mathcal{L}\psi}{\mu_0} + \mu_0 I\frac{\nabla I\cdot\nabla\psi}{|\nabla\psi|^2}\right] + \left[\nabla p - (\epsilon_0\nabla^2\phi)\nabla\phi + nm(\boldsymbol{v}\cdot\nabla)\boldsymbol{v}\right]\cdot\frac{\nabla\psi}{|\nabla\psi|^2} = 0. \tag{5}$$

The magnetic, current, equipotential and isobaric surfaces are defined by ψ, I, ϕ, $p =$ constant, respectively. The scalar product of Eq. (1) with $\hat{\boldsymbol{\theta}}$ leads to an equation indicating the deviation of the current surface I from the magnetic surface ψ as follows,

$$nm[(\boldsymbol{v}\cdot\nabla)\boldsymbol{v}]_\theta = -\frac{1}{(2\pi r)^2}\frac{\partial(I,\psi)}{\partial(r,z)}. \tag{6}$$

Similarly, the scalar products of Eqs. (1) and (2) with the magnetic field $\boldsymbol{B}$ yield

$$nm[(\boldsymbol{v}\cdot\nabla)\boldsymbol{v}]\cdot\boldsymbol{B} = \frac{1}{2\pi r}\frac{\partial(p,\psi)}{\partial(r,z)}, \tag{7}$$

$$\frac{\partial(\phi,\psi)}{\partial(r,z)} = \frac{1}{en}(\frac{T_e}{T_e+\gamma T_i})\frac{\partial(p,\psi)}{\partial(r,z)}. \tag{8}$$

Thus, the convective derivative term $nm[(\boldsymbol{v}\cdot\nabla)\boldsymbol{v}]$ induces the derivations of the current, isobaric and equipotential surfaces I, p, ϕ from the magnetic surface ψ. Conversely, if the convective derivative term is negligibly small, all of the surfaces I, p, ϕ, ψ are coincident. Now, we get the Grad-Shafranov equation including electric fields in case of neglecting the convective derivative term, as follows.

$$\frac{1}{(2\pi r)^2}\left[\frac{1}{\mu_0}\mathcal{L}\psi + \mu_0 I\frac{\partial I}{\partial\psi}\right] + \frac{\partial p}{\partial\psi} - (\epsilon_0\nabla^2\phi)\frac{\partial\phi}{\partial\psi} = 0, \tag{9}$$

3. Calculations of Magnetic and Potential Surfaces

Here, we discuss a torus plasma where the minor and major radii are a and R, respectively. Thus, we use the toroidal coordinates ρ, θ, ω; $r = R + \rho\cos\omega, z = \rho\sin\omega$. In order to survey the nature of the solutions of Eq. (9), we solve this under simple assumptions as follows. $\psi(a) = 0$, and $\phi(a) = 0$. In the plasma, $\partial p/\partial\psi =$ constant, $I\partial I/\partial\psi =$ constant, and $\partial\phi/\partial\psi = C$ (= constant). The inverse aspect ratio a/R and the toroidal beta is considerably smaller than 1.

It is convenient to use the ratio δ_0 of $(\epsilon_0\nabla^2\phi)\partial\phi/\partial\psi$ with $\mathcal{L}\psi/(2\pi r)^2\mu_0$ in Eq. (9). Under the above assumption, this is rewritten as $\delta_0 = (\epsilon_0 E_\rho^2(a)/2)/(B_\omega^2(a)/2\mu_0) = (2\pi R)^2\epsilon_0\mu_0 C^2$. We put $\delta = (1-\delta_0)/(1+\delta_0)$. Then, $\delta = 1$ and -1 means the pure Tokamak and the pure magnetoelectric torus, respectively. The change of δ leads the plasma from the Tokamak to the magnetoelectric torus continuously.

The solutions of Eq. (9) under the above assumption are

$$\psi_{out} = -\psi(0)\{2\ln\frac{\rho}{a} + [\ln\frac{\rho}{a} + \lambda_1(1-\frac{\rho^2}{a^2})]\frac{\rho}{R}\cos\omega\}, \tag{10}$$

$$\phi_{out} = -C\psi(0)\{2\ln\frac{\rho}{a} + [-ln\frac{\rho}{a} + \lambda_2(1-\frac{\rho^2}{a^2})]\frac{\rho}{R}\cos\omega\}, \tag{11}$$

$$\psi_{in} = -\psi(0)\{-(1-\frac{\rho^2}{a^2})(1+\lambda_3\frac{\rho}{R}\cos\omega)\}, \tag{12}$$

and $\phi_{in} = C\psi_{in}$. Here, $\lambda_1 = (\beta+0.75)/\delta - 1, \lambda_2 = (\beta+0.75)/\delta, \lambda_3 = (\beta+0.75)/\delta - 0.5$. $\beta = < p > /(\epsilon_0 E_\rho^2(a)/2 + B_\omega^2(a)/2\mu_0)$ and indicates the generalized poloidal beta.

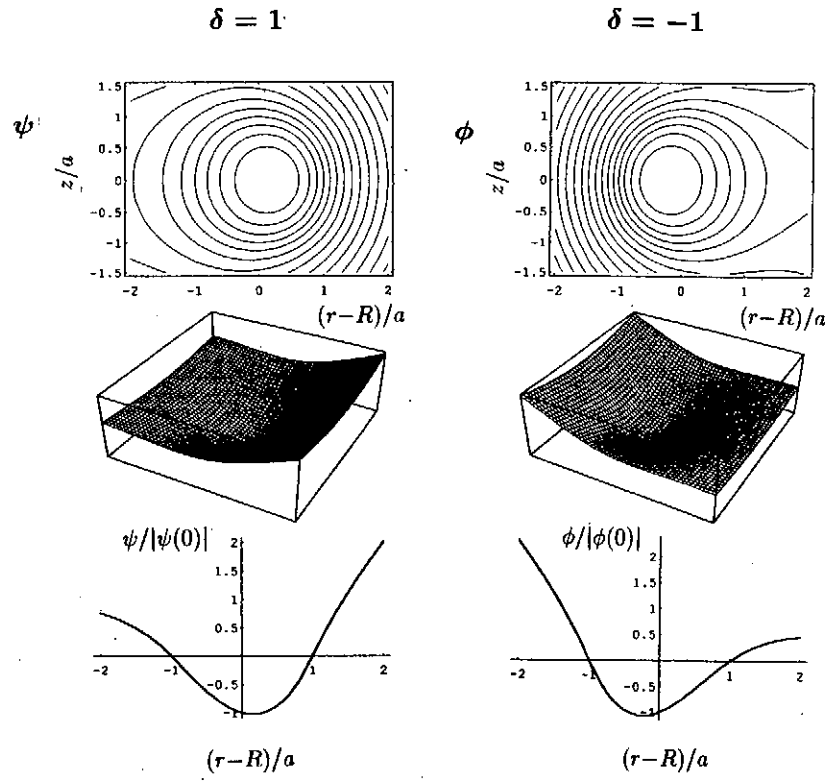

Fig. 1. Equilibrium magnetic surfaces ψ of a Tokamak ($\delta = 1$) and equilibrium potential surfaces ϕ of a magnetoelectric torus ($\delta = -1$). $\beta = 1.4, a/R = 0.2$.

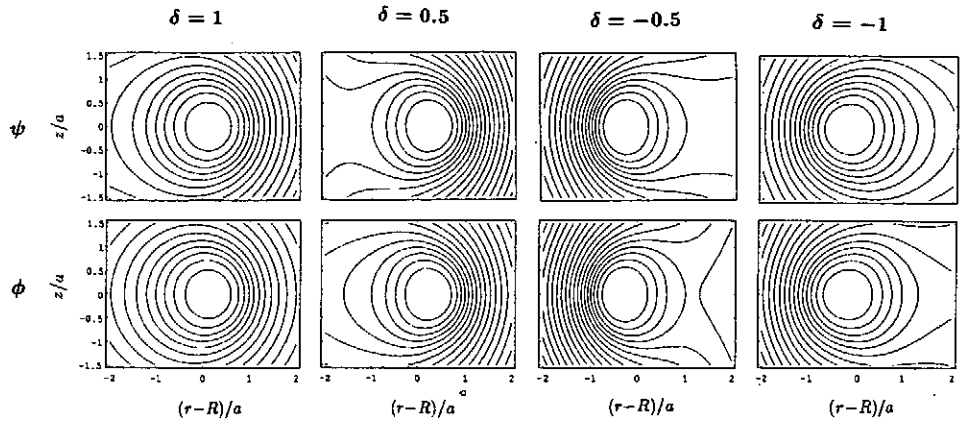

Fig. 2. Equilibrium magnetic surfaces and equilibrium potential surfaces with δ as a parameter. $\beta = 1.4, a/R = 0.2$.

The equilibrium surfaces of a Tokamak and a magnetoelectric torus are shown in Fig. 1. The toroidal hoop force is sustained by the steep magnetic surfaces on the outer side of the Tokamak, and by the steep potential surfaces on the inner side of the magnetoelectric torus. As shown in Fig. 2, the parameter δ changes the surfaces, continuously.

The parameter of the convective derivative term ν is defined as the ratio of $nm(\boldsymbol{v}\cdot\boldsymbol{\nabla})\boldsymbol{v}\cdot\boldsymbol{\nabla}\psi/|\boldsymbol{\nabla}\psi|^2$ with $\mathcal{L}\psi/(2\pi r)^2\mu_0 - (\epsilon_0\nabla^2\phi)\partial\phi/\partial\psi$. ν is rewritten as $\nu = 0.25(\omega_{pi0}/\omega_{ci0})^2(1-\delta)/\delta$. Thus, the convective derivative term is able to be neglected when $\nu \ll 1$.

4. Conclusions and Acknowledgments

Under the assumptions of neglecting the convective derivative term, we derive a new equilibrium equation of the magnetized plasma including electric fields. This equation describes the equilibrium plasma from the Tokamak to the magnetoelectric torus, continuously.

We appreciate Prof. H. Sanuki and Prof. H. Sugama for their discussion, and Prof. D. Grésillon for their cooperation.

References

[1] V. D. Shafranov: Soviet Physics JETP **6** 545 (1958).

[2] T. H. Stix: Phys. Rev. Lett. **24** 135 (1970).

Three-Dimensional Hybrid Simulation Study of Interactions between the Solar Wind and Unmagnetized Planets

Hironori Shimazu
Space Science Division, Communications Research Laboratory,
Koganei, Tokyo 184-8795 Japan

ABSTRACT

The interaction between the solar wind and an unmagnetized planet (Venus or Mars) was investigated in the computer simulations by using a three-dimensional hybrid code (kinetic ions and massless fluid electrons). The purpose of this study is to examine the kinetic effects such as ion pickup and mass loading on macro-scale structures around the planet. The results showed that the shock size and the magnetic barrier intensity were asymmetrical in the direction of the convection electric field because of O^+ ions picked up from the side of the planet to which the convection electric field was pointing.

1 Introduction

Magnetized plasma flow around an obstacle has been studied and the results of these studies have been applied to the interaction between the solar wind and unmagnetized planets (Venus and Mars). Studies of the interaction were summarized in Luhmann (1986) and Luhman and Brace (1991).

Since the solar wind is supersonic and the mean free path of the plasma particles constituting the solar wind is much larger than the size of planets, the collisionless shock is formed in front of the planet. The gas dynamic theory has been used to explain the location and shape of the shocks around Venus and Mars. The solar wind interaction with these planets has also been the subject of magnetohydrodynamic (MHD) simulations.

Although the gas dynamic theory and MHD simulations have been useful in investigating many kinds of problems, they are invalid when the scale of the Larmor radius of ions must be considered. Since the radius of Mars, for example, is comparable to the Larmor radius of solar wind protons, we must therefore use some other methods taking into account the kinetic effects of ions. The hybrid code is one of the best simulation methods for studying the effects because it treats ions as gyrating particles. This paper reports the results of three-dimensional hybrid code simulations in a global simulation system (size of the simulation box $\gg$ size of the planet) including the magnetotail. In previous hybrid simulation studies (Brecht, 1997; Shimazu, 1999) the planet was treated as a solid sphere, and at the surface of the sphere particles were absorbed or reflected. In this paper we introduce planetary plasma.

The most prominent feature caused by the kinetic effects is asymmetry in the direction of the $-\boldsymbol{v}_{sw} \times \boldsymbol{B}$ convection electric field ($\boldsymbol{v}_{sw}$: solar wind speed, $\boldsymbol{B}$: interplanetary magnetic field). In the framework of the MHD all the physical parameters are symmetric in this direction. However observations and the previous hybrid simulations showed

the asymmetry of the shock geometry and the magnetic field intensity. The purpose of this study is to examine the kinetic effects such as ion pickup and mass loading on the asymmetry of macro-scale structures around the planet.

2 Model

The simulation used the three-dimensional Cartesian coordinate system in which the grid cells were spaced equally and there were 64 in each of the x, y, and z directions. The average number of particles in one grid cell was 16. The solar wind was emulated by using a super-Alfvénic plasma (number density n_0, velocity $v_{sw} = 4V_A$ where V_A is the Alfvén velocity) continuously injected into the simulation system from the $x = 0$ plane. The bulk velocity of the solar wind was parallel to the x axis, and the solar wind particles were removed from the simulation system when they reached the other boundary. Planetary plasmas distributed uniformly in a sphere (radius $R = 25.6c/\omega_{pi} = 6.4\rho$, where c is the speed of light, ω_{pi} is the proton plasma frequency, and ρ is the Larmor radius of the solar wind protons) were placed at the center of the simulation box. The sphere is also a source of planetary plasmas and the loading rate corresponds to $0.256\omega_{pi}$.

The initial ambient magnetic field $\boldsymbol{B}$ was given by the potential field:

$$\boldsymbol{B} = \begin{cases} \nabla \left\{ B_0 y \left(1 + \dfrac{R^3}{2r^3} \right) \right\} & (r > R) \\ 0 & (r < R), \end{cases} \tag{1}$$

where $B_0/(4\pi m_i n_0)^{1/2} \equiv V_A = 1.0 \times 10^{-4} c$, $r^2 = (x - L/2)^2 + (y - L/2)^2 + (z - L/2)^2$, m_i is the proton mass, and L $(= 8R)$ is the size of the simulation box. The electrical resistivity of the solar wind was assumed to be zero. The initial temperature of the ions was assumed to be the same as that of the electron fluid and to be constant in space. The ratio of the ion thermal pressure to the magnetic pressure of the solar wind (i.e., β_i) was assumed in this study to be 1. At $t = 0$ the dynamic pressure of the solar wind balances with the thermal pressure of the planetary plasma.

We compare the two cases; One is that the planetary ion species consists of protons (case A) and the other is that it consists of oxygen ions (case B).

3 Results

Figures 1a and 1b respectively show the x component of the average proton velocity and the magnetic field intensity at $\omega_{ci}t = 37.5$ in case A, where ω_{ci} is the proton Larmor frequency. These figures are cross sections for the $y = L/2$ plane, which cuts through the center of the planet. As shown in Figure 1a, on the upstream side of the planet the velocity decreases sharply. A bow shock is generated there. Figure 1b shows that the magnetic barrier, where the magnetic field is larger than the typical value in the magnetosheath, is formed around the planet. The magnetotail is formed on the downstream side of the planet. Figure 1c shows that the planetary protons are confined and that they do not escape much to interplanetary space. The magnetic barrier can prevent protons from escaping because their Larmor radius is less than the width of the magnetic barrier.

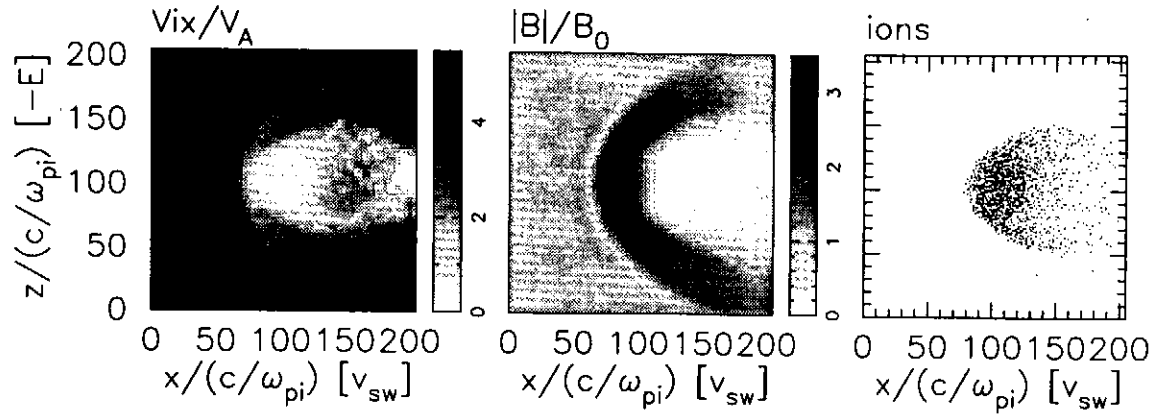

Figure 1: The $y = L/2$ plane at $\omega_{ci}t = 37.5$ in case A: (a) the x component of the proton velocity, (b) the magnetic field intensity, and (c) the distribution of planetary protons.

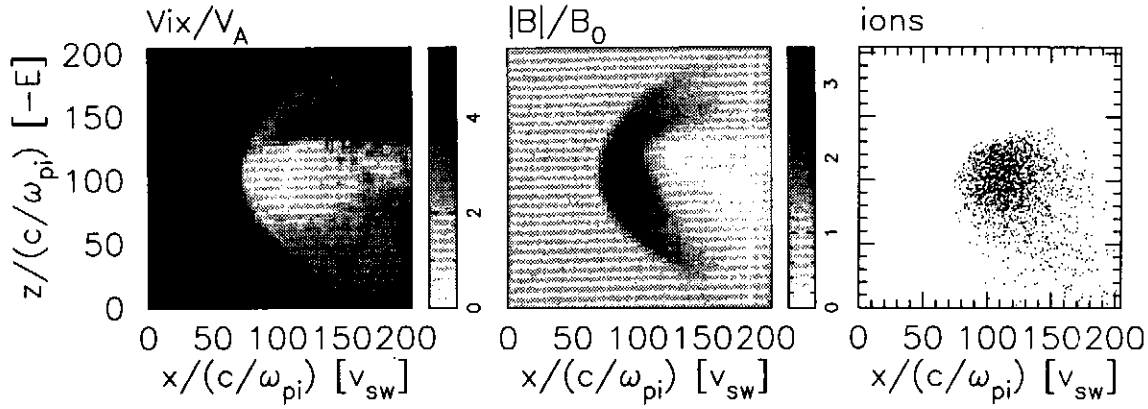

Figure 2: The $y = L/2$ plane at $\omega_{ci}t = 37.5$ in case B: (a) the x component of the ion velocity, (b) the magnetic field intensity, and (c) the distribution of planetary O^+ ions.

Figure 2 show the results of case B. Clear asymmetry in the direction of the $-\boldsymbol{v}_{sw} \times \boldsymbol{B}$ convection electric field ($-z$ direction) were found in this case. Figure 2a shows, for the $y = L/2$ plane, the x component of the ion velocity. The flow near $x = 150c/\omega_{pi}, z = 140c/\omega_{pi}$ (upper side) is accelerated to a speed greater than that of the solar wind by the Lorentz force, while the flow on the other side (lower side) is decelerated by mass loading of the planetary oxygen ions.

Figure 2b shows that the magnetic barrier becomes weak downstream on the side of the planet to which the convection electric field is pointing (lower side). As shown in Figure 2c planetary oxygen ions escape to interplanetary space on the lower side. Because these escaping ions can be seen only on this side, they are picked up by the solar wind electric field. These picked up ions stop formation of the magnetic barrier in the downstream region because of the diamagnetic current.

Figure 3 shows the magnetic field intensity for the $x = L/2$ plane at $\omega_{ci}t = 37.5$ in case B. The cross section of the shock is an ellipse. The lengths of the major axis and

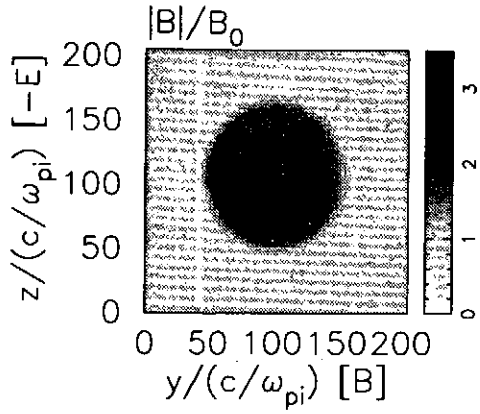

Figure 3: Magnetic field intensity for the $x = L/2$ plane at $\omega_{ci}t = 37.5$ in case B.

the minor axis differ by $0.21R$. This difference is too large to be explained by the Mach cone asymmetry. The shape of the boundary of the planetary plasma also changed from an initial circle to an ellipse. The lengths of the major axis and the minor axis differ by $0.08R$. This is caused by the pinch effect of the magnetic field and the ion movement in the direction of the electric field.

This figure also shows another asymmetry in the direction of the electric field. The shock size is smaller on the side of the planet to which the convection electric field is pointing (lower side) than on the other side (upper side). This asymmetry is caused by the reduction of the Alfvén and fast mode velocity because of the mass loading of O^+ ions on the lower side. However this asymmetry in shock size is opposite the asymmetry actually observed at both Venus (Alexander *et al.*, 1986) and Mars (Zhang *et al.*, 1991). This discrepancy indicates that the observed asymmetry is due to effects not included in this simulation. This discrepancy is a future problem.

References

Alexander, C. J., J. G. Luhmann, and C. T. Russell, Interplanetary field control of the location of the Venus bow shock: Evidence for comet-like ion pickup, *Geophys. Res. Lett.*, **13**, 917-920, 1986.

Brecht, S. H., Hybrid simulations of the magnetic topology of Mars, *J. Geophys. Res.*, **102**, 4743-4750, 1997.

Luhmann, J. G., The solar wind interaction with Venus, *Space Sci. Rev.*, **44**, 241-306, 1986.

Luhmann, J. G., and L. H. Brace, Near-Mars space, *Rev. Geophys.*, **29**, 121-140, 1991.

Shimazu, H., Three-dimensional hybrid simulation of magnetized plasma flow around an obstacle, *Earth Planets and Space*, **51**, 383-393, 1999.

Zhang, T. L., K. Schwingenschuh, H. Lichtenegger, W. Riedler, C. T. Russell, and J. G. Luhmann, Interplanetary magnetic field control of the Mars bow shock: Evidence for Venuslike interaction, *J. Geophys. Res.*, **96**, 11265-11269, 1991.

Simulation study of quasi-perpendicular shock waves in a multiple-ion-species plasma

N. Terada

Department of Geophysics, Graduate School of Science, Kyoto University

Abstract: Supercritical perpendicular shock waves propagating in a plasma containing electrons and two positive ions (i.e., protons and alpha particles) are studied using a one-dimensional electromagnetic hybrid code. It is found that, as the number density ratio of heavy ions to protons is increased, the shock with a moderately high Mach number becomes more dynamic and changes its structure periodically. In this brief report, we show a typical example of the multi-ion shock exhibiting a periodic variation of its structure, and discuss the underlying mechanism of the dynamic process.

1 Introduction

In a multi-ion-species plasma, there are many interesting subjects introduced by the presence of heavy ion components. For instance, in the downstream region of a multiple-ion perpendicular shock, a standing long-wavelength perturbation called the bi-ion hybrid wave (or ion-ion hybrid wave) is generated by the coupling of protons and heavy ions [*Motschmann et al.*, 1991]. Even if we start from the same flow velocities, as the incident ions pass through the shock transition, each ion component will have a different downstream bulk velocity due to the different reaction to the electromagnetic fields. The resulting difference in the bulk velocities just behind the shock will lead to the generation of a bi-ion hybrid wave downstream of the shock. Here, we show that, in a particular situation of a supercritical perpendicular shock, the trailing bi-ion hybrid wave has a sufficiently large influence to cause a periodic variation of the shock structure.

2 Periodic Variation of the Shock Structure

The numerical model we use is a one-dimensional electromagnetic hybrid code in which electrons are treated as a massless fluid and the individual particle orbits of ions are followed kinetically in the four-dimensional phase space (x, v_x, v_y, v_z). We present here a simulation result obtained with the proton Alfvén Mach number $M_{Ap} = V_{shock}/V_{Ap} \sim 9$, the number density ratio $n_\alpha/n_e = 0.1$, and the upstream electron and ion beta $\beta_e = \beta_p = 1.0$ and $\beta_\alpha = 0.5$, respectively, where $V_{Ap} = B_{z0}/\sqrt{\mu_0 m_p n_{p0}}$ is the upstream proton Alfvén velocity, β is the ratio of thermal to magnetic pressure, and subscripts e, p, and α denote electron, proton, and alpha particle (He^{2+}) species, respectively. The upstream thermal velocity of the alpha particles is the same as that of the protons. The mass and charge ratio are taken

to be $m_\alpha/m_p = 4$ and $q_\alpha/q_p = 2$, respectively. We generate the shock by the reflection method with physical piston boundary conditions. Particles are continuously injected from the left boundary of the simulation box with the proton Alfvén Mach number of 6, and the shock propagates toward the left side with the mean proton Alfvén Mach number of ~ 3 in the rest frame of the simulation box, that is, the Doppler-shifted propagation speed of the shock is about $M_{Ap} \sim 9$ with respect to the upstream flow.

Figure 1 illustrates the magnetic field profile, the $x - v_x$ phase space and the number density profile for each ion species at four different time steps during one oscillation cycle. In such a high M_{Ap} shock, the flow velocities of each ion component just downstream of the shock are very different, such that a considerably large amplitude bi-ion hybrid wave is generated. Therefore, the phase bunched motion of the alpha particles turns around and even indicates "loop" structures in the $x - v_x$ phase space, where distinct enhancements of n_α are observed. While the bi-ion hybrid resonance is a purely electrostatic mode [*Smith and Brice,* 1964], the trailing bi-ion hybrid wave has a fairly long wavelength and involves magnetic perturbation. Considering the quasi-charge neutrality condition, $n_e = n_p + 2n_\alpha$, and that B_z is nearly proportional to n_e, we expect magnetic field B_z to have a relatively large value in the region where n_p and n_α are relatively large.

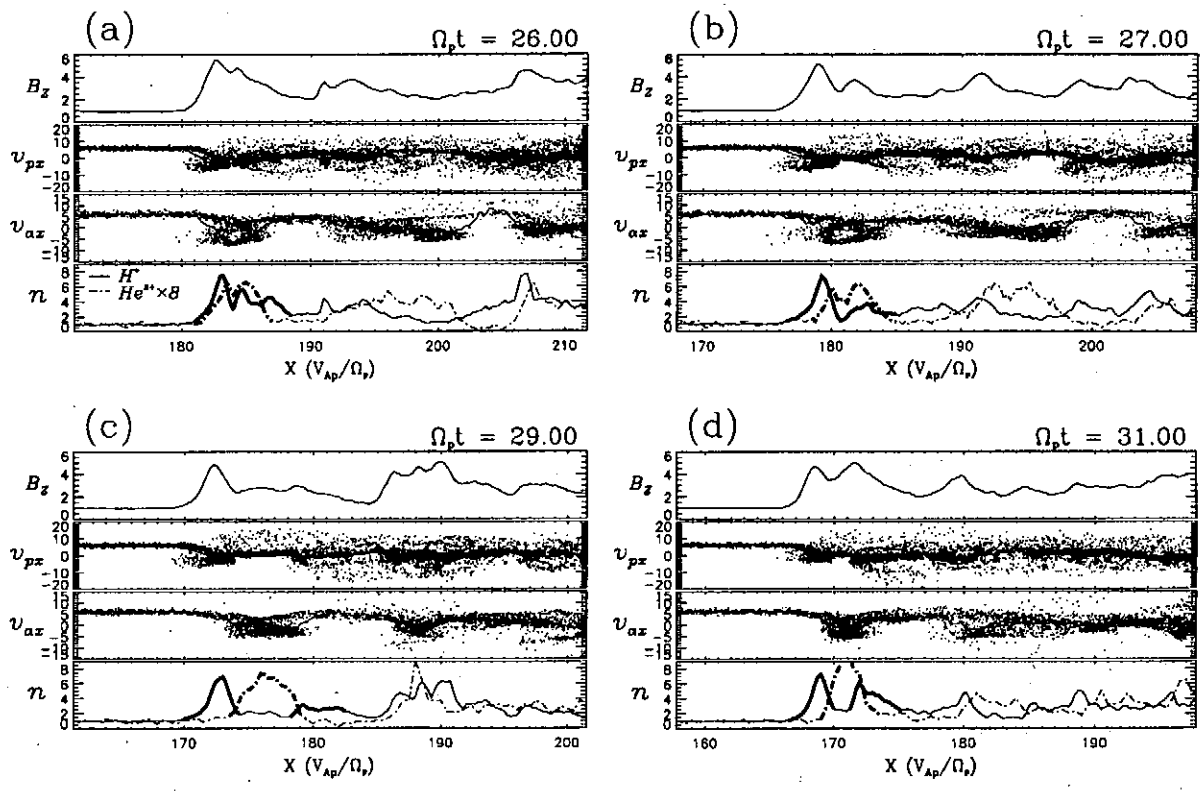

Fig. 1. Plots of the magnetic field B_z, the $x - v_x$ phase space for protons and for alpha particles, and the number density for each ion species at (a) $t = 26.0\Omega_p^{-1}$, (b) $t = 27.0\Omega_p^{-1}$, (c) $t = 29.0\Omega_p^{-1}$, and (d) $t = 31.0\Omega_p^{-1}$. The magnetic field, velocities, and number densities are normalized to the upstream values of B_{z0}, V_{Ap}, and n_{p0}. The regions of n_p and n_α enhancements are emphasized with thick solid curves and thick dashed curves in the panels for the number density profiles.

As can be seen in Figure 1, some fraction of the incident protons are reflected just upstream of the shock and then forms a gyrating stream in the downstream region in a similar fashion for the single-ion-species shock, while the alpha particles change their velocities only slightly due to their large inertia in the immediate vicinity of the shock. In the downstream fields, the alpha particles begin to gyrate, and their phase bunched gyrating stream dynamically shapes the number density profile. Since the mass-to-charge ratio for the alpha particles is twice that for the protons, the 1st peak of n_α locates between the 1st and the 2nd proton density enhancement regions. We call these alpha particle and proton enhancement regions "alpha particle pulse" and "proton pulse" in this paper. For the sake of visualization, the 1st and the 2nd proton pulses and the 1st alpha particle pulse in the panels for the number density profiles in Figure 1 are marked with thick solid curves and thick dashed curves, respectively. Note that, for high M_A shocks as in this case, the gyrating stream of reflected protons is quite energetic and the proton density enhancement regions are prominent [*Leroy et al.*, 1982].

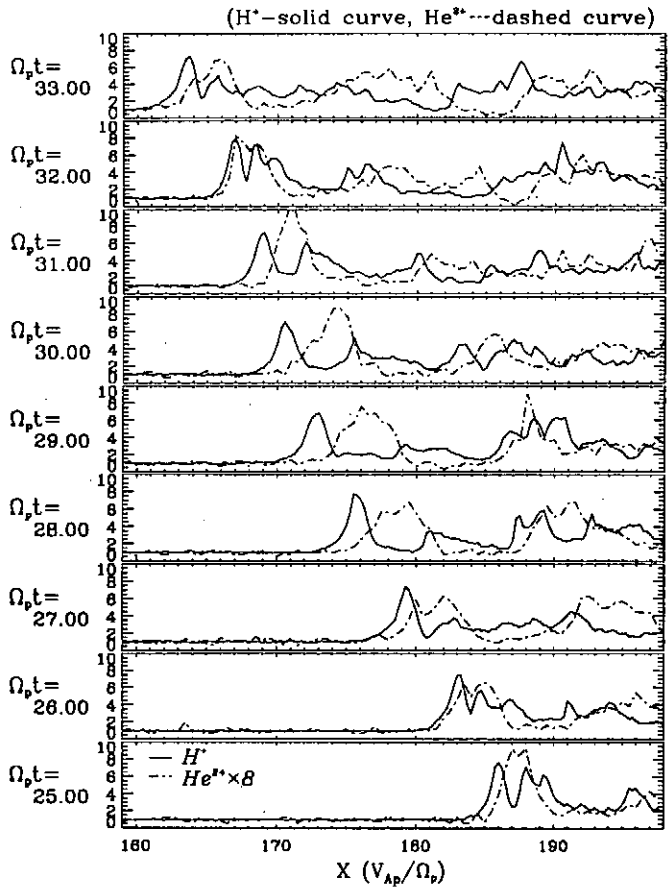

Fig. 2. Time sequence of the number density profiles for protons (solid curve) and for alpha particles (dashed curve).

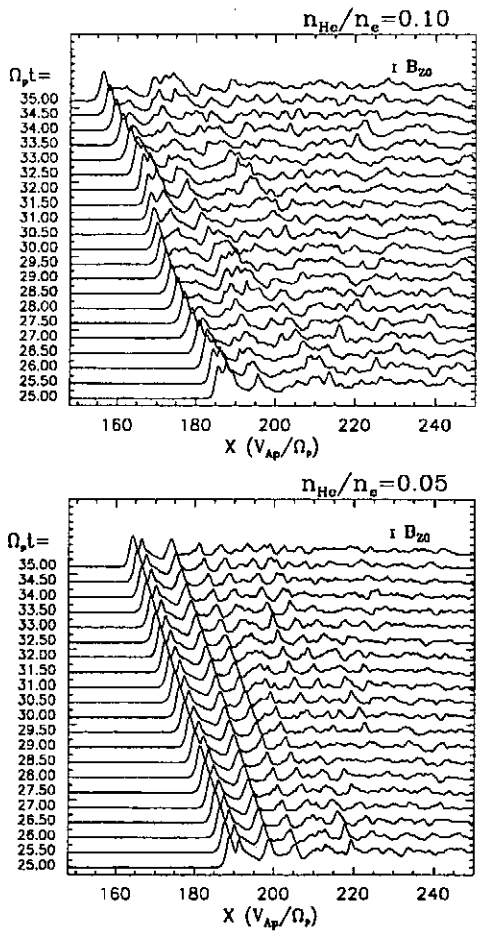

Fig. 3. Time-stacked profiles of the magnetic field B_z for $n_\alpha/n_e = 0.10$ (upper panel) and for $n_\alpha/n_e = 0.05$ (lower panel).

In Figure 1(a), we can see that the alpha particles have a large number density at the position of the 1st proton pulse, where we can also expect magnetic field to increase slightly. If the amount of magnetic field increase is small (e.g., in the case of $n_\alpha/n_e = 0.05$), it is diffused through the electrical resistivity and a reasonably steady shock structure would be achieved. In this case, however, newly injected protons are strongly deflected and decelerated at the 1st proton pulse, and the 1st proton pulse moves forward while leaving the alpha particle pulse behind (Figure 1(a)→(b)→(c)). Since alpha particles are deflected in the downstream fields behind the shock ramp rather than completely decelerated just at the shock foot and ramp regions due to their large inertia, the alpha particle pulse cannot follow the movement of the 1st proton pulse coherently. Accompanied by the recovery of the 2nd proton pulse, alpha particles are strongly deflected there and the alpha particle pulse begins to move forward until it overtakes the 1st proton pulse in front of it (Figure 1(c)→(d)). The cycle is completed by a return to the state of Figure 1(a), where B_z at the 1st proton pulse increases again. In addition, further downstream of the shock, similar movements of the pulses can be observed, which result from the interaction between the proton gyrating stream and the alpha particle pulses. We illustrate a time series of the number density profiles in Figure 2, where the time variations of the positions of the proton and the alpha particle pulses can be clearly seen.

We have also performed simulation runs with a wide range of model parameters, and found dependences on parameters such as the number density ratio, Mach number, upstream ion beta, heavy ion mass ratio and so on. In the upper panel of Figure 3, the time-stacked profiles of the magnetic field B_z for $n_\alpha/n_e = 0.1$ are plotted, where quasi-periodic back and forth movements of the pulses are seen, while the lower panel shows a reasonably steady shock structure for $n_\alpha/n_e = 0.05$. For $M_{Ap} \sim 9$, $\beta_p = \beta_\alpha n_p/4n_\alpha = 1$, and $\eta = 1.5\Omega_p/\epsilon_0\omega_{pp}^2$, the non-stationary structure appears when the number density ratio n_α/n_e exceeds ~ 0.07. By varying the Alfvén Mach number while maintaining the same values for the other parameters, we found that the simulation results of multi-ion shocks show the non-stationary structure discussed above, when M_{Ap} exceeds the threshold value of ~ 7. Detailed examination of these parameter dependences gives us the opportunity to confirm the underlying mechanism discussed above and much deep insight into this dynamic process.

References

Leroy, M. M., D. Winske, C. C. Goodrich, C. S. Wu, and K. Papadopoulos, The structure of perpendicular bow shocks, *J. Geophys. Res.*, **87**, 5081 (1982).

Motschmann, U., K. Sauer, T. Roatsch, and J. F. McKenzie, Subcritical multiple-ion shocks, *J. Geophys. Res.*, **96**, 13841 (1991).

Smith, R. L., and N. Brice, Propagation in multicomponent plasmas, *J. Geophys. Res.*, **69**, 5029 (1964).

TIME EVOLUTION OF THE EARTH'S MAGNETOTAIL ASSOCIATED WITH SUBSTORM ONSET: GEOTAIL OBSERVATIONS

S. Machida and Y. Miyashita

Department of Geophysics, Graduate School of Science, Kyoto University,
Kyoto 606-8502, Japan

and

GEOTAIL/LEP-MGF team

Abstract. Temporal changes in the plasma flow and magnetic fields of the Earth's magnetotail were studied by applying a superposed epoch analysis method to substorm events by employing plasma and magnetic field data obtained by GEOTAIL spacecraft. The onset times of the substorms were determined with Pi-2 pulsations at mid-latitude geomagnetic stations.

It was found that the earthward flow from the distant neutral line was enhanced at least 20 min prior to the onsets, and that the tailward flow associated with plasmoids started about 2 min before the Pi-2 onsets. The earthward flow became somewhat coherent 1 min before the onsets in the near tail region. The variation of the northward magnetic field component was found to increase at X ~ -10 R_E and decrease at X ~ - 28 R_E simultaneously in the premidnight tail immediately after the onsets. These variations definitely correspond to the dipolarization and plasmoid formation, respectively. Furthermore, it is possible to locate the center of the highest possibility of a diffusion region, i.e., the near-Earth neutral line at (X, Y) ~ (- 19, 6) R_E. To interpret our observational results, we propose a thin-current reconnection model in which very thin current layers extend from the diffusion region in both the earthward and tailward directions.

1. Introduction

A number of substorm models have been proposed so far. Among these, the near-Earth neutral line (NENL) model excels in the point that it can explain the generation of plasmoids, and accordingly it is regarded as one of the primary substorm models [*Hones*, 1976]. However, there is still some debate that the earthward flows during substorms known as bursty bulk flows (BBFs) are always intermittent and that they are not capable of carrying the amount of magnetic flux and energy required for a substorm [*Angelopoulos et al.*, 1994]

In the meantime, auroral break-ups associated with a substorm occur in the region which can be mapped to the premidnight tail at the distance of ~ 8 R_E. Various changes in the

magnetic fields and current system, such as a dipolarization and a current disruption, take place in that region. In order to explain such a transition from a quiet to a disturbed state, various models, such as the ballooning instability [*Roux et al.*, 1991], the kinetic drift instability [*Lui et al.*, 1990] or the unstable magnetosphere-ionosphere coupling system [*Kan et al.*, 1988], have been proposed. Those models have the advantage of explaining the location and timing of the auroral break-ups, however, as a drawback, it is often said that they cannot necessarily account for the creation of a plasmoid as a natural consequence.

Therefore, it is a matter of great importance to examine the timing of the plasma flow changes, the magnetic field changes, and the variations in other parameters at X ~ - 10 R_E, i.e., the variations associated with the dipolarization or the current disruption, and those observed at X ~ - 30 R_E associated with plasmoid formation. With such a timing analysis, one can expect to solve the causality relationship issue and derive significant information to clarify the principal mechanism of substorms.

To demonstrate the temporal changes of the magnetotail, we separate our report into two parts in which variations of the mid- and distant tail regions in terms of the earthward and tailward flow velocities will be shown first, and those of the near and mid-tail regions will be described in the second part.

We used plasma moment and magnetic field data acquired with the Low Energy Particle/ Energy Analyzer (LEP/EA) and Magnetic Field Instrument (MGF) onboard the GEOTAIL spacecraft. The time resolution of both data is 12 sec. A detailed description of the LEP and the MGF can be found in papers by *Mukai et al.* [1994] and *Kokubun et al.* [1994], respectively.

There may be several different ways to determine the substorm onset times, but we determined them by investi-gating Pi-2 pulsations in the geomagnetic records taken at Kakioka and Wingst stations located at (26.94° , 208.29°) and (54.15° , 95.26°) in the geomagnetic dipole coordinates, respectively.

2. Results

2.1. Mid- and Distant Tail Regions

In the first part of this study, we used the GEOTAIL data obtained during the period from September 14, 1993 to February 28, 1995. The data around X ~ - 30 R_E was obtained in January and February, 1995. The spacecraft traversed regions around X ~ - 60 R_E in September, 1993 and February, 1994; X ~ - 90 R_E in January, 1994; X ~ - 160 R_E in October, 1993 and October, 1994; and X ~ - 200 R_E in April, 1994.

To determine the onset times, we used ground magnetic records at Kakioka and Wingst. We selected either a single onset or the first of multiple onsets requiring that the ground

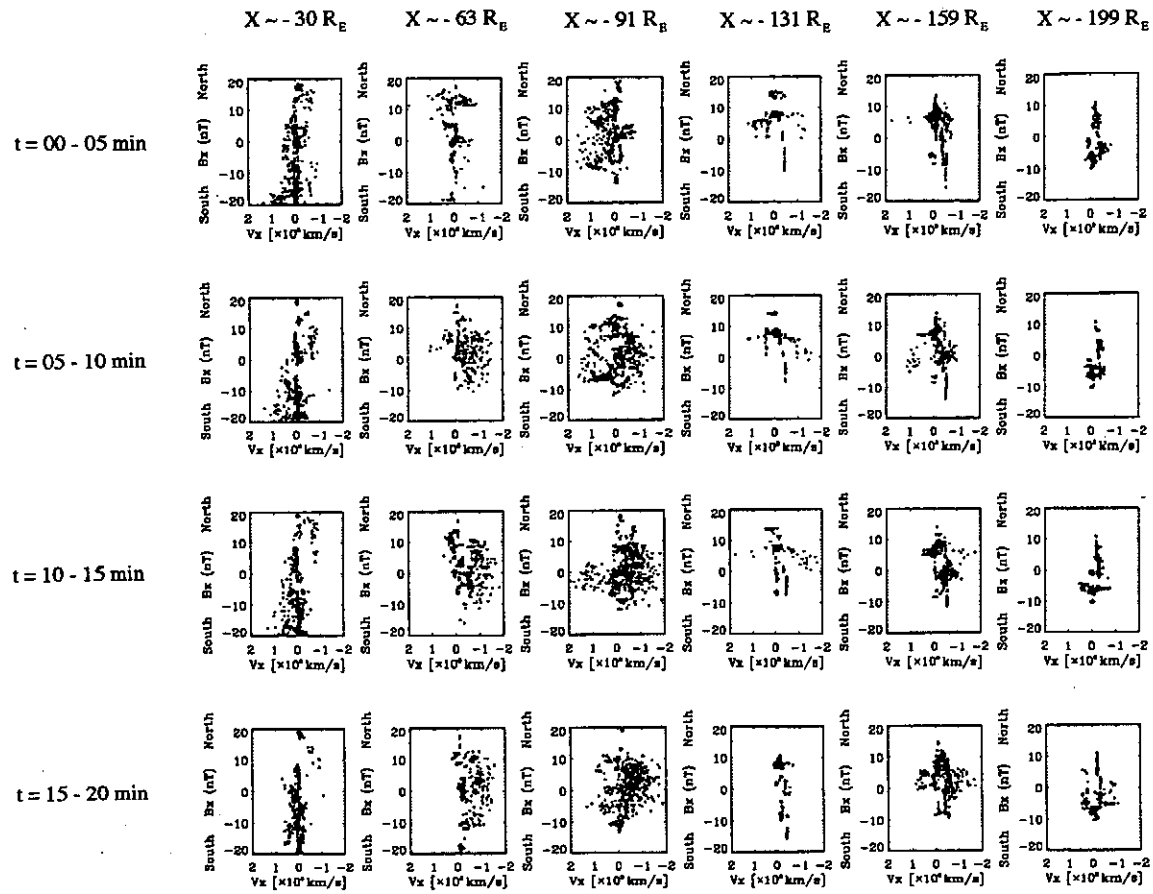

Figure 1. Scatter plots of Vx vs. Bx at six different locations as indicated at the top for different time intervals relative to the Pi-2 onsets on the ground. Each dot corresponds to the averaged plasma flow and magnetic field data for 12 sec.

geomagnetic activity was quiet at least 30 min prior to the onset, and ambiguous events such as extremely small onsets or very gradual onsets was excluded in this analysis. With such criteria, we selected 156 substorm events to be analyzed.

To demonstrate the time variation of the magnetotail plasma flow in association with the substorm onset, scatter plots, as shown in Figure 1, were made which reveals the relation between the earthward flow velocity Vx and magnetic field component Bx at six different locations in the magnetotail with respect to the onset time of Pi-2. Each dot corresponds to the averaged plasma flow velocity and magnetic field for four spacecraft spin periods which is 12 sec. The data spread more in the vertical direction, namely, cover wider |Bx| values when the spacecraft is closer to Earth since the lobe magnetic field is stronger in the near Earth region and monotonically decreases as a function of distance from the center of Earth. One of the most interesting signatures is the clear earthward flow observed at X ~ - 91 R_E for

t = 0-5 min after the onsets. This earthward flow has been already apparent at least 20 min prior to the onsets, i.e. in the growth phase, and still continued in the expansion phase. This flow continued even at t = 05-10 min or later in some cases. In the outermost region X ~ - 199 R_E, the tailward flow was observed throughout the substorm. The location of the flow reversal is not clear, however, the positive and negative scattering of the dots in the region X ~ - 131 R_E and - 159 R_E indicates that it may vary considerably, depending on several conditions, such as the solar wind velocity or the orientation of the interplanetary magnetic field, and how they varied with respect to the onset time. Certainly, our primary interest is the fast flow created in the near Earth region in association with substorms. This fast flow appears at X ~ - 63 R_E in the time interval of t = 00-05 min, and then becomes more prominent in the next time interval. A switch from the tailward flow to the earthward flow is observed at X ~ - 91R_E. The enhanced tailward flow appears in the time interval t = 05-10 min in the inner region of the tail, namely, the region with small values of |Bx|. The population of the earthward flow increases as time elapses in association with the progress of the substorms. It is of interest that both the tailward and earthward flows are mixed at X ~ - 30 R_E in which the neutral line is statistically located in the vicinity. Also, the value of the fastest flow does not reach to 2,000 km/s which can be often observed at X ~ - 63 R_E and - 91 R_E or at further distances. There are cases in which the flow velocity reaches up to 1,000 km/s, which is significantly fast compared to that found in quiet times at X ~ - 30 R_E.

At the distance of X ~ - 131 R_E, unfortunately, the amount of available data was only about 50 % compared to other cases. However, it is evident that the tailward flow will become dominant from t = 15-20 min, even though both earthward and tailward flows are mixed together at the beginning. A similar tendency can be found at the distance of X ~ - 159 R_E. In contrast, the earthward flow is rare and the tailward flow is mostly dominating at X ~ - 199 R_E, as pointed out earlier.

Our results clearly indicated an enhancement of the earthward flow from the distant neutral line (DNL) during the growth phase. This earthward flow continued until about 10 min after the onset of the substorms, i. e., even in the expansion phase. By extending the superposed epoch analysis method used in this study, it is possible to obtain the structure of plasmoids by investigating the plasma data such as number density, the flow velocities, and the temperature as well as the magnetic field data. We will report on these results in a separate paper. Since there were fast tailward flows which seem to have been created in the region around X ~ - 30 R_E associated with the onset of substorms as seen in the plots in Figure 1, we will focus on describing the results of our analysis on the plasma flow and the magnetic field in the inner region.

2. 2. Near and Mid-Tail Regions

As for determining the onset time of the ground Pi-2, 1 sec sampling records, from only the Kakioka station, were used in this part of study, i.e., to study the near and mid-tail regions. We restricted the substorm events to those which occurred during the interval from 1100 to 1900 UT (2000 - 0400 LT) having a positive bay within ±7 min in the H-component of the geomagnetic field relative to a Pi-2 onset. We also required that there were no other Pi-2 pulsations at least for 30 min before the onset for each case to be selected. Further, the

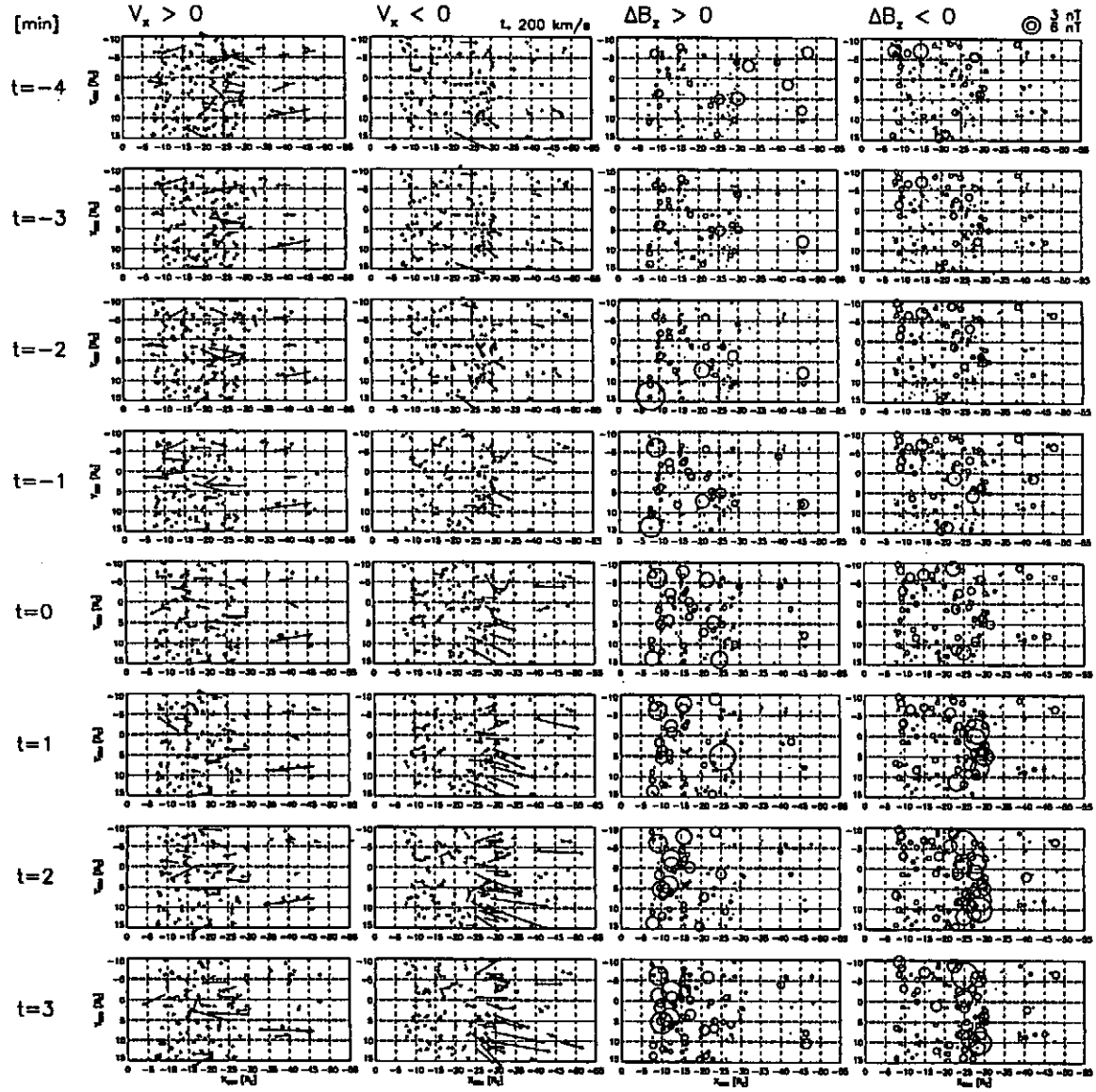

Figure 2. From left to right, the columns show the earthward and tailward flow vectors (Vx, Vy), and the positive and negative deviations of the northward magnetic field component (Δ Bz) from the averaged values from t = - 10.5 to t = - 7.5 min. The flow vectors are those which have a maximum value of |Vx| during the 1 min interval centered at the time indicated on the left. The flow vectors corresponding to 200 km/s dawnward and tailward flows together with the 3 nT and 6 nT magnetic field deviations are indicated at the top.

plasma data from the LEP instrument and the magnetic field data from the MGF instrument, both onboard the GEOTAIL spacecraft during the period from September, 1993 to August, 1997, were used to derive the variations in the magnetotail. The time resolution of both data was, again, 12 sec. By combining the Pi-2 records and the spacecraft location from - 7.5 to - 52.5 R_E in the X-direction, and from - 10 to 15 R_E in the Y-direction in the GSM coordinate system, we selected 243 substorm events for which onset-times were read in 1 min time accuracy.

Figure 2 shows the time evolution of the flow velocity vectors and the deviation of the northward magnetic field component projected on the X-Y plane at 243 different spacecraft locations. The first column is for the positive Vx data, i.e., earthward flows, and the second column is for the negative Vx data, i.e., tailward flows. The flow vectors corresponding to 200 km/s dawnward and the tailward velocities are indicated at the top of the figure. The flow vectors for both earthward and tailward flows are those which have the maximum value of |Vx| during the 1 min interval centered at the time indicated on the left of the figures.

At t = - 4 min, there are some large earthward flow vectors, which we regard as having originated from the DNL. However, there are also some large flow vectors of $Vx < 0$, but most of these have also large duskward flow components. This tendency continued at least from t = - 10 min. Then at t = - 3 min, some duskward flows of a velocity of about 200 km/s appear in the region around (X, Y) ~ (- 30, 7) R_E, which evolve to pronounced tailward flows, characterizing a structure known as a plasmoid. These flows have duskward flow components of 100 km/s at t = 0 min, and show a slightly decreasing duskward velocity after the start of their creation at t ~ - 3 min. After t = 1 min, tailward flows appear with some dawnward flow components around the region $-25 > X\ (R_E) > -30$ and $-10 < Y\ (R_E) < 0$. This can be related to the expansion of the plasmoid as pointed out by *Ieda et al.* [1998].

As for the earthward flows which correspond to BBFs, it seems that they become somewhat coherent at 1 min before the Pi-2 onset. However, if we separate them into parallel and perpendicular components as shown in Figure 3, it turned out that these fast earthward flows are mostly due to the contribution of the parallel motion of the plasma rather than the perpendicular drift motion which is thought to carry the magnetic flux toward Earth.

Figure 2 also shows the temporal change of the north-south component of the magnetic field by obtaining the deviation (ΔBz) of Bz from its averaged value during the growth phase from t = - 10.5 to - 7.5 min. The positive ΔBz events are shown in the third column, and the negative ΔBz events are shown in the fourth column. The magnitude of ΔBz is revealed by a radius of a circle as indicated at the top of the figure. It should be noticed that the indicated values of ΔBz are those when the earthward and tailward flows are most enhanced during each 1 min time interval. There is a tendency for the positive deviation of Bz to gradually be enhanced in the central part of the tail, while the negative deviation of Bz progresses in the region surrounding that of positive ΔBz. There are events in which ΔBz

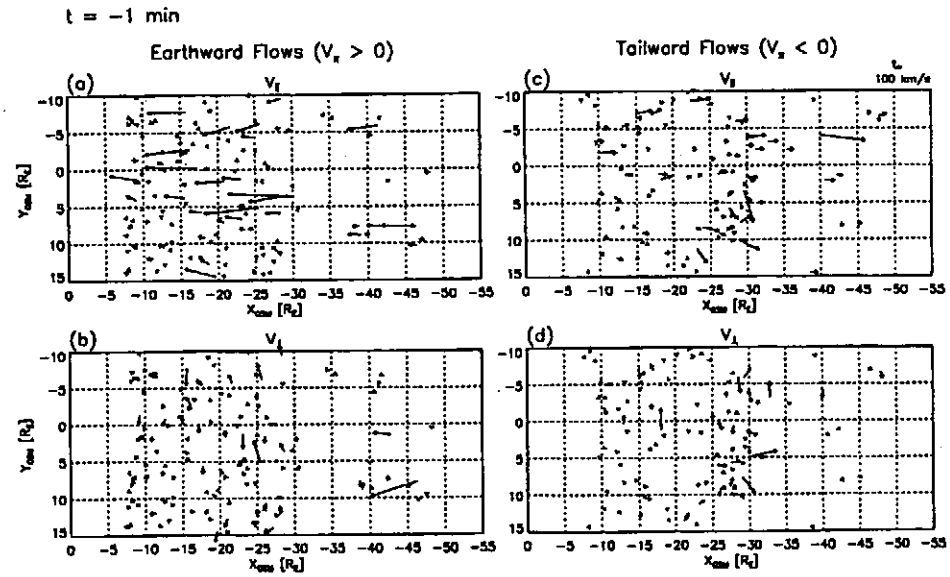

Figure 3. Flow vectors decomposed into parallel and perpendicular components. (a) Parallel velocity vectors for Vx > 0; (b) Perpendicular velocity vectors for Vx > 0; (c) Parallel velocity vectors for Vx < 0; (d) Perpendicular velocity vectors for Vx < 0. The flow vectors corresponding to 100 km/s dawnward and tailward flows are shown in the top right corner.

increases associated with the BBFs in the central part starting at around t = - 2 min. It is not necessarily clear, but they seem to be connected to a notable increase of ΔBz with a magnitude about 5 nT occurring at around (X, Y) = (- 12, 1) R_E soon after the Pi-2 onset on the ground as can be seen from the data of t = 0, 1 and 2 min. Remarkably, a pronounced decrease of ΔBz, also about 5 nT occurs around (X, Y) = (- 28, 7) R_E at the same time. Most of the negative ΔBz accompanies the fast tailward flow of the plasmoid. The region of negative ΔBz also expands in dawnward and duskward directions in accordance with the expansion of the negative Vx region in the same directions. The positive enhancements of Δ Bz in the near-Earth region correspond to the dipolarization of the Earth's magnetic field, which significantly develops after the onset of Pi-2. The dipolarization region also expands in both the dawnward and duskward directions in time.

3. Discussion and Summary

As we have shown, considerable changes occur in the magnetotail during substorms.

Concerning the distant tail region, we found an enhancement of the DNL activity at least 20 min before the onset. The intense earthward flows definitely affect the condition of the near tail and the triggering of substorms. The activity of the DNL continued even after the onset of substorms, and this earthward flow encountered the tailward flow due to the reconnection at the NENL. It was also found that the plasmoid evolution occured not only in a localized region around the NENL but in a much more extended region from X ~ - 30 R_E to X ~ - 90 R_E, i.e., in the mid-tail region.

Concerning the near tail region, we found significant increases and decreases of the Bz field at distances of X ~ - 10 R_E and ~ - 30 R_E regions which took place simultaneously at around t = 1 min. The determination of the Pi-2 onset time has an inherent ambiguity of about 1 min, since the characteristic oscillation period of Pi-2 is from 40 to 150 sec by definition. There are cases in which high-frequency components associated with a Pi-2 burst may improve the accuracy of the onset-time determination. Regardless of these facts, we can conclude that the increase of Bz which corresponds to the dipolarization in the near-Earth region, and the decrease of Bz which corresponds to the plasmoid formation in the downtail region take place simultaneously, and that the magnetic reconnection can be responsible for creating such a time change of Bz.

We found that the first earthward flow became somewhat coherent 1 min before the Pi-2 onset. This earthward flow is regarded as a substorm related BBF. However, upon decomposing the flow vector, it turned out that the earthward flow was mostly due to the parallel motion of plasma, and the perpendicular motion was predominantly duskward or dawnward. To interpret this observational fact, we propose a thin current sheet reconnection model in which thin current layers are extended from the diffusion region in the earthward and tailward directions, with a structure similar to the flux pile-up model proposed by *Priest and Forbes* [1986], but the kinetic effect of ions has to be considered. The ions are unmagnetized in the thin current layers, hence, the duskward ion flow is possible in the central plasma sheet due to the meandering motion, and the diamagnetic drift at the boundary region of the plasma sheet also gives rise to a large duskward flow velocity. The dawnward ion flow is also created by the ExB drift under the existence of the electric field toward the center of the thin current sheet. Meanwhile the magnetic field line across this thin current sheet is highly stretched and the angle between this field line and the plasma sheet boundary is very small, hence, the parallel velocity can be very high, but the perpendicular velocity in the plasma sheet boundary layer is low even if this field line, i.e., the magnetic flux tube, moves with a very high velocity toward Earth.

The region of negative ΔBz is distributed very close to the Earth, surrounding the region of positive ΔBz. Also, it is apparent that the middle point of these negative and positive Δ Bz regions shifts to the duskward side and is located around (X, Y) = (- 20, 5) R_E. While, the tailward plasma flow seems to start around (X, Y) = (- 26, 6) R_E. If we use the plasma flow

to infer the location of the diffusion region, we have to pay special attention to the fact that the region where the tailward flow becomes evident is the region where the ions start to be unmagnetized. Specifically, this can be the tailward edge of the thin current sheet rather than the diffusion region itself.

The earthward flow in the near tail region is very slow, and, it is not necessarily enhanced severely in association with a substorm onset. As shown in a paper by *Miyashita et al.* [1998], this can be clearly demonstrated when we plot the electric field on the X-Y plane. Apparent enhancements of the duskward component to the comparable level of 2 mV/m appear around X ~ - 10 R_E and X ~ - 28 R_E of the tail just before and after the onset of a substorm. This supports the basic principle of the magnetic reconnection which transports an equal amount of the magnetic flux in both the earthward and tailward directions. They also found that the total pressure reduction occurred in the region centered at (X, Y) ~ (- 18, 7) R_E, which is also regarded as a natural consequence of the magnetic reconnection. Synthesizing those results, we propose that the location of the diffusion region is centered at around (X,Y) = (- 19, 6) R_E.

In the region of the thin current layer, we would definitely obtain erroneous values of the rate of the magnetic flux transportation or the Poynting flux if we evaluate them from the bulk flow velocity derived from ion measurements, since most of the ions are regarded as unmagnetized. A study on the structure and characteristics of this thin current layer would be significantly important in understanding the primary mechanism of substorms.

As for the downstream of the separatrix in the magnetic reconnection topology, the magnetized ions are dominant outside the region of the thin current layer. A pair of slow shocks will develop in the downtail region approximately from X = - 30 R_E down to X = - 90 R_E, generating a fully developed plasmoid as shown in the first part of this study. In contrast, the electromagnetic coupling between the magnetosphere and the ionosphere under the constraint of the strong geomagnetic field are significant in the inner tail region of X > - 15 R_E, which reveals quite different characteristics from those of the downtail region separated by the diffusion region even though both can be categorized as the same downstream region of the separatrix.

In this study, we determined the onset of substorms by the Pi-2 event on the ground. Therefore, it should be emphasized that the substorm onset in this paper is actually the Pi-2 onset on the ground. In spite of those facts, the systematic variations of the plasma flow and magnetic fields such as simultaneous sudden increases and decreases of the ΔBz corresponding to the dipolarization and the plasmoid formation, strongly support the validity of our method to use the Pi-2 onset as a time mark. In contrast, the fact that the Pi-2 onset may be used as a valid time mark also suggests that the Pi-2 is closely related to the magnetic reconnection.

Acknowledgments

We would like thank to Profs. C. Z. Cheng , T. Ogino, K. Shibata, M. Tanaka and other colleagues for valuable discussions and comments at the NIFS meeting.

References

Angelopoulos, V., C. F., Kennel, F. V. Coroniti, R. Pellat, M. G. Kivelson, R. J. Walker, C. T. Russel, W. Baumjohann, W. C. Feldman, and J. T. Gosling, Statistical characteristics of bursty bulk flow events, *J. Geophys. Res.*, *99*, 21,257-21,280, 1994.

Hones, E. W., Jr., The magnetotail: Its generation and dissipation, in *Physics of Solar Planetary Environments*, edited by D. J. Williams, pp. 558-571, AGU, Washington, D. C., 1976.

Ieda, A., S. Machida, T. Mukai, Y. Saito, T. Yamamoto, A. Nishida, T. Terasawa, and S. Kokubun, Statistical analysis of the plasmoid evolution with Geotail observations, *J. Geophys. Res.*, *103*, 4453-4465, 1998.

Kan, J. R., L. Zhu, S.-I. Akasofu, A theory of substorms: onset and subsidence, *J. Geophys. Res.*, *93*, 5624-5640, 1988.

Kokubun, S., T. Yamamoto, M. H. Acuna, K. Hayashi, K. Shiokawa, and H. Kawano, The Geotail magnetic field experiment, *J. Geomag. Geoelectr..*, *46*, 7-21, 1994.

Lui, A. T. Y., A. Monkofsky, C.-L. Chang, K. Papadopoulos, and C. S. Wu, A current disruption mechanism in the neutral sheet: A possible trigger for substorm expansions, *Geophys. Res. Lett.*, *17*, 745-748, 1990.

Miyashita, Y., S. Machida, A. Nishida, T. Mukai, Y. Saito, and S. Kokubun, Temporal changes in the near and mid-distant magnetotail associated with substorms obtained by Geotail observations: variations in total pressure and electric field, in *Proceedings of International Conference on Substorms-4*, 195-198,1998.

Mukai, T., S. Machida, Y. Saito, M. Hirahara, T. Terasawa, N. Kaya, T. Obara, M. Ejiri, and A. Nishida, The low energy particle (LEP) experiment onboard the Geotail satellite, *J. Geomag. Geoelectr.*, *46*, 669-692, 1994.

Priest, E. R., T. G. Forbes, New models for fast steady state magnetic reconnection, *J. Geophys. Res.*, *91*, 5579-5588, 1986.

Roux, A., S. Perraut, P. Robert, A. Morane, A. Pedersen, A Korth, G. Kremser, B. Aparicio, D. Rodgers, and R. Pellinen, Plasma sheet instability related to the westward traveling surge, *J. Geophys. Res.*, *96*, 17,697-17,714, 1991.

The Origins of Electrical Resistivity in Magnetic Reconnection

Motohiko Tanaka

National Institute for Fusion Science, Toki 509-5292, Japan

Abstract The inertia motion of electrons along the magnetic field, which is not included in the MHD framework, has been identified by means of the macro-particle simulations as the origin of resistivity (Ohm's law) and reconnection in collisionless plasmas. The finite Larmor radius effect of ions acts to suppress the reconnection rate by increasing the X-point current that is carried by accelerated electrons due to charge separation electric field. The multiple reconnection process is suggested to accomplish the global size reconnection in the solar flares in which kinetic time and space scales are much less than that of the flares.

I. Roles of Resistivity in Reconnection Process

The origins of resistivity in collisionless plasmas have been a mystery of magnetic reconnection since 1960's. By definition, there should not be resistivity in a collisionless plasma, hence, no reconnection. Indeed, Faraday's, Ampere's and Ohm's laws

$$\frac{1}{c}\frac{\partial B}{\partial t} = -\nabla \times E, \tag{1}$$

$$\nabla \times B = \frac{4\pi}{c} J, \tag{2}$$

$$E = \frac{V}{c} \times B + \eta J \tag{3}$$

yield the equation that describes an evolution of the magnetic field,

$$\frac{1}{c}\frac{\partial B}{\partial t} = \nabla \times (\frac{V}{c} \times B) + \frac{c\eta}{4\pi}\nabla^2 B. \tag{4}$$

$$\tag{5}$$

For collisionless conditions $\eta = 0$, the magnetic field convects with the plasma element, and never reconnects in the absence of dissipation.

The degree of collisionality is indexed by the mean-free path of plasma particles. To have magnetic reconnection, it follows that the collisional mean-free path and the collision time should be much less than the relevant plasma size and reconnection time, respectively. For the magnetospheric plasma, the mean-free path is as much as the

sun-earth distance (1AU), and the collision time is even a few days. But, magnetic reconnection does take place in less than an hour in such plasmas.

The role of resistivity becomes clear if one thinks of the following situation. Let's consider merging of two current filaments, J_1 and J_2 ($J_1 J_2 > 0$), that carry the same-directional currents (Fig.1). Such filaments attract each other by generating the poloidal magnetic field at the partner's site, and the $J \times B$ force. Approach of the current filaments condenses the magnetic field in the region between them, which generates the electric field that is centered at the X-point via Faraday's law. Nothing further happens in vacuum, and the filaments merges in a time of $\tau_A/\sqrt{2}$, where τ_A is the poloidal Alfven time. In a collisionless plasma, the electric field accelerates electrons to result in a large *return* current at the X-point, J_3 ($J_1 J_3 < 0$). This return current blocks further approach of the two current filaments J_1 and J_2, and magnetic reconnection does not proceed in the collisionless plasma. Here, the role of reducing the return current is apparent for resistivity (of any origins) in Ohm's law,

$$J_3 = E/\eta. \tag{6}$$

In a collisionless plasma, one has $\eta = 0$ and $J_3 = \infty$. Then, no reconnection. Contrarily, if resistivity is finite, then one has a small J_3. The attraction between J_1, J_2 exceeds the repulsion between J_1, J_3 and that of J_2, J_3. Thus, magnetic reconnection becomes possible. The essence here is that large (finite) resistivity limits the growth of the return current at the X-point and makes reconnection possible.

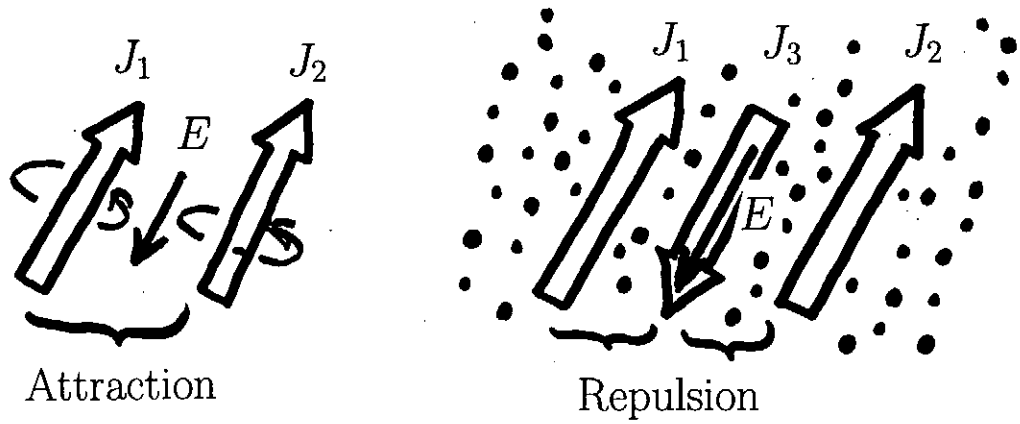

Fig.1 This sketch shows how the return current J_3 that suppresses reconnection is generated between two current filaments J_1, J_2 in a collisionless plasma (right panel). The left panel is the case for vacuum.

The theoretical candidate of resistivity was first proposed in the late 1960's, which took account of electron inertia motion in the magnetic field[1]. The physics process is that the electrons entering the reconnection region where the electric field E is present

spend a finite time τ there. This accelerates electrons to make the return current $J = ne\Delta v_z \cong (ne^2/m)E\tau$. The coefficient η in Ohm's law $J = E/\eta$ is then given by,

$$\eta = \frac{m}{ne^2\tau} \tag{7}$$

This is *electron inertia* resistivity, which gave a reasonable value of the resistivity in magnetic reconnection.

But, the (electron) inertia resistivity was rather forgotten, as *anomalous resistivity* hypothesis, whose central idea is electron scattering by waves generated by plasma-wave interactions, became so popular in the beginning of 1970. Most probable one among various kind of waves was the lower-hybrid-drift (LHD) instability and associated anomalous resistivity through the quasilinear effects[2]. However, there was a serious pitfall for this instability since the LHD instability becomes stable in high-beta plasmas[3]. The magnetospheric plasma sheet has a region of very weak magnetic field, $\beta = nT/B^2 \gg 0$. The plasma wave activities were found to be absent by the satellite measurements in the vicinity of the magnetic nulls where magnetic reconnection takes place. Therefore, one had to look for another plasma instability for anomalous resistivity.

In recent years in the fusion studies, toe role of electron inertia was revisited and used to account for rapid sawtooth oscillations and subsequent merging of magnetic islands in a tokamak[4]. This was enough to explain the rapid merging in a few Alfven times.

II. Electron Inertia Resistivity

Macro-particle simulations with collisionless conditions were performed[5]. Figure 2 shows the growth of the electric field E_y and current J_y at the X-point. These quantities are built up in a few Alfven times. It is quite remarkable that the X-point current increases with the electric field there, and that there is a proportionality relation between the electric field E and the current J, $E \propto J$. This is a direct consequence of the electron behavior; the electrons spend a *finite* time around the X-point, and consequently get *finite* acceleration. This finiteness is essential, as mentioned in Fig.1. One should note that the electron motion along the magnetic field is a key process of collisionless reconnection, which is treated only by particle methods, not by *the MHD theory.*

The direct proof of this mechanism was made by artificially prohibiting electron motion along the magnetic field[6,7]. Figure 3 shows the time history of magnetic flux contained between the flux tube (current filament) and the X-point. The solid line that decreases monotonically for $t > 1.5\tau_A$ shows constant reconnection for the normal

condition. The dashed line corresponds to the case where the parallel electron motion is prohibited. Then, magnetic reconnection is blocked, as predicted. For this case, the return current piles up at the X-point and *a plasmoid* is formed as shown in Fig.4. Magnetic flux cannot flow into the X-point steadily when the electron parallel mass diffusivity – current pump-out effect, is prohibited.

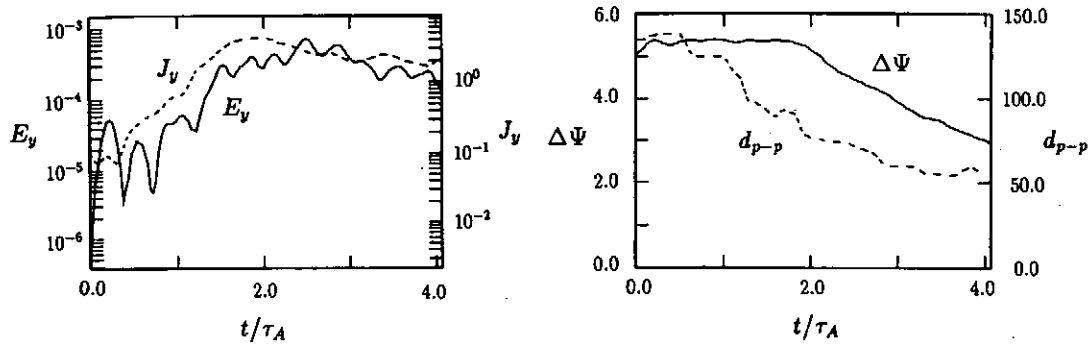

Fig.2. The time history of the reconnection electric field E_y and toroidal current J_y (upper panel), and the poloidal flux $\Delta\Psi$ contained in the flux tube.

It is interesting to know that the plasma is compressible at the X-point even under the presence of the ambient magnetic field. The divergence of the plasma flow is not identical to zero for each species, $\nabla \cdot \mathbf{V}^{(e)} \cong \cdot\mathbf{V}^{(i)} \neq 0$. (Many MHD simulations assume incompressibility.) This compressibility arises from the parallel motion of the electrons, and matching polarization drift of ions to maintain charge neutrality. Electrons are easily compressed as they escape along the magnetic field. The electron thermal motion promotes the reconnection rate.

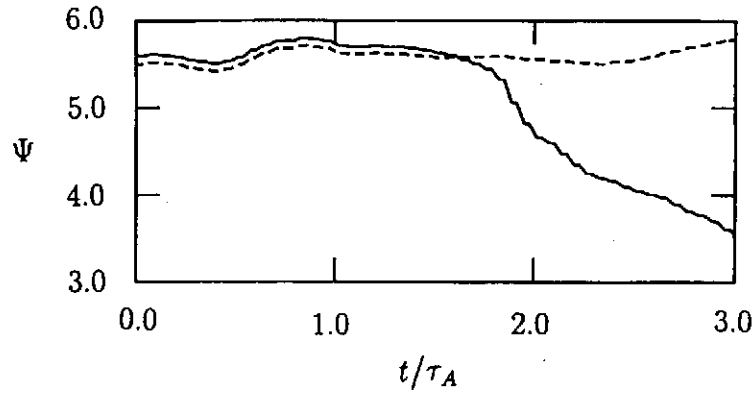

Fig.3. The reconnection rate for the normal condition (solid line), and for the case where the parallel motion of electrons along the magnetic field is prohibited (dashed line).

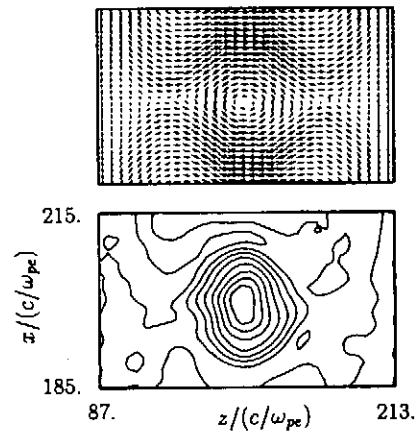

Fig.4. The poloidal and toroidal magnetic field at the X-point when parallel electron motion is suppressed.

III. Finite Larmor Radius Effect

The reconnection rate is shown as a function of ion Larmor radius in Fig.5(b). Finite Larmor radius of ions suppresses magnetic reconnection. This occurs because the charge separation electric field E_p (pointing inward to the X-line) gives the electrons in the current layer the $E_p \times B$ drift, and intensifies the X-point current. This acts negatively to reconnection, as mentioned in Fig.1. Note that only the electrons are subject to the drift; the ions are not magnetized, $\rho_i/L_B \geq 1$ where ρ_i is ion Larmor radius and L_B the current layer thickness.

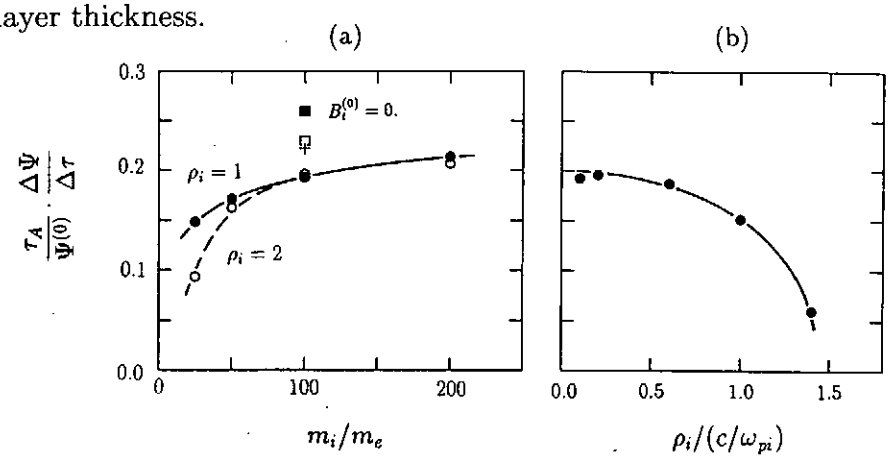

Fig.5. The dependence of the reconnection rate on (a) the ion mass, and (b) the ion Larmor radius ($m_i/m_e = 100$).

IV. Multiple Reconnection Process

It has been proven that the electron motion along the magnetic field carries away the return current generated at the X-point, and makes magnetic reconnection possible. On the other hand, the ion's role was negative; the finiteness of ion Larmor radius

suppressed the reconnection process by enhancing the return current because of the charge-separation electric field. Coupling of the electrons and ions produced the current layer[6,7] whose width was about the ion skin depth c/ω_{pi}.

One astronomical question here is concerned with a large difference between the solar flare size $10,000 - 100,000$km and the ion skin depth, 1m. This large difference in scales can be reconciled by a succession of small reconnection processes, which start from smaller scales and proceeds to larger ones. Let a be the kinetic space scale of magnetic reconnection, say ion skin depth (Fig. 6). By one reconnection, the space scale is doubled, $a + a \rightarrow 2a$. The next reconnection yields the size $4a$. After the n-th reconnection, one has the scale $2^n a = L$. Thus, $2^n = L/a \sim 7 \times 10^7$ gives the repetition of $n \sim 26$ times. The whole reconnection time is given by a sum of all these reconnection processes,

$$\begin{aligned} \tau_A &= \frac{1}{v_A}[\frac{L}{2} + \frac{L}{4} + ... + \frac{L}{2^n}] \\ &= \frac{L}{2v_A}\sum_{i=1}^{n}\left(\frac{1}{2}\right)^{i-1} \cong \frac{L}{v_A}. \end{aligned} \tag{8}$$

The global reconnection time is exactly what we expect for a single reconnection of the space scale L.

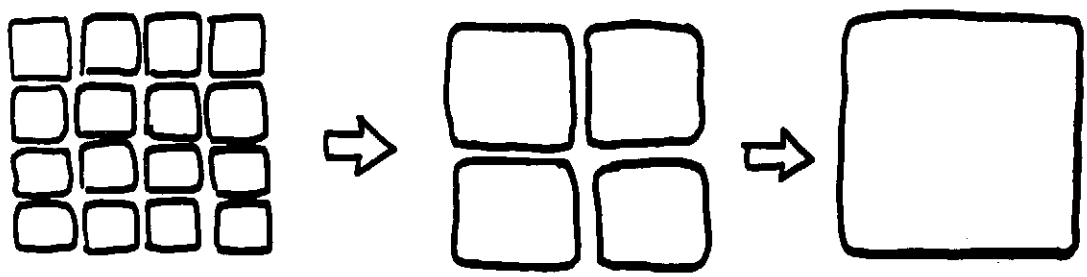

Fig.6. A sketch showing the multiple reconnection processes.

References

1. T.W. Speiser, *Planet.Space Sci., 18*, 613 (1970).
2. R.C.Davidson and N.T.Gladd, *Phys.Fluids, 18*, 1327 (1975).
3. J.D.Huba, N.T.Gladd and K.Papadopoulos, *J.Geophys.Res., 83*, 5217 (1978).
4. J.A. Wesson, *Nucl.Fusion, 30*, 2545 (1990).
5. M.Tanaka, J.Comput.Phys., 107, 124 (1993).
6. M.Tanaka, Phys.Plasmas, 2, 2920 (1995).
7. M.Tanaka, Phys.Plasmas, 3, 4010 (1996).

EVIDENCE OF MAGNETIC RECONNECTION IN SOLAR FLARES AND A UNIFIED MODEL OF FLARES

KAZUNARI SHIBATA
Kwasan and Hida Observatories
Kyoto University
Yamashina, Kyoto 607-8471, Japan

Abstract: The solar X-ray observing satellite Yohkoh has discovered various new dynamic features in solar flares and corona, e.g., cusp-shaped flare loops, above-the-loop-top hard X-ray sources, X-ray plasmoid ejections from impulsive flares, transient brightenings (spatially resolved microflares), X-ray jets, large scale arcade formation associated with filament eruption or coronal mass ejections, and so on. It has soon become clear that many of these features are closely related to magnetic reconnection. We can now say that Yohkoh established (at least phenomenologically) the magnetic reconnection model of flares. In this paper, we review various evidence of magnetic reconnection in solar flares and corona, and present unified model of flares on the basis of these new Yohkoh observations.

1. INTRODUCTION

A few years ago, Akasofu (1995) published a nice popular science book entitled "Introduction to Aurora" written in Japanese. In this book, he wrote "*Solar physicists have long tried to prove an assumption that flares are caused by magnetic reconnection, but not yet succeeded. They forgot that magnetic reconnection was simply an assumption*" ! This statement is a big challenge to solar physicists. Though this might have been partly true before launch of Yohkoh (Ogawara et al. 1991), the situation has been dramatically changed by Yohkoh observations of solar flares.

Yohkoh is a solar X-ray observing satellite launched on Aug. 30, 1991, under international collaboration between Japan, US, and UK. Yohkoh carries two X-ray telescopes, soft X-ray telescope (SXT) (Tsuneta et al. 1991) observing $\sim$ 1 keV soft X-rays emitted from 2 – 20 MK thermal plasmas, and hard X-ray telescope (HXT) (Kosugi et al. 1991), for observations of

10 – 100 keV hard X-rays emitted from nonthermal electrons and superhot plasmas. Yohkoh X-ray observations discovered a lot of evidence of magnetic reconnection in solar flares, e.g., cusps, plasmoids, loop top hard X-ray sources, etc. Yohkoh discovered also various new dynamic phenomena in the corona, such as X-ray jets, microflares, large scale arcade formation, etc. It has soon become clear that these new phenomena are also closely related to magnetic reconnection (e.g., Tsuneta et al. 1992a,b, Shibata et al. 1992b, 1995, Masuda et al. 1994, Shibata 1996, Kosugi and Shibata 1997).

The purpose of this paper is to review these new observations on evidence of magnetic reconnection to convince Akasofu that magnetic reconnection is not an assumption but physical process actually occurring in solar flares. Furthermore, on the basis of these new observations, we propose that various flares, including microflares, impulsive flares, LDE (long duration event) flares, and large scale arcade formation associated with coronal mass ejections, are all explained by a unified model, which we call the *plasmoid-induced-reconnection model* (Shibata 1996, 1997, 1998).

2. FLARES AND PLASMOIDS

2.1. LDE FLARES VS IMPULSIVE FLARES

Solar observers have long thought that there are two types of flares, e.g., long duration event (LDE) flares and impulsive flares. LDE flares typically last more than 1 hour, while impulsive flares are short lived, less than 1 hour. The latter is characterized by the impulsive hard X-ray emission whereas the former shows more softer X-ray spectrum.

Yohkoh soft X-ray telescope (SXT) has discovered that many LDE flares show *cusp-shaped loop* structures (Tsuneta et al. 1992a, Hanaoka 1994, Tsuneta 1996, Forbes and Acton 1996; Fig. 1a), which are quite similar to magnetic field cofiguration predicted by the classical magnetic reconnection model (Carmichael-Sturrock- Hirayama-Kopp-Pneuman model, hereafter called CSHKP model). There are a number of evidence of magnetic reconnection in these LDE flares (Tsuneta 1996): (1) The temperature is systematically higher in outer loops (as predicted by reconnection model; e.g., see Hori et al. 1997, Yokoyama and Shibata 1997, 1998). (2) The cusp-shaped loops apparently grow with time, i.e., the height of loops and the separation of two footpoints of loops increase with time. (3) The energy release rate and other physical quantities are consistent with the prediction by magnetic reconnection model. (4) The plasmoid ejections are often seen in the rise phase of LDE flares (e.g., Hudson 1994).

From these observations and analyses, it was established that LDE flares

are produced by the CSHKP-type magnetic reconnection mechanism. [1] The same physical process can also be applied to *large scale arcade formation* associated with filament eruption or CMEs (e.g., Tsuneta et al. 1992b, Hiei et al. 1994, Hanaoka et al. 1994, McAllister et al. 1996).

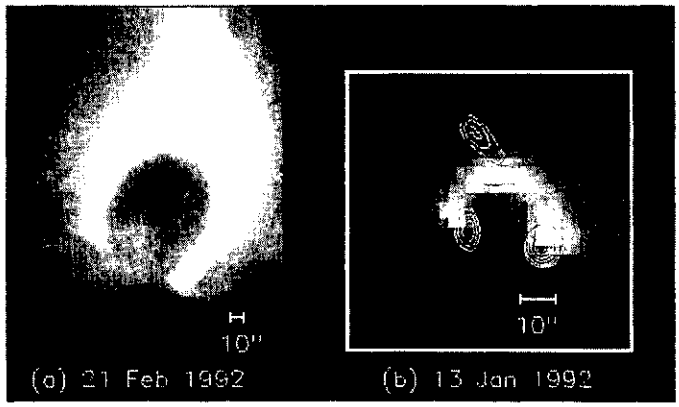

Figure 1. (a) LDE flare on 21 Feb. 1992 observed with SXT (Tsuneta et al. 1992a). (b) Impulsive flare on 13 Jan. 1992 which shows a loop top hard X-ray source above soft X-ray loop (Masuda et al. 1994). Contours of hard X-ray (33 – 53 keV) intensity distribution are overlaid on the soft X-ray ($\sim$ 1 keV) image.

The SXT images of impulsive flares, however, show only *simple loop* structures, as already known from Skylab observations. Hence it was first thought that these impulsive flares might be created by the mechanism different from that for LDE flares, and the magnetic reconnection model was questioned.

It was Masuda (1994) who changed this situation dramatically. He carefully coaligned the SXT and the HXT images of some impulsive compact loop flares observed at the limb, and showed that there is an impulsive HXR source *above* the SXR loop, in addition to the footpoint impulsive

[1] Here, the "CSHKP-type magnetic reconnection mechanism" simply means the *reconnection occurring in a helmet-streamer (or inverted Y type) field configuration* in which a vertical current sheet is situated above a closed loop. We should keep in mind that there was no agreement on the formation process of this geometry in Carmichael (1964), Sturrock (1966), Hirayama (1974), and Kopp and Pneuman (1976). For example, Hirayama (1974) considered that MHD instability (causing filament eruption) is a key to form this geometry, while Kopp and Pneuman (1976) thought that the solar wind opens the closed field to form a current sheet. Only common point in these *classical models* is a helmet-streamer (or inverted Y type cusp-shaped) field configuration. I take this standpoint in this review for a definition of the "CSHKP" model. This model has been extended by many authors (e.g., some of such extended models are Cargill and Priest 1983, Cliver 1983, Forbes and Priest 1984, Martens and Kuin 1990, Moore and Roumeliotis 1992). As a historical remark, the term "CSHKP model" was first introduced by Sturrock (1992), and has been often used in solar physics community.

double hard X-ray (HXR) sources (Masuda et al. 1994; Fig. 1b). Since the impulsive HXR sources are produced by high energy electrons, which are closely related to the main energy release mechansim, this means that *the main energy release occurred above (outside) the soft X-ray (SXR) loop.* This means also that the flare models invoking the energy release mechanism inside the SXR loops (e.g., Alfven and Carlqvist 1967, Spicer 1977, Uchida and Shibata 1988) must now be discarded at least for these impulsive compact loop flares.

What is the energy release mechanism in these compact loop flares ? Masuda et al. (1994) postulated that the basic magnetic field configuration is similar to that of LDE flares and that the high speed jet produced by the reconnection collides with the top of the reconnected loop to produce very hot region as well as high energy electrons. (See Aschwanden et al. 1996 for independent observational evidence for acceleration site of high energy electrons high above the SXR loops.)

2.2. X-RAY PLASMOID EJECTIONS FROM IMPULSIVE FLARES

If the impulsive compact loop flares occur as a result of reconnection in a geometry similar to that for LDE flares, plasmoid ejections would be observed high above the loop top HXR source (Fig. 2). Shibata et al. (1995) searched for such plasmoid ejections using SXT images in 8 impulsive compact loop flares observed at the limb, and indeed found that *all these flares were associated with X-ray plasma (or plasmoid) ejections.* The apparent velocity of these ejections are 50 – 400 km/s, and their height ranges are $4 - 10 \times 10^4$ km. Interestingly, flares with HXR source well above the loop top show systematically higher velocity. It is also interesting that there is a positive correlation between the plasmoid velocity ($V_{plasmoid}$) and the apparent rise velocity of the SXR loop (V_{loop}):

$$V_{plasmoid} \simeq (8 - 20) \times V_{loop}. \quad (1)$$

The SXR intensity of the ejections is very low, typically $10^{-4} - 10^{-2}$ of the bright SXR loop. The shape of these plasma ejections is loop-like, blob-like, or jet-like, which are somewhat similar to the shape of CMEs. In many cases, strong acceleration of plasmoids occur during the impulsive phase (Ohyama and Shibata 1997, 1998; Fig. 4), and the temporal relation between height of the ejections and the HXR intensity is very similar to that between CME height and the SXR intensity of an associated flare.

Ohyama and Shibata (1997, 1998) and Tsuneta (1997) analyzed the temperature distribution of plasmoids, flare loops, and ambient structure, and have revealed that the temperature of plasmoids is $\sim 6-13$ MK, slightly less than that of flare loops, and the overall temperature distribution is consistent with that predicted by the reconnection model.

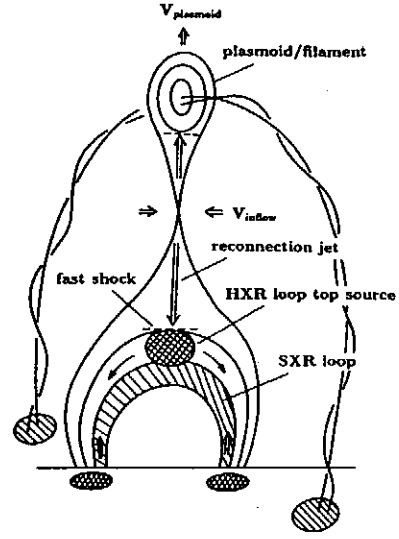

Figure 2. A unified model of flares: *plasmoid-induced-reconnection model* (Shibata et al. 1995, Shibata 1996, 1997).

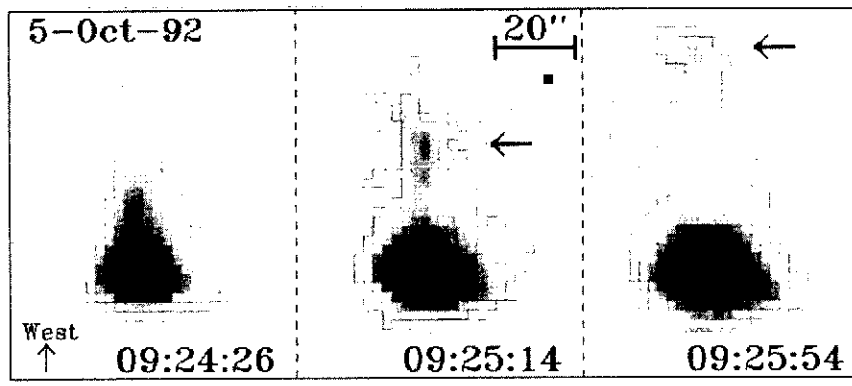

Figure 3. X-ray plasmoid ejections from an impulsive compact loop flare observed with Yohkoh SXT on 5 Oct. 1992 (Ohyama and Shibata 1998). The velocity of the ejections is 200 – 450 km/s.

Ohyama and Shibata (1997, 1998) showed that the kinetic energy of plasmoids is much smaller than that of the total flare energy. This means that the kinetic energy of the plasmoid ejection cannot be the source of flare energy. Instead, the plasmoid ejection could play a role to trigger the main energy release in impulsive phase, since in some events observed in the preflare phase, the plasmoid starts to be ejected (at 10 km/s) well before the impulsive phase (Ohyama and Shibata 1997; Fig. 4).

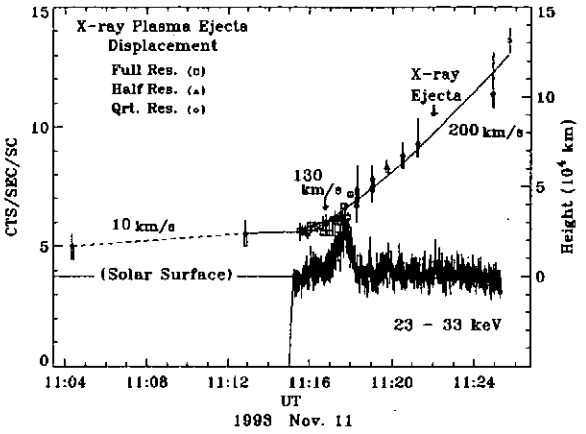

Figure 4. Temporal variations of the height of an X-ray plasmoid and the hard X-ray intensity in an impulsive flare on 11 Nov. 1993 observed by Yohkoh SXT and HXT (from Ohyama and Shibata 1997).

2.3. RECONNECTION MODEL: PLASMOID-INDUCED-RECONNECTION MODEL

On the basis of above observations, Shibata (1996, 1997) proposed the *plasmoid-induced-reconnection model*, by extending the classical CSHKP model. In this model, the plasmoid does not open magnetic field to create current sheet, but instead the plasmoid *is already situated in the current sheet.* In other words, the plasmoid (= flux rope in 3D view) inhibit the reconnection at the current sheet, as in Uchida et al. (1998)'s model where they considered that dark filament ($\sim$ flux rope) inhibits collapse of current sheet. Hence if the plasmoid starts to move, the anti-parallel field lines begin to contact and reconnect. Once the reconnection starts, the released energy help accelerating the plasmoid, leading to faster inflow into the current sheet (i.e., faster reconnection), and the further released energy again accelerate the plasmoid, and so on. This process is a kind of global nonlinear instability (Ugai 1986). In this sense, the plasmoid ejections plays only a role of triggering fast reconnection.

Let us consider the situation that a plasmoid suddenly rises at velocity $V_{plasmoid}$. [2] Since the plasma density does not change much during the eruption process, the plasma inflow with a velocity

$$V_{inflow} \sim V_{plasmoid} L_{plasmoid} / L_{inflow} \qquad (2)$$

[2]In this model, on the basis of observations, we *assume* that the plasmoid is already created before the flare, and is suddenly accelerated by some mechanism. Magnetic reconnection could also play a role to form a plasmoid and accelerate it in such preflare phase as noted by Ohyama and Shibata (1997).

must develop toward the X-point to compensate the mass ejected by the plasmoid (e.g., Ugai 1986, Magara et al. 1997), where $L_{plasmoid}$ and $L_{inflow}(> L_{plasmoid})$ are the typical sizes of the plasmoid and the inflow. We consider that the impulsive phase correspond to the phase when $L_{inflow} \sim L_{plasmoid}$, i.e.,

$$V_{inflow} \sim V_{plasmoid} \sim 50 - 400 \text{ km/s}. \tag{3}$$

Since the reconnection rate is determined by the inflow speed, the ultimate origin of fast reconnection in this model is the fast ejection of the plasmoid. (Of course, the force to compress the current sheet is magnetic pressure around the initial current sheet containing plasmoid.) The equation (2) predicts

$$V_{plasmoid} \propto V_{loop}, \tag{4}$$

since $V_{loop} \sim (B_{inflow}/B_{loop})V_{inflow}$ from conservation of magnetic flux. This nicely explains the observed relation, eq. (1). After the impulsive phase, we expect that L_{inflow} becomes larger than $L_{plasmoid}$ because the distance between the plasmoid and the X-point increases, and hence the inflow speed V_{inflow} would decrease much, leading to slow reconnection which corresponds to the decay or late phase.

In this model, the electric field at the X-point (and surrounding region) becomes $E \sim V_{inflow}B/c$ and is largest during the impulsive phase. Hence, it naturally explains acceleration of higher energy electrons in impulsive phase than in decay phase.

The magnetic reconnection theory predicts two oppositely directed high speed jets from the reconnection point at Alfven speed,

$$V_{jet} \sim V_A \simeq 2000\Big(\frac{B}{100\text{G}}\Big)\Big(\frac{n_e}{10^{10}\text{cm}^{-3}}\Big)^{-1/2} \text{ km/s}, \tag{5}$$

where B is the magnetic flux density and n_e is the electron density (= ion density). The downward jet collides with the top of the SXR loop, producing MHD fast shock, superhot plasmas and/or high energy electrons at the loop top, as observed in the HXR images. The temperature just behind the fast shock becomes

$$T_{loop-top} \sim m_i {V_{jet}}^2/(6k) \sim$$

$$2 \times 10^8 \Big(\frac{B}{100\text{G}}\Big)^2\Big(\frac{n_e}{10^{10}\text{cm}^{-3}}\Big)^{-1} \text{ K}, \tag{6}$$

where m_i is the hydrogen ion mass and k is the Boltzmann constant. This explains the observationally estimated temperature of the loop top HXR source (Masuda 1994). We would expect similar physical process for the upward directed jet (see Fig. 2). Indeed we find an SXR bright point during

the impulsive phase somewhat far from the SXR loop. This bright point seems to be located at the footpoint of the erupting loop.

The magnetic energy stored around the current sheet and the plasmoid is suddenly released through reconnection into kinetic and thermal/nonthermal energies after the plasmoid is ejected. The magnetic energy release rate at the current sheet (with the length of $L_{inflow} \sim L_{plamoid} \simeq 2 \times 10^4$ km) is estimated to be

$$dW/dt = 2 \times L_{plasmoid}^2 B^2 V_{inflow}/4\pi$$

$$\sim 4 \times 10^{28} \left(\frac{V_{inflow}}{100 \text{ km/s}}\right)\left(\frac{B}{100 \text{ G}}\right)^2\left(\frac{L_{plasmoid}}{2 \times 10^9 \text{ cm}}\right)^2 \text{ erg/s}. \quad (7)$$

This is comparable with the energy release rate during the impulisve phase, $4 - 100 \times 10^{27}$ erg/s, estimated from the HXR data, assuming the lower cutoff energy as 20 keV (Masuda 1994).

The reason why the HXR loop top source is not bright in SXR is that the evaporation flow has not yet reached the colliding point and hence the electron density (and so the emission measure) is low. The key physical parameter discriminating impulsive flares and LDE flares (or impulsive phase and gradual phase) is the velocity of the inflow, V_{inflow}. If V_{inflow} is large, the reconnection is fast, so that the reconnected field lines accumulate very fast and hence the MHD fast shock (i.e., HXR loop top source) is created well above SXR loop which is filled with evaporated plasmas. On the other hand, if V_{inflow} is small, the reconnection is slow and hence the fast shock is produced at the SXR loop.

3. MICROFLARES AND JETS

3.1. TRANSIENT BRIGHTENINGS (MICROFLARES)

Shimizu et al. (1992) analyzed active region transient brightenings (ARTBs) in detail, and found that these correspond to soft X-ray counter part of hard X-ray microflares (Lin et al. 1984). The total thermal energy content of ARTBs is $10^{25} - 10^{29}$ erg, their lifetime ranges from 1 to 10 min, their length is $(0.5 - 4) \times 10^4$ km, and the temperature is about $6 - 8$ MK. According to recent analysis of Shimizu (1996) on the comparison of Yohkoh SXT images of ARTBs with LaParma ground based data, some ARTBs indeed occur in association with emergence of tiny magnetic bipole, suggesting the reconnection between emerging flux and pre-existing field. The occurrence frequency of these ARTBs (SXR microflares) decreases with increasing their total energy and shows power-law distribution; $dN/dE \propto E^{-\alpha}$, where dN is the number of ARTBs per day in the energy range between $E + dE$ and E, and $\alpha \simeq 1.5 - 1.6$ (Shimizu 1995). This is nearly the same as

that of HXR microflares and larger flares. Since the index α is less than 2, the SXR microflares alone cannot explain coronal heating. The universal power-law distribution seems to suggest the universal phyiscal origin of both microflares and large scale flares (Watanabe 1994).

3.2. X-RAY JETS

X-ray jets are defined as transitory X-ray enhancements with apparent collimated motion (Shibata et al. 1992b, 1994, 1996, Strong et al. 1992, Shimojo et al. 1996; see Fig. 5). Almost all jets are associated with microflares or subflares, and the length ranges from 1000 to 4×10^5 km. Their apparent velocity is 10 – 1000 km/s. The temperature of X-ray jets is about 4 – 6 MK, which is comparable to those of the footpoint microflares. The electron density ragnes from 3×10^8 to 5×10^9 cm^{-3} and the kinetic energy was estimated to be $10^{25} - 10^{29}$ erg.

There are a number of evidence of magnetic reconnection in X-ray jets.

(1) Morphology: Many jets show constant or converging shape (Shimojo et al. 1996), implying the magnetic field configuration with a neutral point near the footpoint of a jet as shown in Figure 6. In some jets (27 percent), a gap is seen between footpoints of jets and brightest part of the footpoint flares. This is also nicely explained by the reconnection model (Shibata et al. 1996), since the reconnection creates two hot reconnected field lines (a loop and a jet) with a gap between them. Shibata et al. (1996) noted that there are two types of interaction between emerging flux and overlying coronal field; one is the *anemone* type, in which emerging flux appears in coronal hole and a jet is ejected vertically, and the other is the *two-sided-loop* type, which occurs when the emerging flux appears in closed loop region, producing two-sided loops (or jets). The morphology of these types suggests the reconnection between emerging flux and overlying coronal field and resulting formation of jets (or loop brightenings).

(2) Magnetic field: Shimojo, Shibata, and Harvey (1998) have revealed that the magnetic field properties of the footpoint of jets are mainly mixed polarities or satellite spots. This gives a direct evidence of the presence of neutral points (or current sheets) near the footpoint of jets.

(3) Hα surges: Often Hα surges are associated with X-ray jets (e.g., Shibata et al. 1992b, Canfield et al. 1996), though there are also negative cases (e.g., Schmieder et al. 1995). From observations of Hα surges associated with X-ray jets, Canfield et al. (1996) found several new evidence of reconnection.

(4) Type III bursts: Some X-ray jets are associated with type III bursts (Auras et al. 1995, Kundu et al. 1995). This indicates that high energy electrons are accelerated in these small scale microflare/jet events, suggest-

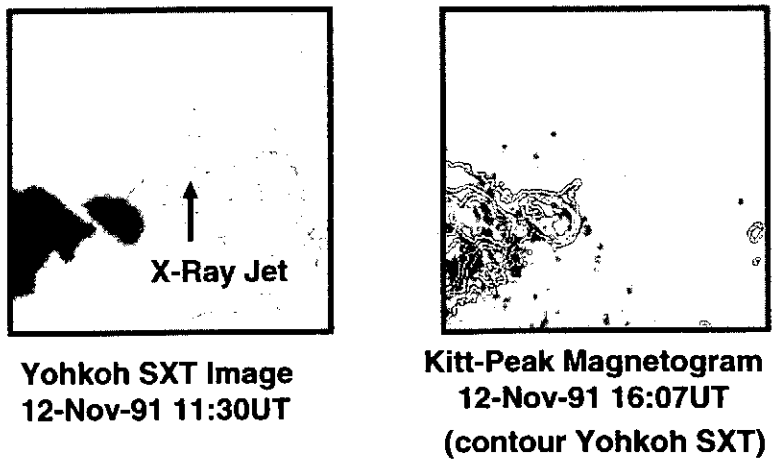

Figure 5. Left: An X-ray jet observed with Yohkoh SXT on 12 Nov. 1991 (Shibata et al. 1992b). Right: NSO/Kitt Peak magnetogram for the same region with overlay of contours of soft X-ray intensity distribution. Note mixed polarities at the footpoint of the jet.

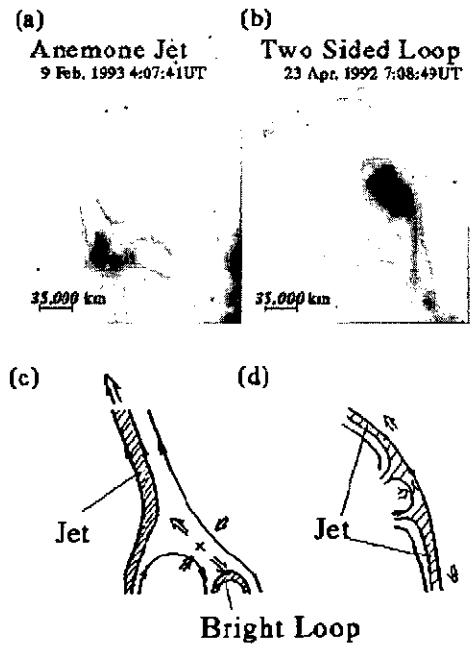

Figure 6. Two types of interaction between emerging flux and overlying coronal fields (from Yokoyama and Shibata 1995).

ing that the same physical process as that of larger flares (i.e., magnetic reconnection) might be occurring in these events.

3.3. MAGNETIC RECONNECTION MODEL: EMERGING FLUX MODEL

Yokoyama and Shibata (1995, 1996) developed magnetic reconnection model of X-ray jets using 2.5D MHD numerical simulations (Fig. 7). In their model, magnetic reconnection occurs in the current sheet between emerging flux and overyling coronal field as in the classical emerging flux model (Heyvaerts et al. 1977, Forbes and Priest 1984, Shibata et al. 1992a). The basic driving force is magnetic buoyancy, though the reconnection rate is not uniquely determined by the rise velocity of emerging flux but affected by the local plasma condition such as the resistivity and dynamics (Ugai 1986, Scholer 1989, Yokoyama and Shibata 1994). Yokoyama and Shibata (1995, 1996) found following interesting features in their simulation results based on the emerging flux model.

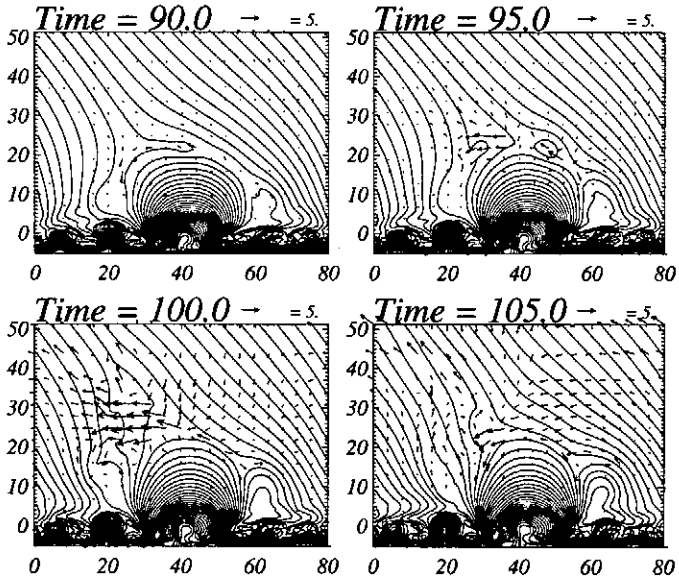

Figure 7. Emerging flux reconnection model of Yokoyama and Shibata (1995, 1996). Note that plasmoids (magnetic islands) are repeatedly created in the current sheet and are ejected upward.

The reconnection starts with the formation of magnetic islands (i.e., plasmoids). (In three dimension, they are seen as helically twisted flux rope.) These islands coalesce with each other and finally are ejected out of the current sheet. After the ejection of the biggest island, the largest energy release occur. The reconnection jets from the X-point soon collides with the ambient field to form fast shocks. The global jets are emanating from the high pressure region just behind the fast shock, and propagate along the reconnected field line. This suggests that *observed X-ray jets are*

not the reconnection jet itself, but hot jets accelerated by the enhanced gas pressure behind the fast shock.

The emission measure of the X-point is the smallest at the X-point, since the volume of the X-point is very small (Yokoyama and Shibata 1996). Thus the X-point is not bright and hence is not easy to be detected. This may be the reason why we observe a gap between a jet and the brightest part of a footpoint flare. In relation to this, Innes et al. (1997) recently reported interesting observations of bi-directional plasma jets using SOHO/SUMER. They interpreted that these jets corresponded to reconnection jets because the intensity between two jets was largest and hence (they thought) the brightest region corresponded to X-point. However, as discussed above, the X-point cannot be a bright region, and hence it is likely that Innes et al. (1997) observed different phenomena, e.g., bi-directional jets ejected from high pressure region just behind the fast shock.

Yokoyama and Shibata found that not only hot jets ($T > 10^6$ K) but also cool jets ($T \sim 10^4 - 10^5$ K) are accelerated by the J x B force in association with reconnection. The cool jets might correspond to Hα surges associated with X-ray jets (Shibata et al. 1992b, Canfield et al. 1996, Okubo et al. 1996). These cool jets start to be accelerated just before hot jets are formed, and are ejected originally as plasmoids (or helically twisted flux rope in three dimension) and form an elongated structure after the plasmoids collides and reconnects with ambient fields. The initial phase of the ejection of both cool and hot jets are seen as *whip-like motion*. In main phase, the cool jets are situated just side of the hot jets with nearly the same orientation. These features are indeed observed in several Hα surges associated with X-ray jets (Canfield et al. 1996).

Okubo et al. (1996) extended Yokoyama and Shibata (1996)'s simulations to the case in which twisted or sheared magnetic flux emerges to reconnect with overlying field. They found that as a result of reconnection between twisted (sheared) field and untwisted field, shear Alfven waves are generated and propagate along reconnected flux tube. Since these Alfven waves have large amplitude, they excite large transversal motion (or spinning motion) of jets and exert nonlinear magnetic pressure force to cool/hot jets to cause further acceleration of them, as originally suggested by Shibata and Uchida (1986). Canfield et al. (1996) found that all Hα surges (9 events) in his observations showed spinning motion at a few 10 km/s (consistent with prediction from numerical simulation) whose direction is also consistent with the direction of unwinding motion of helically twisted flux tubes observed in the same active region 7260. (Schmieder et al. 1995 and Kurokawa et al. 1987 observed similar spinning motion of surges. See also related numerical simulation by Karpen et al. 1998 on the reconnection between sheared and unsheared fields and resulting formation of cool jets.)

4. Summary: Unified View and Unified Model

As we have seen above, Yohkoh SXT/HXT observations have revealed various evidence of magnetic reconnection, especially common occurrence of X-ray mass ejections (plasmoids and/or jets), in LDE flares, impulsive flares, and microflares. These are summarized in Table 1.

Table I Unified View of Various "Flares"

"flares"	mass ejections (cool)	mass ejections (hot)
global restructuring (giant arcade)	Hα filament eruptions	CMEs
LDE flares	Hα filament eruptions	X-ray plasmoid ejections/CMEs
impulsive flares	Hα sprays	X-ray plasmoid ejections
transient brightenings (microflares)	Hα surges	X-ray jets

On the basis of this unified view, Shibata (1996, 1997, 1998) proposed a unified model, *plasmoid-induced-reconnection model*, to explain not only LDE flres and impulsive flares but also microflares and X-ray jets.

One may argue, however, that the shape of X-ray jets and Hα surges (i.e., collimated jet-like structure) is very different from that of plasmoids. How can we relate these jets with plasmoids whose shapes are blob-like (or loop-like in three dimensional space) ? The answer to this question is already given by numerical simulations of Yokoyama and Shibata (1995, 1996; Fig. 6); a blob-like plasmoid ejected from the current sheet soon collides with the ambient fields, and finally disappears (Fig. 8). The mass contained in the plasmoid is transferred into the reconnected open flux tube and forms a collimated jet along the tube. In three dimensional space, this process would be observed as follows: an erupting helical loop (a plasmoid ejected from the current sheet) collides with an ambient loop to induce reconnection seen as a loop-loop interaction. Through this reconnection, magnetic twist (helicity) in the erupting loop is injected into the untwisted loop, resulting in the unwinding motion of the erupting loop/jet (Shibata and Uchida 1986), which may correspond to the spinning motion observed in some Hα surges (Canfield et al. 1996, Schmieder et al. 1995). This also explains why we usually do not observe plasmoid-like (or loop-like) mass

ejections in smaller flares (e.g., microflares). In smaller flares, the current sheet is short, so that a plasmoid soon collides with an ambient field to reconnect with it and disappear. Hence the lifetime of the plasmoid (or loop-like) ejection is very short, of order of $t \sim L/V_{plasmoid} \sim 10 - 100$ sec. It would be interesting to test this scenario using high spatial and temporal resolution observations with Doppler shift measurement in a future mission such as Solar B.

Ground based observations suggest that emerging flux plays an important role in driving flares (e.g., Kurokawa 1987, Zhang et al 1998, Nishio et al. 1997, Hanaoka 1997). For example, a famous X-class impulsive flare, the 15 Nov 1992 flare (e.g., Sakao et al. 1992), was driven by a moving satellite spot (or emerging flux). Even the 21 Feb 1992 LDE flare (e.g., Tsuneta 1996), and a homologous to it on 24 Feb 1992 (Morita et al. 1998) seem to be driven by growing flux (or emerging flux) (Zhang et al. 1998). Nevertheless, these flares clearly show filament or plasmoid ejections as well as the morphology predicted by the CSHKP model. Thus there is a need to unify the CSHKP and the emerging flux models. Such a unification is indeed possible in our *plasmoid-induced-reconnection model* as shown in Fig. 8.

Finally, it should be noted that the basic physics of reconnection has not yet been solved. In particular, the ion gyro radius and collisionless skin depth (c/ω_{pe}) in the solar corona ($\approx 10 - 100$ cm), which is a possible minimum thickness of current sheet, is much smaller than the flare size ($\approx$ 10000 km). The gap between these microscopic and macroscopic scales is huge, so that it is difficult to connect microscopic plasma process (such as anomalous resistivity and collisionless reconnection) and macroscopic dynamics. The turbulent (or fractal) current sheet could be a key to connect these vastly different spatial scales (e.g., Tajima and Shibata 1997, Pustlnik 1998).

ACKNOWLEDGMENTS

The author would like to thank M. Ohyama, T. Kudoh, M. Shimojo, T. Yokoyama and other Yohkoh colleagues for their various help and interesting discussion.

References

Acshwanden, M. J., Hudson, H. S., Kosugi, T., and Schwartz, R. A., 1996, ApJ, 464, 985.
Akasofu, S., 1995, *Introduction to Aurora* (in Japanese), Chuou-Kouron-Sha (Chu-ko Shinsho 1273).
Alfven, H., and Carlqvist, P., 1967, Solar Phys. 1, 220.
Aurass, H., Klein, K. -L., and Martens, P. C. H., 1995, Solar Phys. Lett., 155, 203.
Canfield, R. C., Reardon, K. P., Leka, K. D., et al., 1996, ApJ, 464, 1016.

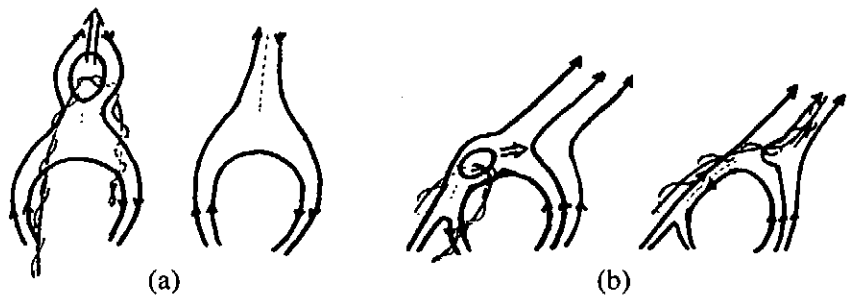

Figure 8. Unification of the CSHKP model (a) and the emerging flux model (b) by the *plasmoid-induced-reconnection* model (Shibata 1997, 1998). Note that a plasmoid (a magnetic island or a helically twisted flux rope) collides and reconnects with the ambient magnetic field to disappear in a short time scale (10 – 100 sec) in microflares.

Cargill, P., and Priest, E. R., 1983, ApJ, 266, 383
Carmichael, H., 1964, in *Proc. of AAS-NASA Symp. on the Physics of Solar Flares*, W. N. Hess (ed.), NASA-SP 50, p. 451.
Cliver, E. W., 1983, Solar Phys., 84, 347.
Forbes, T., and Acton, L., 1996, ApJ, 459, 330.
Forbes, T. G., and Priest, E. R., 1984, Solar Phys., 94, 315.
Hanaoka, Y., 1994, in *Proc. Kofu meeting*, eds. S. Enome, and T. Hirayama, Nobeyama Radio Observatory , p. 181.
Hanaoka, Y., et al., 1994, PASJ, 46, 205.
Hanaoka, Y., 1997, Solar Phys., 173, 319.
Heyvaerts, J., Priest, E. R., and Rust, D. M., 1977, ApJ, 216, 123.
Hiei, E., Hundhausen, A. J., and Sime, D. G., 1993, GRL, 20, 2785.
Hirayama, T., 1974, Solar Phys., 34, 323.
Hori, K., Yokoyama, T., Kosugi, T., and Shibata, K., 1997, ApJ, 489, 426.
Hudson, H. S., 1994, in *Proc. Kofu meeting*, eds. S. Enome, and T. Hirayama, Nobeyama Radio Observatory , p. 1.
Innes, D. E., et al., 1997, Nature, 386, 811.
Kopp, R. A., and Pneuman, G. W., 1976, Solar Phys., 50, 85.
Karpen, J. T., Antiochos, S. K., and DeVore, C. R., 1998, ApJ, 495, 491.
Kosugi, T., et al., 1991, Solar Phys., 136, 17.
Kosugi, T., and Shibata, K., 1997, in *Proc. Magnetic Storms*, Geophysical Monograph 98, (Washington, American Geophysical Union), p. 21.
Kundu, M. R., Raulin, J. P., Nitta, N., et al., 1995, ApJ, 447, L135.
Kurokawa, H., 1987, Space Sci. Rev., 51, 49.
Kurokawa, H., Hanaoka, Y., Shibata, K., and Uchida, Y., 1987, Solar Phys., 108 , 251.
Lin, R. P., et al., 1984, ApJ, 283, 421.
Magara, T., Shibata, K., and Yokoyama, T., 1997, ApJ, 487, 437.
Martens, P. C. H., and Kuin, N. P. M., 1989, Solar Phys., 122, 263.
Masuda, S., 1994, Ph. D. Thesis, U. Tokyo.
Masuda, S., Kosugi, T., Hara, H., Tsuneta, S., and Ogawara, Y., 1994, Nature, 371, 495.
McAllister, A. H., Kurokawa, H., Shibata, K., and Nitta, N., 1996, Solar Phys., 169, 123.
Moore, R. L., and Roumeliotis, G., 1992, in *Lecture Note in Physics, No. 399, Eruptive Flares*, ed. Z. Svestka, B. V. Jackson, and M. E. Machado (New York, Springer), 69.
Morita, S., Uchida, Y., et al., 1998, in *Proc. Observational Plasma Astrophysics*, Watan-

abe, T., Kosugi, T., and Sterling, A. C. (eds), Kluwer, p. 327.
Nishio, M., et al., 1997, ApJ, 489, 976.
Ogawara, Y., et al., 1991, Solar Phys., 136, 1.
Ohyama, M., and Shibata, K., 1997, PASJ, 49, 249.
Ohyama, M., and Shibata, K., 1998, ApJ, 499, 934.
Okubo, A. et al., 1996, in *Proc. Observations of Magnetic Reconnection in the Solar Atmosphere*, Bentley, R. and Mariska, J. T. (eds.), PASP conf. vol. 111, p. 39.
Pustl'nik, L., 1998, in these proceedings.
Sakao, T., et al., 1992, PASJ, 44, L83.
Schmieder, B., Shibata, K., et al., 1995, Solar Phys., 156, 245.
Scholer, M., 1989, JGR, 94, 8805.
Shibata, K., and Uchida, Y., 1986, Solar Phys., 103, 299.
Shibata, K., Nozawa, S., and Matsumoto, R., 1992a, PASJ, 44, 265.
Shibata, K., Ishido, Y., Acton, L., et al., 1992b, PASJ, 44, L173.
Shibata, K., Nitta, N., Strong, K. T., et al., 1994, ApJ, 431, L51.
Shibata, K., Masuda, S., Shimojo, M., et al., 1995, ApJ, 451, L83.
Shibata, K., Yokoyama, T., and Shimojo, M., 1996, J. Geomag. Geoelectr., 48, 19.
Shibata, K., 1996, Adv. Space Res., 17, (4/5)9.
Shibata, K., 1997, in *Proc. 5-th SOHO workshop*, (ESA SP-404) p. 103.
Shibata, K., 1998, in *Proc. Observational Plasma Astrophysics*, Watanabe, T., Kosugi, T., and Sterling, A. C. (eds), Kluwer, p. 187.
Shimizu, T., Tsuneta, S., Acton, L. W., Lemen, J. R., Uchida, Y., 1992, PASJ, 44, L147.
Shimizu, T., 1995, PASJ, 47, 251.
Shimizu, T., 1996, Ph. D. Thesis, U. Tokyo.
Shimojo, M., Hashimoto, S., Shibata, K., et al., 1996, PASJ, 48, 123.
Shimojo, M., Shibata, K., and Harvey, K. L., 1998, Solar Phys., 178, 379.
Spicer, D., 1977, Sol. Phys., 53, 305.
Strong, K. T. et al., 1992, PASJ, 44, L161.
Sturrock, P. A., 1966, Nature, 211, 695.
Sturrock, P. A., 1992, in *Lecture Note in Physics, No. 399, Eruptive Flares*, ed. Z. Svestka, B. V. Jackson, and M. E. Machado (New York, Springer), p. 397.
Tajima, T., and Shibata, K., 1997, *Plasma Astrophysics*, Addison-Wesley.
Tsuneta, S., et al., 1991, Solar Phys., 136, 37.
Tsuneta, S., et al., 1992a, PASJ, 44, L63.
Tsuneta, S., et al., 1992b, PASJ, 44, L211.
Tsuneta, S., 1996, ApJ, 456, 840.
Tsuneta, S., 1997, ApJ, 483, 507.
Uchida, Y., and Shibata, K., 1988, Solar Phys., 116, 291.
Uchida,Y. et al., 1998, in these proceedings.
Ugai, M., 1986, Phys. Fluids, 29, 3659.
Watanabe, T., 1994, in *Proc. Kofu meeting*, eds. S. Enome, and T. Hirayama, Nobeyama Radio Observatory , p. 99.
Yokoyama, T., and Shibata, K., 1994, ApJ, 436, L197.
Yokoyama, T., and Shibata, K., 1995, Nature, 375, 42.
Yokoyama, T., and Shibata, K., 1996, PASJ, 48, 353.
Yokoyama, T., and Shibata, K., 1997, ApJ, 474, L61.
Yokoyama, T., and Shibata, K., 1998, ApJ, 494, L113.
Zhang, H., et al., 1998, in *Proc. Observational Plasma Astrophysics*, Watanabe, T., Kosugi, T., and Sterling, A. C. (eds), Kluwer, p. 391.

RELATIONSHIP BETWEEN THE TIME EVOLUTION OF MAGNETOTAIL RECONNECTION AND SUBSTORMS

Tatsuki Ogino

Solar-Terrestrial Environment Laboratory, Nagoya University, Toyokawa 442, Japan

Abstract. Relationship between the time evolution of magnetotail reconnection and substorms has been studied by using a 3-dimensional magnetohydrodynamic model when the interplanetary magnetic field (IMF) turns from northward to southward. The time evolution of the magnetosphere is divided into four phases: pre-growth, growth, main expansion and relaxation. It takes about 8 minutes from the onset of tail reconnection up to the onset of main expansion phase of substorms. Full development of a near-earth neutral line initiates the main expansion phase to generate strong earthward and tailward flows and to enhance rapidly plasma temperature. Southward turning of the IMF leads to several transient phenomena such as propagation of a convection front, stagnation of convection, tearing of the plasma sheet and generation of field aligned currents. The kinetic energy flux to carry energy toward the earth due to tail reconnection is quickly converted to the plasma pressure flux and then the Poynting flux in the plasma sheet and inner magnetosphere.

1. Introduction

When the solar wind and the interplanetary magnetic field (IMF) change, the earth's magnetosphere responds in a complicated way [*Fedder and Lyon,* 1995; *Walker at al.,* 1993]. The size of the magnetosphere can be well determined by the dynamic pressure of the solar wind, however the response time to reach a new steady state depends on the regions of magnetosphere. The dayside magnetosphere usually responds to the variations in 10-20 minutes; on the other hand, the plasma sheet in the midnight region does so in 40-60 minutes [*Walker at al.,* 1998]. Thus the earth's magnetosphere has typical two response times [*Bargatze et al.,* 1999] to variations of the solar wind and the IMF. Moreover, wavy phenomena and large scale fluctuations are easily excited in various boundary layer regions of the magnetosphere when the upstream disturbance of the solar wind and IMF pass through the magnetosphere.

Phenomena such as flux transfer events (FTEs) in the dayside magnetosphere show that magnetic reconnection in the magnetosphere does not occur in a steady manner. The plasma sheet usually does not reach a static steady state as time elapses because tail reconnection may occur in an intermittent and patchy manner. In particular, high level fluctuations or wavy phenomena can be seen in the plasma sheet and at the magnetopause during southward IMF in the global magnetohydrodynamic (MHD) simulation. Temporal variations in the solar wind and IMF may accelerate this complicated behavior. Therefore, it becomes important to distinguish spontaneous phenomena associated with intermittent and patchy reconnection and transient phenomena associated with upstream disturbances.

In the present paper, we have studied the response of the magnetosphere to variations in the solar wind and IMF using a 3-dimensional global MHD simulation of interaction between the solar wind and the magnetosphere. In particular, when the IMF turns from northward to southward, time evolution of the magnetosphere is presented and the physical precesses are discussed in connection with magnetic reconnection in the near-earth tail.

2. Simulation Model

We solved the normalized resistive MHD and Maxwell's equations as an initial value problem by using a modified version of the Leapfrog scheme which is a combination of the Leapfrog scheme and the two step Lax-Wendroff scheme. The latest version of our MHD model was presented in detail by *Ogino et al.* [1992, 1994], so we will just mention the main different features here.

The normalized MHD equations are written as follows:

$$\partial\rho/\partial t = -\vec{\nabla}\cdot(\vec{v}\rho) + D\nabla^2\rho$$

$$\partial\vec{v}/\partial t = -(\vec{v}\cdot\vec{\nabla})\vec{v} - \vec{\nabla}P/\rho + (\vec{J}\times\vec{B})/\rho + \vec{g} + \vec{\Phi}/\rho$$

$$\partial P/\partial t = -(\vec{v}\cdot\vec{\nabla})P - \gamma P\vec{\nabla}\cdot\vec{v} + D_p\nabla^2 P$$

$$\partial\vec{B}/\partial t = \vec{\nabla} \times (\vec{v} \times \vec{B}) + \eta\nabla^2\vec{B}$$
$$\vec{J} = \nabla \times (\vec{B} - \vec{B}_d)$$

where ρ is the plasma density, $\vec{v}$ is the flow velocity, P is the plasma pressure, $\vec{B}$ is the magnetic field, $\vec{B}_d$ is the dipole magnetic field of the earth, $\vec{J}$ is the current density, $\vec{g}$ is the force of gravity, $\vec{\Phi} = \mu\nabla^2\vec{v}$ is the viscosity, $\gamma = 5/3$ is the ratio of specific heats and η is the resistivity. Subtraction of the dipole magnetic field in calculation of the current density is to decrease numerical errors of finite difference near the earth. The classical resistivity was taken to be $\eta = \eta_o(T/T_o)^{-3/2}$, where $T = P/\rho$ is the temperature, T_o is the ionospheric temperature, $\eta_o = 0.001$. The diffusion coefficients are $\mu/\rho_{sw} = D = D_p = 0.001$, where ρ_{sw} is the solar wind density. The magnetic Reynord's number is $S = \tau_\eta/\tau_A \geq 100$, where $\tau_\eta = \Delta x^2/\eta$, and $\tau_A = \Delta x/v_A$, Δx is the mesh size and v_A is the Alfven velocity. The diffusion and viscous terms were added to suppress MHD fluctuations which come from unbalanced forces at the start of the simulation. Since these terms are kept to be small values, they have no serious effects to simulated global magnetospheric configurations.

In the simulation a uniform solar wind with $n_{sw} = 5$ cm^{-3}, $v_{sw} = 300$ km/s and $T_{sw} = 2 \times 10^5$ °K flows into a simulation box. These parameters are on the low side of observed solar wind parameters except for temperatures. The simulation box has dimensions of $-130\ R_e \leq x \leq 30\ R_e$, $0 \leq y \leq 40\ R_e$ and $0 \leq z \leq 40\ R_e$, because a grid of $(322, 82, 82)$ with a mesh size of $0.5\ R_e$ was used. Free boundary conditions were used at $x = -130\ R_e$, $y = 40\ R_e$ and $z = 40\ R_e$. At $y = 40\ R_e$ and $z = 40\ R_e$ the free boundary is at 45° to the x-axis. Mirror boundary conditions were used at $y = 0$ and $z = 0$. The ionospheric boundary condition imposed near the earth was determined by requiring a static equilibrium. We held all of the ionospheric parameters constant for $r \leq 3.5\ R_e$. A smoothing shape function damps out all perturbations near the ionosphere including parallel currents. The mirror dipole field was used at the initial state to eliminate the magnetic field in the upstream region. The time step was selected as $\Delta t = 4\Delta x/v_A = 1.87$ sec in order to assure the numerical stability condition.

3. Simulation Results

In the simulation we first obtained quasi-steady state magnetospheric configurations for northward IMF and southward IMF by running the code for 390 minutes before starting our studies. The IMF was zero for the first 120 minutes and finite for the next 270 minutes. The IMF was suddenly changed again at 390 minutes and hereafter we refer the time of IMF changes to be zero.

Figure 1 shows two dimensional patterns of the electric potential and plasma convection in the polar region for southward IMF, no IMF and northward IMF, after quasi-steady state magnetospheric configurations were again reached. Two kinds of convective flow in the ionosphere were calculated: compressible flow due to direct mapping of the inner magnetospheric flow (middle row) and incompressible flow obtained from the electric potential by assuming $\nabla \cdot \boldsymbol{v} = 0$ (bottom row). A two cell convection pattern is formed for southward IMF and four cells formed for northward IMF. For no IMF the high latitude cells are small and resemble the high latitude cells for northward IMF. However, sunward flow at high latitudes is negligible in the compressional flow pattern. The difference comes from the stagnation of flow by stretching magnetic field lines in the distant tail.

Figure 2 shows the time evolution of half of the cross polar cap electric potential when the IMF changed, where S and N mean southward and northward IMFs, respectively. The first 10 minutes correspond to the propagation time of the IMF discontinuity from the upstream boundary of simulation box to the magnetopause. Therefore, the response time of the polar cap potential is about 20 minutes for southward turning and it becomes longer when the IMF turns to zero and northward. As is shown in Figure 3, the near-earth neutral line starts forming at $t = 60$ min and the main expansion occurs between 75 min and 105 min after the IMF turns from northward to southward. The dip of potential for $t = 75 - 105$ min corresponds to the accumulation of the magnetic field energy near the plasma sheet.

Figure 3 shows the time evolution of the physical quantities in the magnetosphere when the IMF turns from northward to southward at $t = 390$ min, where the northward IMF was imposed for $t = 120 - 390$ min. As mentioned previously, the time of southward turning is referred as zero. Then the time variation can be classified to four phases: pre-growth phase for $0 - 30$ min, growth phase for $30 - 75$ min, main expansion phase for $75 - 105$ min and relaxation phase after 105 min. In the pre-growth phase the merging site switches from the high latitude tail to the subsolar region at the magnetopause. In the growth phase tail lobe convection increases, a near-earth neutral line appears at 60 min and expands towards the dawn and dusk magnetopause. In the main expansion phase both earthward and tailward flows develop rapidly,

and the plasma sheet is torn to enhance the plasma pressure in the near tail and to eject a plasmoid. After the plasmoid ejection, the near-earth neutral line is maintained at $x = 13 - 15$ Re, the plasma pressure and earthward flow decrease and approach constant values in the relaxation phase. Thus quasi-steady convection flow is formed for steady southward IMF.

Figure 4 shows the time evolution of two dimensional configurations of the magnetic field lines and the plasma pressure when the IMF turns from northward to southward. At $t = 435$ min (45 min), 435 min means the time from the start of simulation and 45 min the time from southward turning. Four panels show the magnetospheric configurations for growth phase at 45 min, onset time of the near-earth neutral line at 60 min, start of main expansion at 75 min and expansion phase at 90 min. At the onset time the neutral line forms in a narrow region around midnight. Then it expands toward the dawn and dusk magnetopause. The expansion phase starts with the sudden development of earthward and tailward flow. In the main expansion phase the plasma sheet is torn, then the plasma pressure in the earth side of plasma sheet enhances and a plasmoid is ejected.

Figure 5 shows three kinds of energy: kinetic energy, $E(K) = \frac{1}{2}\rho v^2$, internal energy of plasma, $E(P) = \frac{3}{2}P$, magnetic field energy, $E(B) = \frac{1}{2}B^2$, and the total energy, $E(T) = E(K) + E(P) + E(B)$ at the time of 0 min (northward IMF), 45 min (growth phase), 60 min (onset time of near-earth neutral line), 75 min (start of expansion phase), 90 min (expansion phase) and 135 min (quasi-steady state for southward IMF). Those values were calculated by integration in the $y - z$ plane for $r \leq (y^2 + z^2)^{1/2} \leq 12$ R_e. It is clearly seen that the magnetic field energy in the tail increases up to the start time of the main expansion at $t = 75$ min. At $t = 90$ min of main expansion phase, the internal plasma energy enhances in the near-earth tail for $x \geq -10$ R_e and plasmoid ejection is also seen near $x = -33$ R_e. The internal plasma energy for southward IMF is much less than that for northward IMF in the middle tail for -30 $R_e \leq x \leq -10$ R_e even though the magnetic field energy for southward IMF is greater than that for northward IMF.

Figure 6 shows temporal variation of magnetic field lines in noon-midnight meridian obtained by a high spatial resolution when the IMF flips from northward to southward at $t = 300$ min, where a grid of (480,220,220) with a mesh size of $0.15Re$ was used. Parameters of the solar wind and the IMF were chosen as $n_{sw} = 46$/cc, $v_{sw} = 412$ km/s, $T = 200,000$°K and $B_z = \pm 18.2$ nT to simulate the 1997 January events when abnormal solar-terrestrial phenomena for extremely high plasma density of the solar wind happened. Thinning of the closed field region is occurring in the plasma sheet due to transport of magnetic flux from dayside toward nightside after the IMF turns from northward to southward. The z component of the magnetic field becomes negative for the first time at $t = 342$ min in the plasma sheet. At that time a very thin plasma sheet is created and a sharp transition of the magnetic field configuration from dipole-like to tail-like appears a very near-earth region almost corresponding to the geostationary radius in the midnight tail. The main expansion phase, which is characterized by rapid increases of the earthward and tailward plasma flows and also the plasma temperature, starts at $t = 350$ min, about 8 minutes later from the onset of the tail reconnection. At that time all the closed field lines are reconnected and closed field lines covering the magnetic island does not exist anymore, that is, the lobe open field lines begin to engage the tail reconnection.

Figure 7 shows structure of the earth's magnetosphere at time steps near the onset time of tail reconnection ($t = 342$ min) and near the time of expansion onset ($t = 350$ min) obtained by using a high spatial resolution MHD simulation as same as in Figure 6. A very thin plasma sheet structure with about $1Re$ thickness is clearly seen at $t = 342$ min and the sharp transition of magnetic field configuration from dipole-like to tail-like occurs near the geostationary radius because the solar wind dynamic pressure is quite large as $P_{sw} = 15$ nPa in the 1997 January events. At the time of the main expansion onset, $t = 350$ min, strong earthward and tailward flows suddenly generate on both sides of the near-earth neutral line (NENL). The plasma sheet is torn into two parts from the NENL and a plasmoid is just ejected toward the tail. At the same time, the plasma temperature also suddenly enhances more than 5 times the previous steady value in the plasma sheet to imply formation of slow shock structure even on the earth side the NENL.

4. Discussion

In Figure 8 we have drawn a schematic diagram of the time evolution of the polar convection and the reconnected field lines when the IMF turns from northward to southward. Four cell convection during northward IMF changes to two cell convection for southward IMF in a short time of about 20 minutes. The convection front corresponding to a discontinuity surface in the IMF propagates from the dayside to the nightside across the polar cap and it can be seen in the compressible flow pattern. The flow velocity

is about 1 km/s in the ionosphere. The thick line in the field line plot stands for the discontinuity surface of the IMF. The convection front approaches the nightside boundary of the polar cap in about 1 hour and the antisunward flow once stagnates at the midnight boundary. The stagnation occurs just prior to the onset of tail reconnection and it correspond to the last stage of growth phase.

Tail reconnection or near-earth neutral line (NENL) develops and expands toward the dawn and dusk magnetopause. The development of tail reconnection again generates a sudden and strong flow toward low latitudes in the midnight region of the polar cap, which corresponds to earthward flow in the magnetosphere due to tail reconnection. This process occurs during the main expansion phase in the present simulation. The power in the earthward flow is quickly converted to Poynting flux. The energy is dominantly transferred from nightside to dayside in the middle magnetosphere by Poynting flux.

Figure 9 shows a schematic diagram of the time evolution of magnetic reconnection in the noon-midnight meridian, where $t = 0$ is now the onset time of the NENL. Poynting flux carries the magnetic flux from the dayside magnetosphere to tail lobes in growth phase for $t \leq 0$ and hence the plasma sheet is thinning and is continuously stretched[*Walker at al.*, 1993; *Papadopoulos et al.*, 1993]. Tail reconnection develops for $0 \leq t \leq 15$ min and strong earthward and tailward flow is triggered to start main expansion phase at about $t = 15$ min. Then the plasma sheet is torn into two parts: an inner part corresponding to enhancement of plasma pressure in the near-earth tail for $x \geq -10$ Re and an outer part where the plasmoid is ejected.

Figure 10 shows a schematic diagram of magnetotail dynamics in connection with the energy transfer. A strong earthward flow is generated by tail reconnection and the speed becomes comparable with the solar wind flow. The earthward flow is localized near the midnight region. The parallel component of the flow influences particle precipitation into the ionosphere, while the perpendicular component influences dipolarization of the magnetic field lines and the distortion of closed field lines to generate region 1 type field aligned currents through parallel vorticity. In the torn plasma sheet, the earthward part of the plasma sheet has two significant pressure gradients: an inner gradient corresponding to the inner edge of plasma sheet and an outer gradient on the NENL side. The both gradients generate region 2 type field aligned currents given by $J_{\parallel} \propto \nabla p \times \nabla B$ [*Vasyliunas*, 1980].

5. Conclusions

We have presented a 3-dimensional global MHD simulation of interaction between the solar wind and the earth's magnetosphere when the IMF turns from northward to southward, and discussed magnetotail dynamics in association with formation of near-earth neutral line. After southward turning of the IMF, time evolution of the magnetosphere can be distinguished in four phases: pre-growth phase, growth phase, main expansion phase and relaxation phase. Initial appearance of the near-earth neutral line is in later time of the growth phase and the main expansion starts when the neutral line expands up to the dawn and dusk magnetopause. In other words, all the closed field lines are reconnected and the lobe open field lines begin to engage the tail reconnection.

Development of the tail reconnection generates a strong earthward flow as well as a tailward flow, sudden increase of the plasma temperature and plasmoid ejection in the plasma sheet. The localized earthward flow near the noon-midnight meridian creates distortion of magnetic field lines to generate region 1 type field aligned currents and significant pressure gradients in the torn inner plasma sheet to generate region 2 type field aligned currents. The large portion of energy for the earthward flow is transferred from near tail to dayside magnetosphere by Poynting flux. Further detailed study of the energy transfer and tail reconnection waits for future simulation with higher spatial resolution.

Acknowledgments. The work was supported by a grant in aid for science research from the Ministry of Education, Science and Culture. Computing support was provided by the Computer Center of Nagoya University.

References

Fedder, J. A., and J. G. Lyon, The Earth's magnetosphere is $165R_E$ long: Self-consistent currents, convection, magnetospheric structure, and processes for northward interplanetary magnetic field, *J. Geophys. Res., 100,* 3623-3635, 1995.

Ogino, T., R. J. Walker, and M. Ashour-Abdalla, A global magnetohydrodynamic simulation of the magnetosheath and magnetosphere when the interplanetary magnetic field is northward, *IEEE Transactions on Plasma Science, 20,* 817-828, 1992.

Ogino, T., R. J. Walker, and M. Ashour-Abdalla, A global magnetohydrodynamic simulation of the response of the magnetosphere to a northward turning of the interplanetary magnetic field, *J. Geophys. Res., 99,* 11,027-11,042, 1994.

Papadopoulos, K., A. S. Sharma, and J. A. Valdivia, Is the magnetosphere a lens for MHD waves?, *Geophys. Res. Lett., 20,* 2,809-2,812, 1993.

Vasyliunas, V.M., Plasma sheet dynamics: effects on, and feedback from, the polar ionosphere, in *Exploration of the Polar Upper Atmosphere,* edited by C. S. Deehr and J. A. Holtet, pp. 229-244, D. Reidel, Dordrecht-Holland, 1980.

Walker, R. J., T. Ogino, J. Raeder, and M. Ashour-Abdalla, A global magnetohydrodynamic simulation of the magnetosphere when the interplanetary magnetic field is southward: The onset of magnetic reconnection, *J. Geophys. Res., 98,* 17,235-17,249, 1993.

Bargatze, L.F., T. Ogino, R.L. McPherron, and R.J. Walker, Solar wind magnetic field control of magnetospheric response delay and expansion phase onset timing, *J. Geophys. Res., 104,* 14,583-14,599, 1999.

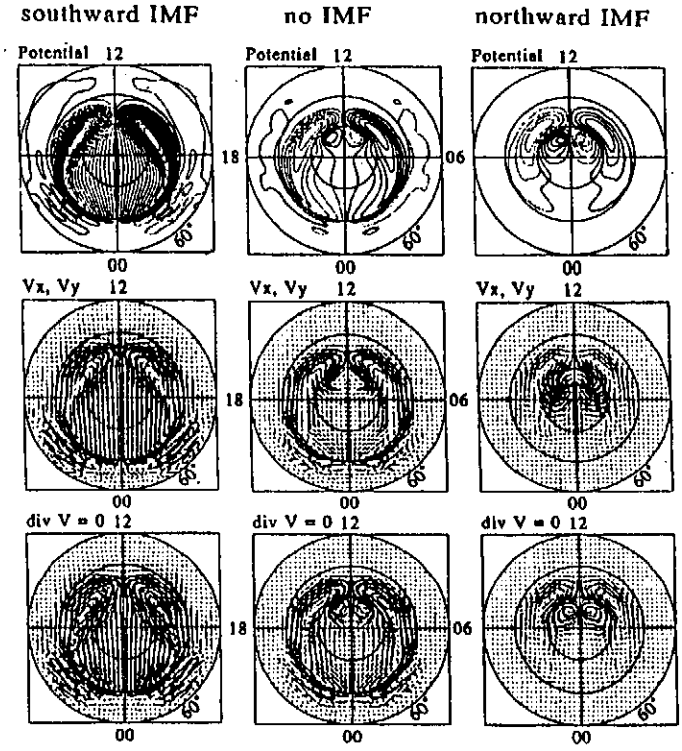

Figure 1. Two dimensional patterns of the electric potential and plasma convection in the polar region for southward IMF ($B_z = -5$ nT), no IMF ($B_z = 0$ nT) and northward IMF($B_z = 5$ nT).

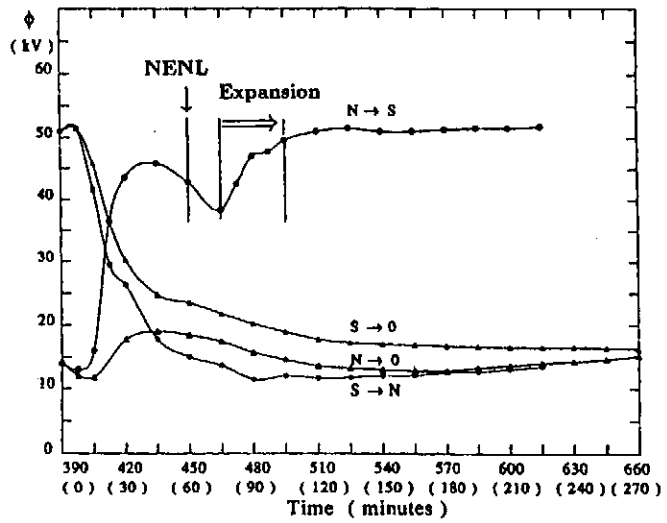

Figure 2. Time evolution of the polar cap electric potential when the IMF changes.

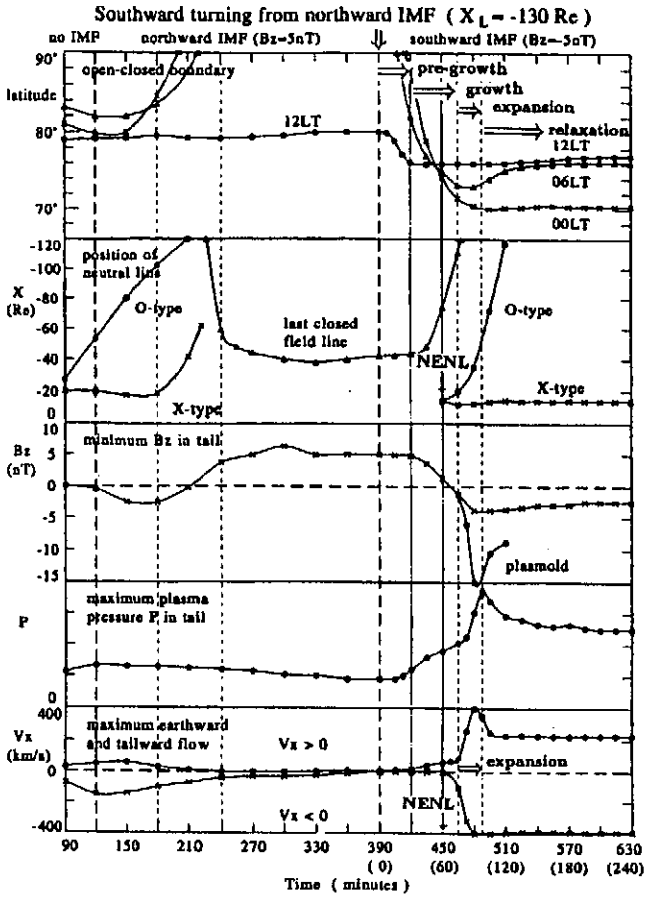

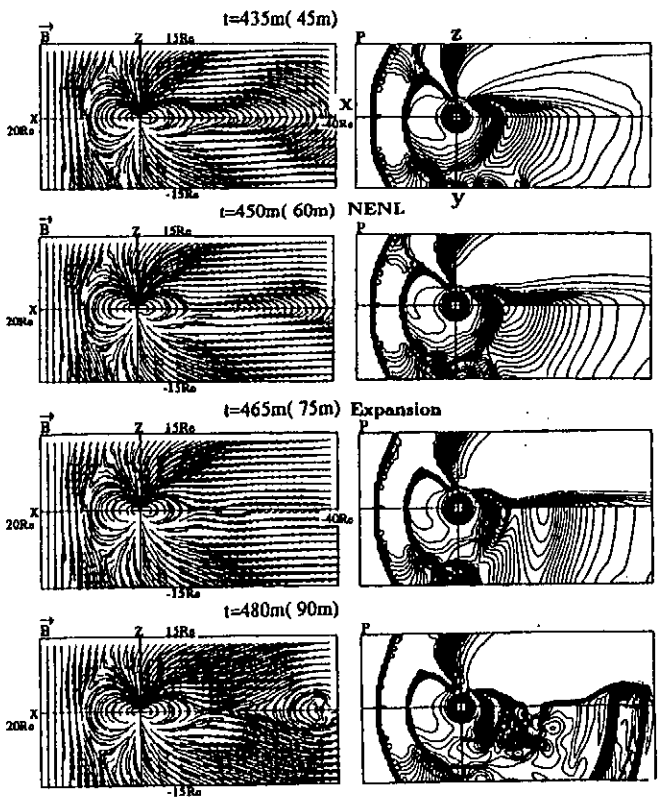

Figure 4. Two dimensional configurations of the magnetic field lines and the plasma pressure when the IMF turns from northward (B_z = 5 nT) to southward ($B_z = -5$ nT).

Figure 3. Time evolution of the physical quantities in the magnetosphere when the IMF turns from northward ($B_z = 5$ nT) to southward ($B_z = -5$ nT) at $t = 390$ min.

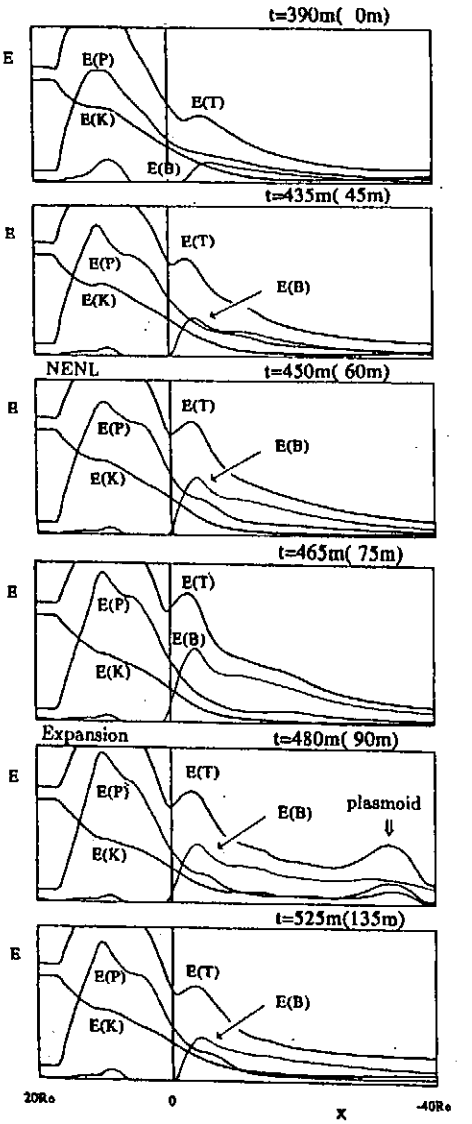

Figure 5. Profiles of three kinds of energy and the total energy along sun-earth line, where the values were given by integrating in $y - z$ plane for $r \leq (y^2 + z^2)^{1/2} \leq 12\ R_e$.

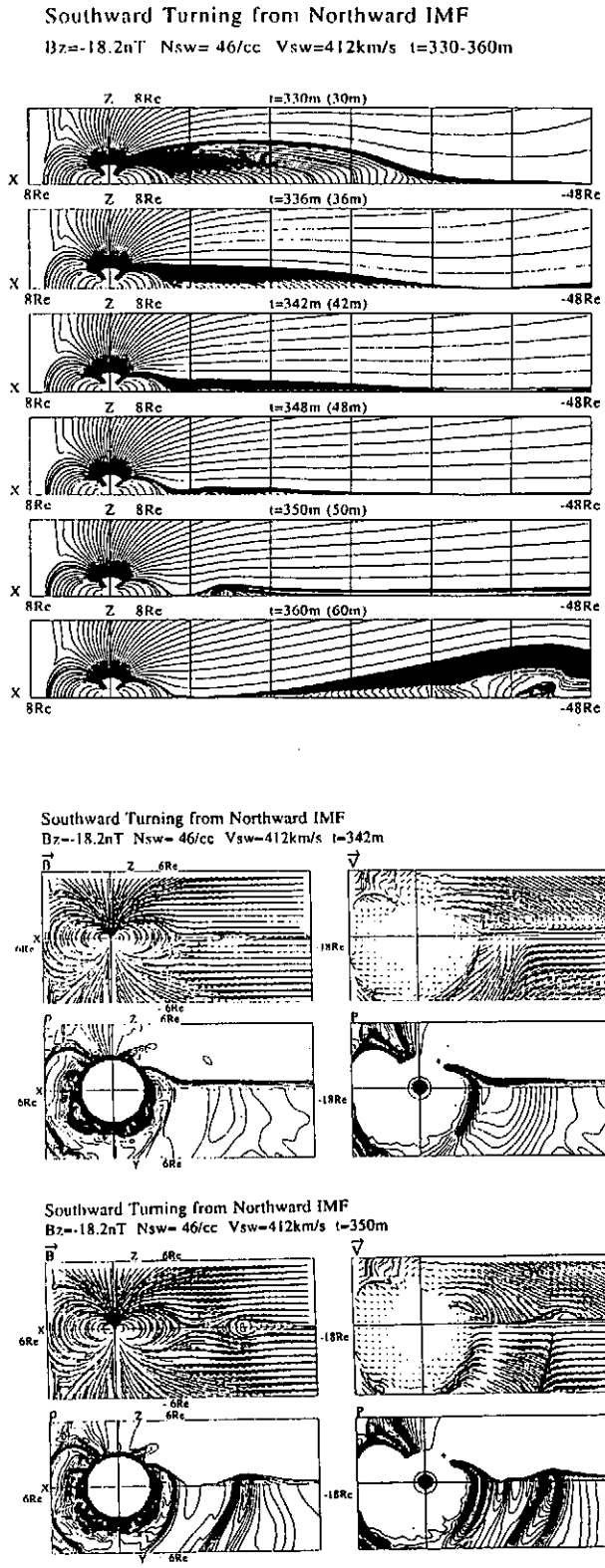

Figure 7. Structure of the earth's magnetosphere at time steps near the onset time of tail reconnection (t = 342 min) and near the time of expansion onset (t = 350 min) obtained by using a high spatial resolution MHD simulation.

Figure 6. Temporal variation of magnetic field lines obtained by a high spatial MHD simulation when the IMF flips from northward to southward at t = 300 min.

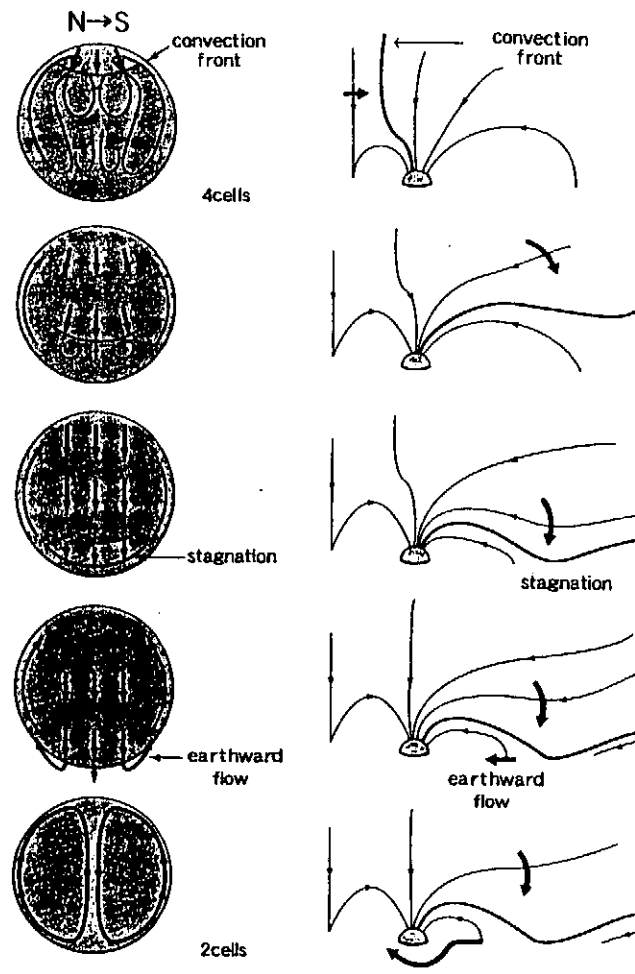

Figure 8. Schematic diagram of time evolution of the polar convection and the reconnected field lines when the IMF turns from northward to southward.

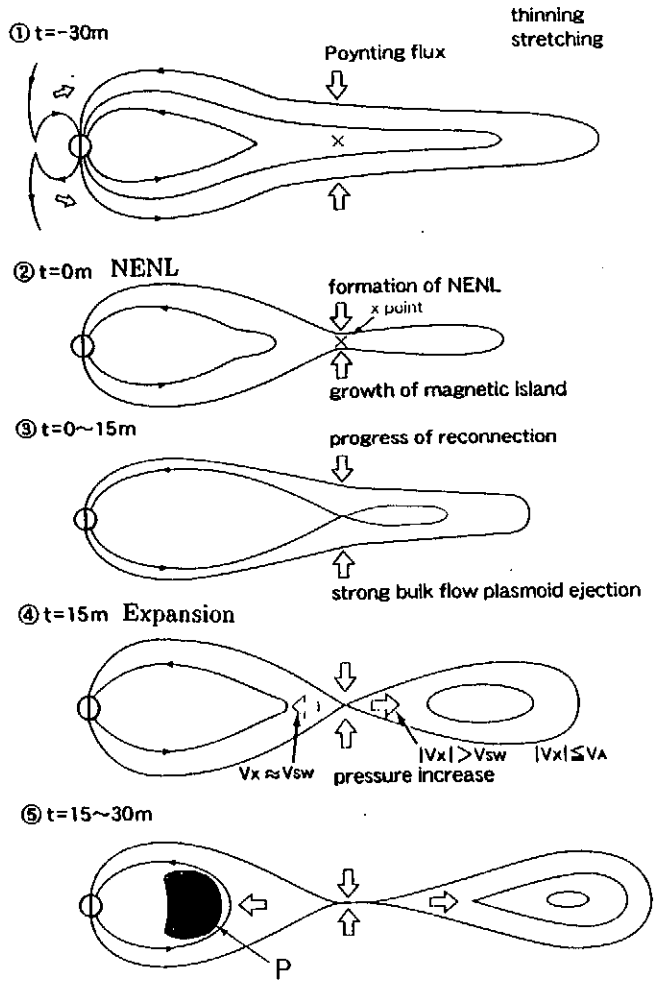

Figure 9. Schematic diagram of time evolution of magnetic reconnection in the noon-midnight meridian of the tail when the IMF turns from northward to southward.

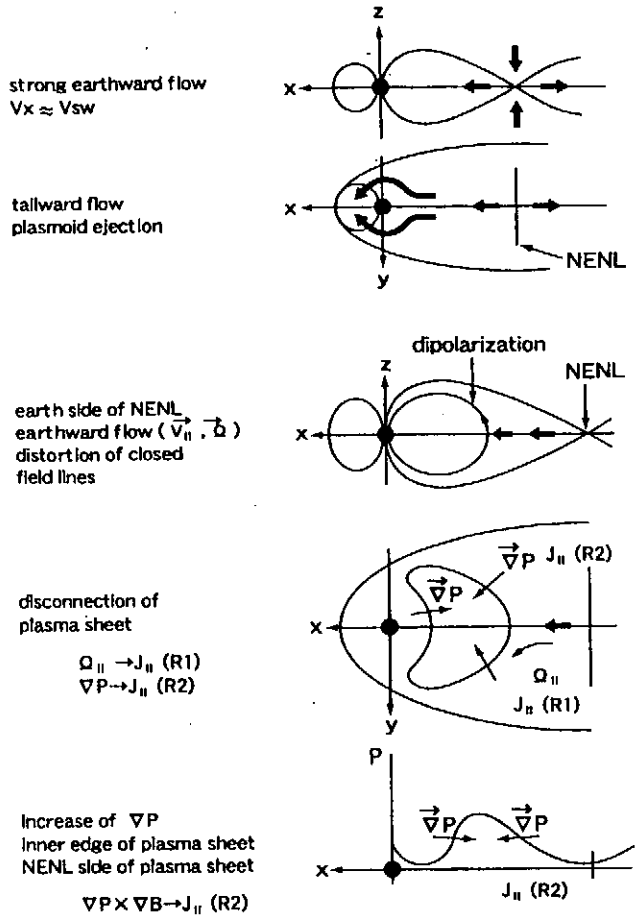

Figure 10. Schematic diagram of formation of the near-earth neutral line and its effects on magnetotail dynamics when the IMF turns from northward to southward.

Kinetic Ballooning Instability As A Substorm Onset Mechanism

C. Z. Cheng

Princeton Plasma Physics Laboratory, Princeton University
Princeton, NJ 08543

Abstract

A new scenario of substorm onset and current disruption and the corresponding physical processes are presented based on the AMPTE/CCE spacecraft observation and a kinetic ballooning instability theory. During the growth phase of substorms the plasma β is larger than unity ($20 \geq \beta \geq 1$). Toward the end of late growth phase the plasma β increases from 20 to ≥ 50 in ~ 3 minutes and a low frequency instability with a wave period of $50 - 75$ sec is excited and grows exponentially to a large amplitude at the current disruption onset. At the onset, higher frequency instabilities are excited so that the plasma and electromagnetic field form a turbulent state. Plasma transport takes place to modify the ambient pressure profile so that the ambient magnetic field recovers from a tail-like geometry to a dipole-like geometry. A kinetic ballooning instability (KBI) theory is proposed to explain the low frequency instability (frequency and growth rate) and its observed high β threshold ($\beta_c \geq 50$). Based on the ideal MHD theory $\beta_c^{MHD} \simeq 1$ and the ballooning modes are predicted to be unstable during the growth phase, which is inconsistent with observation that no appreciable magnetic field fluctuation is observed. The enhancement of β_c over β_c^{MHD} is due to the kinetic effects of trapped electrons and finite ion Larmor radii which provide a large stabilizing effect by producing a large parallel electric field and hence a parallel current that greatly enhances the stabilizing effect of field line tension. As a result, β_c is greatly increased over β_c^{MHD} by a factor proportional to the ratio of the total electron density to the un-trapped electron density, n_e/n_{eu}, which is $\geq O(10^2)$ in the near-Earth plasma sheet. The wave-ion magnetic drift resonance effect produces a perturbed resonant ion velocity distribution centered at a duskward velocity roughly equal to the average ion magnetic drift velocity. This perturbed ion distribution explains the enhanced duskward ion flux during the explosive growth phase and can excite higher frequency instabilities (such as the cross-field current instability).

1 Introduction

A critical issue in the magnetospheric physics is the substorm process, in particular, the substorm onset and current disruption. Recently a new scenario of the substorm onset and current disruption has been presented [*Cheng and Lui*(1998)] based on the AMPTE/CCE spacecraft observations. In the late substorm growth phase the plasma β at the substorm onset site in the near Earth plasma sheet region is typically ~ 20 at ~ 10 minutes prior to the current disruption onset. At ~ 2 minutes before the substorm onset β increases to ≥ 50 and the pressure becomes isotropic [*Lui et al.*(1992)]. Therefore, too much plasma energy is stored in the plasma sheet and the excess energy must be release via instabilities and associated plasma and magnetic field transport. We have found that a low frequency instability with a wave period of $\sim 50 - 75$ sec is excited and grows exponentially to a large amplitude with $\delta B/B \geq 0.5$ at the onset. The half wave period of the instability before the onset was previously called "explosive growth phase" [*Ohtani et al.*(1992), *Ohtani et al.*(1995)] which lasts ~ 30 sec with an enhanced duskward ion flux centered at ~ 500 km/s (below the ion thermal velocity of ≈ 1000 km/s)[*Lui*(1996)]. This enhanced cross-tail ion drift population is responsible for exciting higher frequency instabilities (with wave periods of 15 sec, 10, sec, 5 sec; etc.) which together with the low frequency instability last throughout the current disruption phase to form a strong turbulence for $\sim 4 - 5$ minutes. During the turbulent state anomalously fast plasma transport takes place to modify the average pressure profile so that the plasma sheet recovers to a lower energy state and the ambient magnetic field relaxes from a tail-like geometry to a dipole-like geometry.

Previously the ideal MHD ballooning instability has been proposed to explain the substorm current disruption and explosive growth phase [*Roux et al.*(1991), *Liu*(1997), *Voronkov et al.*(1997)]. The ballooning instability results from the release of free energy of nonuniform plasma pressure with a gradient in the same direction as the magnetic field curvature. Analogous to the expansion of a balloon due to higher inner air pressure around weak surface tension spot, the ballooning instability will relax higher plasma pressure and hence move the magnetic field lines across the large field curvature surface area toward the weaker pressure direction. Theories of ballooning modes based on the ideal MHD model would predict a purely growing instability when the plasma β is above a low critical value β_c^{MHD}. In a dipole field or a more tail-like field $\beta_c^{MHD} \simeq 1$ with $L_p = 1\mathrm{R_E}$. This is inconsistent with the AMPTE/CCE spacecraft observation that no appreciable magnetic field fluctuations were observed throughout most of the growth phase even when plasma β values are above β_c^{MHD} (typically $40 \geq \beta \geq 1$).

In this paper we present a kinetic theory of ballooning instability (KBI) which shows that kinetic effects of trapped particle dynamics, finite ion Larmor radii (FLR)

and wave-particle resonances are important in determining the stability of ballooning modes. The kinetic theory of ballooning modes provides a proper understanding of two key physical processes of substorm current disruption and subsequent magnetic field dipolarization: (1) the excitation mechanism and the high plasma β threshold (≥ 50) of the low frequency instability that underlines the explosive growth phase; (2) the physical mechanism of the enhanced duskward ion flux that occurs only during the explosive growth phase and leads to excitation of higher frequency instabilities. In particular, we show that the kinetic effects of trapped electrons and finite ion Larmor radii produce a large parallel electric field and hence a parallel current that greatly enhances the stabilizing effect of field line tension. As a result, the β threshold (β_c) for KBI is greatly increased over the ideal MHD ballooning instability threshold by $\geq O(10^2)$, which is consistent with the AMPTE/CCE observation of high β_c ($\beta_c \sim 50$) for exciting a low frequency instability just before the substorm onset. The kinetic ballooning instability has a real frequency on the order of ion diamagnetic drift frequency which is associated with ion FLR effects. Moreover, the wave-ion magnetic drift resonance effect produces a perturbed resonant ion velocity distribution centered at a duskward velocity which roughly equals to the average ion magnetic drift velocity. This perturbed ion distribution explains the enhanced duskward ion flux during the explosive growth phase and can excite higher frequency instabilities (such as the cross-field current instability).

In the following we first describe the derivation of the eigenmode equations for kinetic ballooning instability based on the gyrokinetic formulation. We then present the physical process of the kinetic ballooning instability and its application to understand the critical substorm processes. Then, we discuss the difficulties in attempting to explain the substorm process by the magnetic reconnection based on the near-Earth neutral line model [*Nagai and Kamide*(1995)]. Finally, a summary is given.

2 Gyrokinetic Formulation

In order to properly address kinetic effects on the ballooning instability we will employ the gyrokinetic formulation to describe the particle dynamics. We shall consider collisionless plasmas with isotropic pressure. The particle velocity distribution function is assumed to have no appreciable bulk flow velocity. Quasi-static equilibria with isotropic pressure are determined by the system of equations in the rationalized EMU unit: $\mathbf{j} \times \mathbf{B} = \nabla P$, $\nabla \times \mathbf{B} = \mathbf{J}$, and $\nabla \cdot \mathbf{B} = 0$. For three-dimensional magnetospheric equilibria the magnetic field can be expressed in a straight field line (ψ, α, θ) flux coordinate as $\mathbf{B} = \nabla\psi \times \nabla\alpha$, where ψ is the magnetic flux function, $\alpha = \phi - \delta(\psi, \alpha, \theta)$, θ is a generalized poloidal angle, ϕ is the azimuthal angle in the cylindrical (R, ϕ, Z) coordinate, and $\delta(\psi, \alpha, \theta)$ is periodic in both ϕ and θ. The intersection of constant ψ

and α surfaces defines the magnetic field line. The flux coordinate system is in general not orthogonal, and $\nabla\psi \cdot \nabla\theta \neq 0$, $\nabla\psi \cdot \nabla\alpha \neq 0$, and $\nabla\alpha \cdot \nabla\theta \neq 0$. Within a magnetic surface the poloidal flux is $\Psi = \int d^3x \mathbf{b} \cdot \nabla\theta/2\pi = 2\pi\psi$. Note that α is a cyclic function with a period of 2π for all constant ψ surfaces.

We consider low frequency perturbations with $\omega << \omega_{ci}$ and $k_\perp L >> k_\parallel L > 1$, where ω is the wave frequency, ω_{ci} is the ion cyclotron frequency, L is the equilibrium scale length, and $k_{\parallel,\perp}$ are the parallel and perpendicular wave numbers, respectively. Because the electron mass is much smaller than the ion mass and the temperatures of electrons and ions are of the same order, the electron thermal velocity is much larger than the ion thermal velocity. We consider electromagnetic perturbations with the orderings: $k_\perp \rho_i \sim O(1)$ and $v_{the} > (\omega/k_\parallel) > v_{thi}$ [*Cheng*(1982b), *Cheng*(1982a)], where ρ_i is the ion gyroradius. With these orderings the following kinetic effects must be considered: trapped electron dynamics, ion FLR effect and wave-particle resonance with $\omega - \omega_{di} = 0$, where ω_{di} is the ion magnetic drift frequency. We shall obtain approximate solutions of the perturbed particle distributions based on the gyrokinetic formulation [*Cheng et al.*(1995)].

We assume a WKB eikonal representation for perturbed quantities, *i.e.*, $\delta f(\vec{x}, \vec{v}, t) = \delta f(s, \mathbf{k}_\perp, \vec{v}, t) \exp\left[i\left(\int d\vec{x}_\perp \cdot \mathbf{k}_\perp - \omega t\right)\right]$. Including full gyroradius effects the perturbed particle distribution function can be expressed in terms of the rationalized MKS unit as $\delta f = (q/M)\partial F/\partial\mathcal{E}[(\omega_\star^T/\omega)\Phi - (1 - \omega_\star^T/\omega)\left(1 - J_0 e^{i\delta L}\right)\Phi] + g e^{i\delta L}$, where M is the particle mass, q is the particle charge, the guiding center particle equilibrium distribution is assumed to be $F = F(\mathcal{E}, \psi)$ so that the equilibrium pressure is a function of ψ and $\mathcal{E}$ only, $\delta L = \mathbf{k} \times \mathbf{v} \cdot \mathbf{B}/\omega_c B$, J_l is the l-th order Bessel function of the argument $k_\perp v_\perp/\omega_c$, $\omega_c = qB/M$ is the cyclotron frequency, B is the magnetic field intensity, Φ is the perturbed electrostatic potential, and g is the non-adiabatic part of the perturbed distribution function. Based on the WKB-ballooning formalism the gyrokinetic equation for g in the low frequency ($\omega \ll \omega_c$) limit is given by

$$(\omega - \omega_d + i\mathbf{v}_\parallel \cdot \nabla_\parallel) g = -\frac{q}{M}\frac{\partial F}{\partial \mathcal{E}}\left(1 - \frac{\omega_\star^T}{\omega}\right) \times \left[\left(\omega_d \Phi - i\mathbf{v}_\parallel \cdot \nabla_\parallel \Psi\right) J_0 + \frac{\omega v_\perp}{k_\perp} J_1 \delta B_\parallel\right], \quad (1)$$

where Ψ is the parallel perturbed electric field potential with $\mathbf{E}_\parallel = -\nabla_\parallel \Psi$, $\delta B_\parallel$ is the parallel perturbed magnetic field, $\omega_\star^T = \mathbf{B} \times \mathbf{k}_\perp \cdot \nabla F/(B\omega_c \partial F/\partial\mathcal{E})$, $\omega_d = \mathbf{k}_\perp \cdot \mathbf{v}_d$ is the magnetic drift frequency, $\mathbf{v}_d = (\mathbf{B}/B\omega_c) \times (v_\parallel^2 \boldsymbol{\kappa} + \mu \nabla B)$ is the magnetic drift velocity, and $\boldsymbol{\kappa}$ is the magnetic field curvature. Note that the vector potential, defined by $\mathbf{A} = \mathbf{A}_\parallel - iA_\perp \mathbf{B} \times \mathbf{k}_\perp/(Bk_\perp)$, is related to Φ, Ψ and $\delta B_\parallel$ by $\omega \mathbf{A}_\parallel = -i\nabla_\parallel(\Phi - \Psi)$ and $\delta B_\parallel = k_\perp A_\perp$. We also note that the gyrokinetic formulation is still valid for the case $\rho_i \sim L_\perp$ if the the magnetic drift frequency is replaced by the pitch angle average value

to account for the non-conservation of the magnetic moment [*Hurricane et al.*(1994)].

For electrons we shall neglect gyro-radius effects and consider $|v_\parallel \nabla_\parallel| \gg \omega, \omega_{de}$. Clearly, trapped and un-trapped electrons have very different parallel dynamics. The un-trapped electron dynamics is mainly determined by its fast parallel transit motion, and to the lowest order in $(\omega/|v_\parallel \nabla_\parallel|)$ the perturbed un-trapped electron density is given by [*Cheng*(1982a)]

$$\delta n_{eu} = \frac{eN_{eu}}{T_e}\left[\frac{\omega_{*e}}{\omega}\Phi + \left(1 - \frac{\omega_{*e}}{\omega}\right)\Psi\right], \tag{2}$$

where $\omega_{*e} = \mathbf{B} \times \nabla N_e \cdot \mathbf{k}_\perp T_e/(Bm_e\omega_{ce}N_e)$ is the electron diamagnetic drift frequency, $N_{eu}/N_e = 1 - [1 - B(s)/B_i]^{1/2}$ is the fraction of un-trapped electron at the field line location s, B_i is the maximum magnetic field along a field line. Near the minimum B location $N_{eu}/N_e \simeq B(s)/2B_i \ll 1$. Note that the first term in Eq. (2) is the adiabatic response and the second term is due to the parallel electric field.

The trapped electron dynamics is mainly determined by its fast parallel bounce motion and to the lowest order in (ω/ω_{be})

$$\delta n_{et} \simeq \frac{eN_{et}}{T_e}\left[\frac{\omega_{*e}}{\omega}\Phi + \left(1 - \frac{\omega_{*e}}{\omega}\right)\Delta\Psi\right] + \delta\hat{n}_{et}, \tag{3}$$

where $N_{et}/N_e = [1 - B(s)/B_i]^{1/2}$ is the fraction of trapped electron,

$$\Delta = \int_{tr} d^3v (F_e/N_{et})\left[1 - \frac{\langle(\omega - \omega_{de})\Psi\rangle}{\langle\omega - \omega_{de}\rangle\Psi}\right], \tag{4}$$

$$\delta\hat{n}_{et} = -\int_{tr} d^3v (eF_e/T_e)[(\omega - \omega^T_{*e})/(\omega - \langle\omega_{de}\rangle)]\left\langle(\omega_{de}/\omega)\Phi + v_\perp^2\delta B_\parallel/2\omega_{ce}\right\rangle, \tag{5}$$

and $\langle\omega_{de}\rangle$ is the trapped particle orbit average of ω_{de}. Note that the contribution due to the parallel electric field is small because $\Delta \ll 1$ for trapped electrons. Thus, it is difficult to change the trapped electron density by the parallel electric field because of their fast bounce motion relative to the parallel wave motion.

To obtain perturbed ion distribution function we assume that $\omega, \omega_{di} \gg |v_\parallel \nabla_\parallel|$, and the non-adiabatic perturbed distribution function is given by

$$g_i \simeq \frac{eF_i}{T_i}\frac{\omega - \omega^T_{*i}}{\omega - \omega_{di}}\left(\frac{\omega_{di}J_0\Phi}{\omega} + \frac{v_\perp J_1 \delta B_\parallel}{k_\perp}\right). \tag{6}$$

Note that the ion dynamics is mainly determined by its perpendicular motion and the perturbed ion density is given by

$$\delta n_i = -\frac{eN_i}{T_i}\left[\frac{\omega_{*i}}{\omega}\Phi + \left(1 - \frac{\omega_{*pi}}{\omega}\right)(1 - \Gamma)\,\Phi\right] + \delta\hat{n}_i, \tag{7}$$

where $\omega_{*i} = \mathbf{B} \times \nabla N_i \cdot \mathbf{k}_\perp T_i/(Bm_i\omega_{ci}N_i)$, $\omega_{*pi} = \mathbf{B} \times \nabla P_i \cdot \mathbf{k}_\perp T_i/(Bm_i\omega_{ci}P_i)$, $\Gamma(b_i) = I_0(b_i)\exp(-b_i)$, $b_i = k_\perp^2 T_i/M_i\omega_{ci}^2 = k_\perp^2\rho_i^2/2$, I_0 is the modified Bessel function of the zeroth order, and $\delta\hat{n}_i = \int d^3v g_i J_0$.

¿From the charge quasi-neutrality condition we obtain the parallel electric field potential

$$\left(\frac{N_{eu}+N_{et}\Delta}{N_e}\right)\Psi = -\frac{T_e}{T_i}\frac{\omega-\omega_{*pi}}{\omega-\omega_{*e}}(1-\Gamma)\Phi + \frac{T_e}{eN_e}(\delta\hat{n}_i - \delta\hat{n}_e) \tag{8}$$

In comparison with the limit without trapped electron effects, the parallel electric field is enhanced by $N_e/(N_{eu}+N_{et}\Delta)$. Making use of the parallel Ampere's law the perturbed parallel current is given by $\delta J_\parallel \simeq i\nabla_\perp^2\nabla_\parallel(\Phi-\Psi)/\omega$, which represents the enhancement of stabilizing field line tension due to the enhanced parallel electric field resulting from effects of trapped electron dynamics and ion FLR.

To obtain the eigenmode equation for ballooning instability we follow the derivation presented in the paper by [*Cheng et al.*(1995)]. By multiplying the gyrokinetic equation with particle charge, integrating it over the velocity space and summing it over all species, and making use of the parallel component of the Ampere's law we obtain

$$\mathbf{B}\cdot\nabla\left[\frac{k_\perp^2}{B^2}\mathbf{B}\cdot\nabla(\Phi-\Psi)\right] + \frac{\omega(\omega-\omega_{*pi})}{V_A^2}\frac{1-\Gamma(b_i)}{\rho_i^2/2}\Phi + \frac{\mathbf{B}\times\boldsymbol{\kappa}\cdot\mathbf{k}_\perp}{B^2}\left(\frac{2\mathbf{B}\times\nabla P\cdot\mathbf{k}_\perp}{B^2}\Phi - \omega\sum_j\delta\hat{p}_j\right) = 0 \tag{9}$$

where $V_A = B/(n_iM_i)^{1/2}$ is the Alfvén speed, and the non-adiabatic perturbed pressures for each particle species are given by $\delta\hat{p}_j = M_j\int d^3v[(1-\omega_{*j}^T/\omega)(1-J_0^2)\Phi + g_jJ_0](v_\perp^2/2 + v_\parallel^2)$. Note that the perturbed total pressure balance relation, $\mathbf{B}\cdot\delta\mathbf{B} + \delta P_\perp \simeq 0$, is used for low frequency instabilities with $\omega \ll k_\perp V_A$ [*Cheng*(1991), *Cheng and Qian*(1994), *Cheng et al.*(1995)].

Equations (8) and (9) form a coupled set of kinetic ballooning eigenmode equations for solving Φ and Ψ along the field lines and the eigenvalue ω. We also need to obtain the non-adiabatic contributions of perturbed electron density, $\delta\hat{n}_{et}$ and $\delta\hat{n}_i$, and perturbed particle pressures, $\delta\hat{p}_\parallel$ and $\delta\hat{p}_\perp$. The eigenmode equations include kinetic effects of trapped electron dynamics, parallel electric field, full ion FLR, and wave-particle resonances.

3 Kinetic Ballooning Instability

If we further consider the ordering $\omega \gg \omega_{de}, \omega_{di}$, the non-adiabatic density and pressure responses in Eqs. (8) and (9) can be neglected and we obtain a kinetic ballooning mode

equation that retains the trapped electron and ion FLR effects, and the local dispersion relation for KBI is approximately given by

$$\frac{\omega(\omega-\omega_{*pi})}{(1+b_i)V_A^2} \simeq Sk_\parallel^2 - \frac{2\boldsymbol{\kappa}\cdot\nabla P}{B^2}, \tag{10}$$

where $S = 1 + (b_i/(1+b_i))N_eT_e/(N_{eu}+N_{et}\Delta)T_i \gg 1$, and we have adopted the Padé approximation $1-\Gamma \simeq b_i/(1+b_i)$. The real frequency of KBI is $\omega_r \simeq \omega_{*pi}/2$ and the critical β is given by

$$\beta_c \simeq S\beta_c^{MHD} + \frac{\omega_{*pi}^2 R_c L_p}{4(1+b_i)V_A^2}, \tag{11}$$

where R_c is the radius of the magnetic field curvature and L_p is the pressure gradient scale length, and $\beta_c^{MHD} = k_\parallel^2 R_c L_p$ is the ballooning instability threshold based on the MHD theory.

We now briefly summarize the physical processes of kinetic stabilization effects of trapped electron dynamics and finite ion Larmor radii. In the substorm late growth phase the temperatures of electrons and ions are of the same order and the electron thermal velocity to be much larger than the ion thermal velocity. Because the frequency of kinetic ballooning instability is on the order of the ion diamagnetic drift frequency, its wave phase speed along the field line is usually much smaller than the electron thermal speed, but much larger than the ion thermal speed. Therefore, with respect to the parallel wave motion electrons move very rapidly along the field line with either transit or bounce motion depending on the particle pitch angle. On the other hand, ions moves very slowly with respect to the parallel wave motion and their parallel dynamics can be considered as static. Moreover, electron and ion motions across magnetic field lines are very different if the perpendicular wavelength is on the order of ion gyroradii; the electron perpendicular motion is essentially the $\mathbf{E}\times\mathbf{B}$ drift motion because of small mass, but the ion perpendicular motion is governed by both the $\mathbf{E}\times\mathbf{B}$ and polarization drifts. The difference in electron and ion motion across magnetic field lines can cause significant charge separation. In order to maintain the charge quasi-neutrality a parallel electric field must be produced to accelerate (or decelerate) electrons to positions where there is excess positive charge. A parallel electric field can easily accelerate (or decelerate) un-trapped electrons to change its density distribution. However, it is relatively harder to change the trapped electron density distribution by a parallel electric field because of their rapid bounce motion along the field lines. Thus, if the trapped electron population is larger than the un-trapped electron population, an enhanced parallel electric field will be produced to move electrons to maintain charge quasi-neutrality. The large parallel electric field will then drive an enhanced parallel current which can greatly increase the stabilizing field line tension over the value expected from the MHD theory

just like high-pressured water increases the tension of a hose. As a result, a much higher β_c than that based on the ideal MHD model is obtained with $\beta_c \approx O(N_e/N_{eu})\beta_c^{MHD}$, where $N_{eu}/N_e < 1$ is the un-trapped electron fraction and β_c^{MHD} is the critical β predicted by the ideal MHD theory. Therefore, for systems with a large fraction of trapped electron population the ideal MHD ballooning mode theory underestimates the critical β for instability and it is necessary to use the more complete kinetic theory.

The kinetic ballooning instability can interact with perpendicular ion motion via wave-ion magnetic drift resonance because ion moves much slower than the wave along the field lines. If $\omega \sim \omega_{di}$, the wave-ion magnetic drift resonance can provide an additional channel to release the KBI free energy and the growth rate and critical β can be modified. To fully evaluate the effect of wave-ion magnetic drift resonance, we need to retain ion non-adiabatic responses in perturbed density and pressures. Numerical studies of KBI have been performed for tokamaks previously [*Cheng*(1982b), *Cheng*(1982a)] and the results indicated that the effect of the wave-ion magnetic drift resonance is to reduce β_c by about 20% and the real frequency of KBI will increase to ω_{*pi} at critical β. We expect the results for the magnetosphere to be qualitatively similar to the tokamak case and the detailed numerical solutions will be presented in the future.

Another consequence of the wave-particle resonance is to produce a perturbed resonant ion distribution in the velocity space centered around $v_y = v_{di}$ that oscillates with KBI, where v_y is the particle velocity in the duskward direction and v_{di} is the resonant ion magnetic (∇B and curvature) drift velocity which is approximately equal to the average drift velocity. As KBI grows to a large amplitude, the perturbed ion velocity distribution enhances the duskward ion flux in one half of the wave phase and vice versa for the other half of the wave phase. The resulting change in ion velocity distribution gives rise to $\partial f_i/\partial v_y > 0$ near $v_y \sim v_{di}$, and provides an additional free energy source for exciting higher frequency instabilities.

One consequence of the wave-ion magnetic drift resonance is that as KBI grows to a large value with $\delta B/B \geq 0.3$ the perturbed resonant ion velocity distribution has a positive slope near the duskward resonant ion magnetic drift velocity. This can be clearly seen from the $(\omega - \omega_{di})$ resonance denominator in the perturbed ion distribution. Because $\omega_r \simeq \omega_{*pi}/2$, the wave-ion magnetic drift resonance will occur at $v_{di} = T_i \mathbf{B} \times \nabla P_i/(2eP_iB^2) \simeq v_{thi}\rho_i/2L_{pi}$, where ρ_i is the ion Larmor radius and L_{pi} is the ion pressure gradient scale length. Thus, $|v_{di}| \sim v_{thi}$ for $\rho_i \sim L_{pi}$.

4 Magnetic Reconnection

An alternative popular idea in the space plasma physics community regarding the mechanism responsible for the onset of substorm expansion phase is the magnetic reconnec-

tion [*Sweet*(1958), *Parker*(1963), *Petschek*(1964)]. There are two elements in the magnetic reconnection process [*Kulsrud*(1998)]: one is the change of magnetic field topology, and the other is the rate of energy conversion from magnetic field energy to plasma thermal and flow energies. The study of the physical process of magnetic reconnection is still an intensive ongoing activity in the plasma physics community. Some critical issues of magnetic reconnection are still being pursued: how current sheets form and what the current sheet topology is; how magnetic field reconnects in a 3D sheared magnetic field; what causes reconnection (external force or internal waves or instabilities); what the reconnection rate is and is it steady or spontaneous; and how electrons and ions gain energy; etc.

Despite insufficient understanding of magnetic reconnection physics, there have been constant attempts to propose the magnetic reconnection as the substorm onset mechanism. In particular, the near-earth neutral line model [*Nagai and Kamide*(1995)] has gained popularity which postulates that the substorm expansion phase is caused by magnetic reconnection in the near-earth plasma sheet. The near-Earth neutral line model is based on the scenario that the plasma and magnetic field are pinched by oppositely directed flows from north and south to form a current sheet in the equatorial near-Earth plasma sheet region. As magnetic reconnection occurs via plasma dissipation, both Earthward and tailward flows are generated to transport plasma and magnetic flux. In order for magnetic reconnection to be a viable mechanism for the substorm onset, several serious difficulties of the near-Earth neutral line model associated with both observational and theoretical constraints must be addressed. In the following we discuss a few of these difficulties and how the kinetic ballooning instability theory can naturally explain some critical substorm observations.

First, the effort by MHD simulations to find out whether magnetic reconnection process can occur in the near-Earth plasma sheet region has been carried out. It is a common conclusion that under normal solar wind and IMF conditions observed during substorms magnetic reconnection does not occur in the near-earth plasma sheet region. Even when magnetic reconnection occurs in the near-Earth plasma sheet under extremely unrealistic solar wind and IMF conditions in the MHD simulations, the reconnection region is quite broad ($>$ 3 hours in local time and $> 3R_E$ in radial direction) in the equatorial region [*Ogino*(1999)]. This is inconsistent with the observation that the substorm onset is initiated in a small localized region of less than $1R_E$ in radius in the near-Earth plasma sheet at $x \simeq -10R_E$ around midnight. This corresponds to a localized initial aurora brightening region of less than a few degrees wide in longitude and less than one degree wide in latitude in the ionosphere. On the other hand, it is natural for us to expect that the kinetic ballooning instability will be initiated in a localized region in the near-Earth plasma sheet where the the plasma β is large, mag-

netic curvature is strong and field line tension is weak so that the driving free energy is maximized.

Secondly, the AMPTE/CCE observation of magnetic field data during substorms has clearly identified a low frequency instability which is excited before substorm onset and continues to evolve and develop into a strong plasma turbulence during the expansion phase. There is no physical mechanism to explain the low frequency instability based on the near-Earth neutral line model. On the other hand, the low frequency instability can be best explained in terms of the kinetic ballooning instability which requires kinetic effects of finite ion Larmor radii and trapped electron dynamics to properly understand the high β_c (≥ 50), the observed wave frequency and growth rate, and the associated enhanced parallel electric field that is required to accelerate particle into and out of the auroral ionosphere.

Thirdly, it is required that the magnetic reconnection process in the near-earth plasma sheet region must produce observable high speed Earthward plasma flows perpendicular to the field lines before and during the substorm expansion phase. It relies on the Earthward flow to carry plasma and magnetic flux to cause magnetic field dipolarization in the near-Earth plasma sheet region. The near-Earth neutral line model advocates have been arguing that the existence of high speed flows is manifested by the bursty bulk flows (BBF). However, more recent analysis of the GEOTAIL data has indicated that there is no statistically favorable evidence of large perpendicular Earthward flows within $25R_E$ from the Earth in the night side [*Machida*(1999)]. Moreover, recent detailed data analysis indicates that Earthward flows are either field-aligned ion beams or some types of MHD perturbations without significant B_z flux.

5 Summary

In this paper we have identified a new scenario and physical processes of substorm explosive growth phase, onset and current disruption observed by AMPTE/CCE. We have found a low-frequency instability with a wave period of about $50-75$ sec excited at approximately 2 minutes before the current disruption onset, and we have interpreted it as the kinetic ballooning instability (KBI). The β threshold (≥ 50) for exciting KBI is at least 10^2 larger than that based on the ideal MHD theory because of the kinetic effects of trapped electron dynamics and finite ion Larmor radii which give rise to a large parallel electric field and hence a parallel current that greatly enhances the stabilizing effect of field line tension. With the KBI theory we are able to explain the enhanced duskward ion flux which occurs only during the explosive growth phase ($\approx$ 30 sec) and can excite higher frequency instabilities such as the cross-field current instabilities (CCI) [*Lui*(1996)]. Thus, our new substorm scenario emphasizes KBI which

can naturally account for the features of the explosive growth phase and the initiation of current disruption through a combination of KBI and higher frequency instabilities such as CCI. We have also discussed the difficulties of explaining the substorm onset by the magnetic reconnection process as proposed in the near-Earth neutral line model.

Finally, we point out that even though progress has been made in understanding the substorm onset mechanism from the model of kinetic ballooning instability, more works are still needed to carry out a conclusive demonstration of substorm process by both theory and observation.

Acknowledgments

The author would like to thank Profs. T. Ogino and Y. Kamide of Solar-Terrestrial Environment Laboratory, Nagoya University, Japan for useful discussion. This work is supported by the NSF Grants No. ATM-9523331 and the DoE Contract No. DE-AC02-76-CHO3073.

References

Cheng, C. Z., High-n collisionless ballooning modes in axisymmetric toroidal plasmas, *Nucl. Fusion*, *22*, 773, 1982a.

Cheng, C. Z., Kinetic theory of collisionless ballooning modes, *Phys. Fluids*, *25*, 1020, 1982b.

Cheng, C. Z., A kinetic-magnetohydrodynamic model for low-frequency phenomena, *J. Geophys. Res.*, *96*, 21159, 1991.

Cheng, C. Z., and Q. Qian, Theory of ballooning-mirror instabilities for anisotropic pressure plasmas in the magnetosphere, *J. Geophys. Res.*, *99*, 11193, 1994.

Cheng, C. Z., N. N. Gorelenkov, and C. T. Hsu, Fast particle destabilization of TAE modes, *Nucl. Fusion*, *35*, 1639, 1995.

Cheng, C. Z., and A. T. Y. Lui, Kinetic Ballooning Instability for Substorm Onset and Current Disruption Observed by AMPTE/CCE, *Geophys. Res. Lett.*, *25*, 4091, 1998.

Hurricane, O. A., R. Pellat, and F. V. Coroniti, The kinetic response of a stochastic plasma to low frequency perturbations, *Geophys. Res. Lett.*, *21*, 253, 1994.

Liu, W. W., Physics of the explosive growth phase: Ballooning instabilities revisited, *J. Geophys. Res.*, *102*, 4927, 1997.

Kulsrud, R. M., Magnetic reconnection in a magnetohydromagnetic plasma, *Phys. Plasmas*, *5*, 1599, 1998.

Lui, A. T. Y., Current disruption in the Earth's magnetosphere: Observations and models, *J. Geophys. Res.*, *101*, 13067, 1996.
Lui, A. T. Y., et al., Current disruptions in the near-Earth neutral sheet region, *J. Geophys. Res.*, *97*, 1461, 1992.
Machida, S., private communication, 1999.
Nagai, T., and Y. Kamide,, Magnetic field changes at the neutral sheet associated with substorm expansion onset: A model prediction and observation, *J. Geophys. Res.*, *100*, 3521, 1995.
Ogino, T., private communication, 1999.
Ohtani, S., K. Takahashi, L. Zanetti, T. A. Potemra, R. W. McEntire, and T. Iijima, Initial signatures of magnetic field and energetic particle fluxes at tail reconfiguration: Explosive growth phase, *J. Geophys. Res.*, *97*, 19311, 1992.
Ohtani, S., T. Higuchi, A. T. Y. Lui, and K. Takahashi, Magnetic fluctuations associated with tail current disruption: Fractal analysis, *J. Geophys. Res.*, *100*, 19135, 1995.
Parker, E. N., The solar flare phenomenon and the theory of reconnection and annihilation ofmagnetic fields, *Astrophys. J. Suppl. Ser.*, *8*, 177, 1963.
Petschek, H. E., Magnetic field annihilation, in AAS-ASA Symposium on the Physics of Solar Flare, ed. by W. N. Hess, NASA SP-50, Washington, DC, 425, 1964.
Roux, A., S. Perraut, A. Morane, P. Robert, A. Korth, G. .Kremser, A. Pederson, R. Pellinen, and Z. Y. Pu, Plasma sheet instability related to the westward traveling surge, *J. Geophys. Res.*, *96*, 17697, 1991.
Sweet, P. A., The neutral point theories of solar flares, in Electromagnetic Phenomena in Cosmic Physics, ed. E. Lehnert, 135, 1958.
Voronkov, L., R. Rankin, P. Frycz, V. T. Tikonchuk, and J. C. Samson, Coupling of shear flow and pressure gradient instabilities, *J. Geophys. Res.*, *102*, 9639, 1997.

List of Participants

Cheng, C.Z.	Plasma Physics Laboratory, Princeton University
Hatakeyama, Rikizo	Dep.Electrical Engineering, Graduate School of Engineering, Tohoku University
Hatori, Tadatsugu	Dep.Information Science, Kanagawa University
Iwaki, Takashi	Dep.Physics, Graduate School of Science, Kyoto University
Kato, Takako	National Institute for Fusion Science
Machida, Shinobu	Dep.Geophysics, Graduate School of Science, Kyoto University
Mayama, Hiroyuki	Institute for Fundamental Chemistry
More, Richard	National Institute for Fusion Science
Ogino, Tatsuki	Solar Terrestrial and Environment Laboratory, Nagoya University
Saeki, Kohichi	Dep.Physics, Shizuoka University
Sasai, M.	Graduate School of Human Information, Nagoya University
Shibata, Kazunari	Kwasan and Hida Observatories Kyoto University
Shimazu, Hironori	Communications Research Laboratory
Shoji, Tatsuo	Dep.Energy Engineering and Science, Graduate School of Engineering, Nagoya University
Takagi, Seiji	Graduate School of Human Information, Nagoya University
Tanaka, Masayoshi	National Institute for Fusion Science
Tanaka, Motohiko	National Institute for Fusion Science
Terada, Naoki	Dep.Geophysics, Graduate School of Science, Kyoto University
Yoshikawa, Kenichi	Dep.Physics, Graduate School of Science, Kyoto University

Publication List of NIFS-PROC Series

NIFS-PROC-1 "U.S.-Japan on Comparison of Theoretical and Experimental Transport in Toroidal Systems Oct. 23-27, 1989" Mar. 1990

NIFS-PROC-2 "Structures in Confined Plasmas –Proceedings of Workshop of US-Japan Joint Institute for Fusion Theory Program–" Mar. 1990

NIFS-PROC-3 "Proceedings of the First International Toki Conference on Plasma Physics and Controlled Nuclear Fusion –Next Generation Experiments in Helical Systems– Dec. 4-7, 1989" Mar. 1990

NIFS-PROC-4 "Plasma Spectroscopy and Atomic Processes –Proceedings of the Workshop at Data & Planning Center in NIFS–" Sep. 1990

NIFS-PROC-5 "Symposium on Development of Intensed Pulsed Particle Beams and Its Applications February 20 1990" Oct. 1990

NIFS-PROC-6 "Proceedings of the Second International TOKI Conference on Plasma Physics and Controlled Nuclear Fusion, Nonlinear Phenomena in Fusion Plasmas -Theory and Computer Simulation-" Apr. 1991

NIFS-PROC-7 "Proceedings of Workshop on Emissions from Heavy Current Carrying High Density Plasma and Diagnostics" May 1991

NIFS-PROC-8 "Symposium on Development and Applications of Intense Pulsed Particle Beams, December 6 - 7, 1990" June 1991

NIFS-PROC-9 "X-ray Radiation from Hot Dense Plasmas and Atomic Processes" Oct. 1991

NIFS-PROC-10 "U.S.-Japan Workshop on "RF Heating and Current Drive in Confinement Systems Tokamaks, Nov. 18-21, 1991" Jan. 1992

NIFS-PROC-11 "Plasma-Based and Novel Accelerators (Proceedings of Workshop on Plasma-Based and Novel Accelerators) Nagoya, Japan, Dec. 1991" May 1992

NIFS-PROC-12 "Proceedings of Japan-U.S. Workshop P-196 on High Heat Flux Components and Plasma Surface Interactions for Next Devices" Mar. 1993

NIFS-PROC-13 「NIFS シンポジウム
「核燃焼プラズマの研究を考える－現状と今後の取り組み方」
1992年7月15日、核融合科学研究所」1993年7月
"NIFS Symposium "Toward the Research of Fusion Burning Plasmas -Present Status and Future strategy-" 1992 July 15, National Institute for Fusion Science" July 1993 (in Japanese)

NIFS-PROC-14 "Physics and Application of High Density Z-pinches" July 1993

NIFS-PROC-15 岡本正雄、講義「プラズマ物理の基礎」
平成5年度、総合大学院大学1994年2月
M. Okamoto,
"Lecture Note on the Bases of Plasma Pysics"Graduate University for Advanced Studies"
Feb. 1994 (in Japanese)

NIFS-PROC-16 代表者 河合良信
平成5年度 核融合科学研究所共同研究
研究会報告書「プラズマ中のカオス現象」
"Interdisciplinary Graduate School of Engineering Sciences" Report of the meeting on Chaotic Phenomena in Plasma" Apr. 1994 (in Japanese)

NIFS-PROC-17 平成5年度NIFSシンオジウム報告書
「核融合炉開発研究のアセスメント」平成5年11月29日-30日 於 核融合科学研究所
"Assessment of Fusion Reactor Development" Proceedings of NIFS Symposium held on November 29-30,1993 at National Insitute for Fusion Science" Apr. 1994 (in Japanese)

NIFS-PROC-18 "Physics of High Energy Density Plasmas Produced by Pulsed Power" June 1994

NIFS-PROC-19 K. Morita, N. Noda (Ed.),
"Proceedings of 2nd International Workshop on Tritium Effects in Plasma Facing Components at Nagoya University, Symposion Hall, May 19-20, 1994" Aug. 1994

NIFS-PROC-20 研究代表者 阿部 勝憲 (東北大学・工学部)
所内世話人 野田信明
平成6年度 核融合科学研究所共同研究[研究会]「金属系高熱流束材料の開発と評価」成果報告書
K. Abe and N. Noda (Eds.),
"Research and Development of Metallic Materials for Plasma Facing and High Heat Flux Components" Nov. 1994 (in Japanese)

NIFS-PROC-21 世話人:森田 健治(名大工学部)、金子 敏明(岡山理科大学理学部)
「境界プラズマと炉壁との相互作用に関する基礎過程の研究」研究会報告
K. Morita (Nagoya Univ.), T. Kaneko (Okayama Univ. Science)(Eds.)
"NIFS Joint Meeting "Plasma-Divertor Interactions" and "Fundamentals of Boundary Plasma-Wall Interactions" January 6-7, 1995 National Institute for Fusion Science" Mar. 1995 (in Japanese)

NIFS-PROC-22 代表者 河合 良信
プラズマ中のカオス現象
Y. Kawai,
"Report of the Meeting on Chaotic Phenomena in Plasma, 1994" Apr. 1995 (in Japanese)

NIFS-PROC-23 K. Yatsui (Ed.),
"New Applications of Pulsed, High-Energy Density Plasmas" June 1995

NIFS-PROC-24 T. Kuroda and M. Sasao (Eds.),
"Proceedings of the Symposium on Negative Ion Sources and Their Applications, NIFS, Dec. 26-27, 1994" , Aug. 1995

NIFS-PROC-25 岡本 正雄
新古典輸送概論(講義録)
M. Okamoto,
"An Introduction to the Neoclassical Transport Theory" (Lecture note), Nov. 1995 (in Japanese)

NIFS-PROC-26 Shozo Ishii (Ed.),
"Physics, Diagnostics, and Application of Pulsed High Energy Density Plasma as an Extreme State" May 1996

NIFS-PROC-27 代表者 河合 良信
プラズマ中のカオスとその周辺非線形現象
Y. Kawai ,
"Report of the Meeting on Chaotic Phenomena in Plasmas and Beyond, 1995" Sep. 1996 (in Japanese)

NIFS-PROC-28 T. Mito (Ed.),
"Proceedings of the Symposium on Cryogenic Systems for Large Scale Superconducting Applications" Sep. 1996

NIFS-PROC-29 岡本 正雄
講義「核融合プラズマ物理の基礎-1」
平成8年度 総合研究大学院大学 数物科学研究科 核融合科学専攻 1996年10月
M. Okamoto

"Lecture Note on the Fundamentals of Fusion Plasma Physics - I" Graduate University for Advanced Studies; Oct. 1996 (in Japanese)

NIFS-PROC-30 研究代表者　栗下　裕明（東北大学金属材料研究所）
所内世話人　加藤　雄大
平成 8 年度核融合科学研究所共同研究「被損傷材料の微小体積強度評価法の高度化」研究会　1996年 10月　9日　於：核融合科学研究所

H. Kurishita and Y. Katoh (Eds.)
"NIFS Workshop on Application of Micro-Indentation Technique to Evaluation of Mechanical Properties of Fusion Materials" Oct. 9, 1996, NIFS ; Nov. 1996 (in Japanese)

NIFS-PROC-31 岡本　正雄
講義「核融合プラズマ物理の基礎 - II 」
平成 8 年度　総合研究大学院大学　数物科学研究科　核融合科学専攻　1997年 4月
M. Okamoto
"Lecture Note on the Fundamentals of Fusion Plasma Physics - II" Graduate University for Advanced Studies; Apr. 1997 (in Japanese)

NIFS-PROC-32 代表者　河合　良信
平成8年度　核融合科学研究所共同研究　研究会報告「プラズマ中のカオスとその周辺非線形現象」
Y. Kawai (Ed)
"Report of the Meeting on Chaotic Phenomena in Plasmas and Beyond, 1996" Apr. 1997 (mainly in Japanese)

NIFS-PROC-33 H. Sanuki,
Studies on Wave Analysis and Electric Field in Plasmas; July 1997

NIFS-PROC-34 プラズマ対向機器・PSI・熱・粒子制御合同研究会報告
平成 9 年 6 月 27 日（金）9:00 ～16:20　核融合科学研究所・管理棟 4 F 第 1 会議室
1997年　10月
T. Yamashina (Hokkaido University)
"Plasma Facing Components, PSI and Heat/Particle Control June 27, 1997, National Institute for Fusion Science" Oct. 1997 (in Japanese)

NIFS-PROC-35 T. Watari,
"Plasma Heating and Current Drive" Oct. 1997

NIFS-PROC-36 T. Miyamoto and K. Takasugi (Eds.)
"Production and Physics of High Energy Density Plasma; Production and Physics of High Energy Density Plasma" Oct. 1997

NIFS-PROC-37 (Eds.)T. Fujimoto, P. Beiersdorfer,
"Proceedings of the Japan-US Workshop on Plasma Polarization Spectroscopy and The International Seminar on Plasma Polarization Spectroscopy January 26-28, 1998, Kyoto" June 1998

NIFS-PROC-38 (Eds.) Y. Tomita, Y. Nakamura and T. Hayashi,
"Proceedings of the Second Asian Pacific Plasma Theory Conference APPTC '97, January 26-28, 1998, Kyoto" Aug. 1998

NIFS-PROC-39 (Ed.) K. Hirano,
"Production, Diagnostics and Application of High Energy Density Plasmas" Dec. 1998

NIFS-PROC-40 研究代表者　加古　孝（電気通信大学）
所内世話人　渡辺　二太
平成 10 年度核融合科学研究所共同研究 研究会「プラズマ閉じ込めに関連する数値計算手法の研究」
Ed. by T. Kako and T. Watanabe
"Proceeding of 1998-Workshop on MHD Computations "Study on Numerical Methods Related to Plasma Confinement" Apr. 1999

NIFS-PROC-41 (Eds.) S. Goto and S. Yoshimura,
"Proceedings of The US-Japan Workshop and The Satellite Meeting of ITC-9 on Physics of

High Beta Plasma Confinement in Innovative Fusion System, Dec. 14-15, 1998, NIFS, Toki" Apr. 1999

NIFS-PROC-42 (Eds.) H. Akiyama and S. Katsuki,
"Physics and Applications of High Temperature and Dense Plasmas Produced by Pulsed Power" Aug. 1999

NIFS-PROC-43 (Ed.) M. Tanaka,
"Structure Formation and Function of Gaseous, Biological and Strongly Coupled Plasmas" Sep. 1999